The Role of Three-Body Interactions on the Equilibrium and Non-Equilibrium Properties of Fluids from Molecular Simulation

Gianluca Marcelli

Dissertation
Submitted in fulfilment of requirements for the degree of

Doctor of Philosophy

Centre for Molecular Simulation and
School of Information Technology

Swinburne University of Technology
2001

Alla mia famiglia e
agli amici piu' cari
che non si sono fatti
distrarre dalla lontananza.

Declaration

I hereby declare that the thesis entitled "The Role of Three-Body Interactions on the Equilibrium and Non-Equilibrium Properties of Fluids from Molecular Simulation", and submitted in fulfilment of the requirements for the Degree of Doctor of Philosophy in School of Information Technology of Swinburne University of Technology, is my own work and that it contains no material which has been accepted for the award to the candidate of any other degree or diploma, except where due reference is made in the text of the thesis. To the best of my knowledge and belief, it contains no material previously published or written by another person except where due reference is made in the text of the thesis.

Gianluca MARCELLI

February 2001

Abstract

The aim of this work is to use molecular simulation to investigate the role of three-body interatomic potentials in noble gas systems for two distinct phenomena: phase equilibria and shear flow. In particular we studied the vapour-liquid coexisting phase for pure systems (argon, krypton and xenon) and for an argon-krypton mixture, utilizing the technique called Monte Carlo Gibbs ensemble. We also studied the dependence of the shear viscosity, pressure and energy with the strain rate in planar Couette flow, using a non-equilibrium molecular simulation (NEMD) technique.

The results we present in this work demonstrate that three-body interactions play an important role in the overall interatomic interactions of noble gases. This is demonstrated by the good agreement between our simulation results and the experimental data for both equilibrium and non-equilibrium systems.

The good results for vapour-liquid coexisting phases encourage performing further computer simulations with realistic potentials. This may improve the prediction of quantities like critical temperature and density, in particular of substances for which these properties are difficult to obtain from experiment.

We have demonstrated that use of accurate two- and three-body potentials for shearing liquid argon and xenon displays significant departure from the expected strain rate dependencies of the pressure, energy and shear viscosity. For the first time, the pressure is convincingly observed to vary linearly with an apparent analytic $\dot{g}^2$ dependence, in contrast to the predicted $\dot{g}^{3/2}$ dependence of mode-coupling theory. Our best extrapolation of the zero-shear viscosity for argon gives excellent agreement (within 1%) with the known experimental data. To the best of our knowledge, this the first time that such accuracy has been

achieved with NEMD simulations. This encourages performing simulations with accurate potentials for transport properties.

Acknowledgments

Publications from this thesis

The following papers have been based on part of this work:

[1]   **Marcelli G. and Sadus R. J. (1999),** *Molecular simulation of the phase behavior of noble gases using accurate two-body and three-body intermolecular potentials***, J. Chem. Phys.** 111**, 1533-1540.**

[2]   Marcelli G. and Sadus R. J. (2000), *A link between the two-body and three-body interaction energies of fluids from molecular simulation*, J. Chem. Phys. **112**, 6382-6385.

[3]   Marcelli G. and Sadus R. J. (2001), *Three-body interactions and the phase equilibria of mixtures*, High Temp. -High Pressures **33**, 111-118.

[4]   Marcelli G., Todd B. D. and Sadus R. J. (2001), *Analytic dependence of the pressure and energy of an atomic fluid under shear*, Phys. Rev. E **63**, in press.

[5]   **Marcelli G., Todd B. D. and Sadus R. J. (2001),** *The strain rate dependence of shear viscosity, pressure and energy from two-body and three-body interactions***, Fluid Phase Equilib., in press.**

[6]   **Marcelli G., Todd B. D. and Sadus R. J. (2001),** *On the relationship between two-body and three-body interactions from non-equilibrium molecular dynamics simulation***, J. Chem. Phys., submitted.**

Table of Contents

Table of Symbols

Abbreviations

AAD	**Absolute average deviations**
AT	**Axilrod -Teller Potential**
BFW	**Barker-Fisher-Watts intermolecular potential**
fcc	**Face-centred cubic**
LHS	**Left-hand-side**
LJ	**Lennard -Jones potential**
hcp	**Hexagonal close-packed**
MD	**Molecular dynamics**
MC	**Monte Carlo**
MPPT	**Møller-Plesset perturbation theory**
NEMD	**Non-equilibrium molecular dynamics**
NPT	**Ensemble where number of particles, pressure and temperature are kept constant**
NVT	**Ensemble where number of particles, volume and temperature are kept constant**
RHS	**Right-hand-side**
WCA	**Weeks-Chandler-Andersen intermolecular potential**

Subscripts and superscripts

*****	**Reduce units**
I	**Phase *I***
2b, 2body	**Two body potential contribution**

3b, 3body	**Three body potential contribution**
$acc\,(old \rightarrow new)$	**Acceptance probability of a move from** *old* **to** *new*
conf.	**Configurational**
crit.	**Critical property**
D	**Dipole**
Disp	**Dispersion**
L, liq.	**Liquid phase**
O	**Octupole**
Q	**Quadrupole or partition function**
tot	**Total**
V, vap.	**Vapour phase**

Latin alphabet

B	**Second virial coefficient**
C	**Third virial coefficient**
E	**Potential energy**
e	**Euler number**
F_i	**Force acting on particle** i
G(r)	**Radial distribution function**
H	**Hamiltonian or enthalpy**
k	**Boltzmann's constant**
L	**Length of the simulation box**
m	**Mass**
N	**Number of particles**

P	Hydrostatic pressure
P	Pressure tensor
p_i	Momentum of particle i
Q	Partition function
R	Molar gas constant
r_i	Position of particle i
$r_{ij} = r_i - r_j$	Relative position of particle i and j
$r_{ij} = \lvert r_i - r_j \rvert$	
$\dot{r}_i, \ddot{r}_i$	First and second time derivative of the position of particle i
$r, \boldsymbol{q}, \boldsymbol{f}$	Polar coordinates
T	Temperature
t	Time
Δt	Time step
u	Intermolecular potential function
V	Volume
$\nabla \boldsymbol{v}$	Strain rate tensor
x, y, z	Cartesian coordinates
$\hat{x}, \hat{y}, \hat{z}$	Cartesian unit vectors
x_I^a	Composition of species a in phase I.

Greek alphabet

$\boldsymbol{a}$ (*old* $\rightarrow$ *new*)	Probability of generating configuration *new* starting from *old*
$\dot{g}$	Shear rate

η	Shear viscosity
Λ	Thermal de Broglie wavelength
μ	Chemical potential
ν	Non-additive coefficient
π	Pi
$\pi(old \rightarrow new)$	Transition probability from *old* to *new*
ρ	Numeric density
ψ, χ, ϕ	Wave functions as defined in Eqs. (2.1) and (2.3)

Chapter 1

Molecular Simulation of Fluids

This work is the result of research conducted on the molecular simulation of fluids. Traditionally, science, in order to understand the phenomena occurring in nature, used two different approaches: experiment and theory. These two approaches are not necessarily separate. In fact, the 'art' of collecting experimental data usually requires profound theoretical knowledge, while on the other hand, models require a necessary minimum amount of experimental data to derive some of their parameters. It is better to view them as complementary approaches that together strengthen the scientific investigation. Molecular simulation, since the advent of the computer, has become an important means of carrying out scientific research.

Despite the commonly used term 'computer experiments', molecular simulation belongs to the theoretical approach, unless we intend to investigate a 'virtual' reality. We can envisage two main reasons why molecular simulation is associated with the experimental approach. The first reason is a suggestive one and is due to its ability to reproduce the motion of the particles as it occurs in nature. In this regard, even if simulation techniques could reproduce molecular motion in detail, they would be, in any case, a representation of real systems. Moreover techniques that try to simulate closely real systems, show less predictive power than others, which use more artificial implementations. The other reason is more a procedural one. Usually molecular

simulation is used to test the validity of a theory or a theoretical conjecture, or even to discriminate between two theories. While this is indeed true, ultimately it is experiment that will decide the matter.

More interesting, and maybe more speculative, is to consider if molecular simulation is a deductive or an inductive method. The use of semiempirical models, such as for example intermolecular potentials fitted on experimental data, could be indeed indicative of an inductive procedure. However, these models are usually supposed to be applied under a range of conditions wider than those used to derive the models themselves. Furthermore, *ab initio* techniques [Gal93] are meant to predict general behaviour, utilizing very elementary initial assumptions.

The appeal and usefulness of molecular simulation is that it often allows accurate calculation of natural phenomena without the plethora of approximations and assumptions that limit conventional theoretical approaches to prediction and estimation. The key theoretical assumption of molecular simulation is to envisage any physical system as a collection of particles. In general, all the macroscopic properties such as temperature, pressure and density can be related to the motion or the state of these particles. Consequently, knowing the motion or the state of the particles enables one to deduce the macroscopic properties of the system. From a *classical* dynamics viewpoint, to derive the motion of a collection of particles it is required to know the forces acting on them. One may then use Newton's equations of motion to solve for the particle positions and momenta. From a statistical mechanics viewpoint, the knowledge of the state of an ensemble of particles is related to the energy of the particles, which allows the derivations of probabilities relative to that state.

Molecular simulation techniques, therefore, require the adoption of an intermolecular potential to represent the interactions between the particles of any physical system

(solid, liquid or gas). The intermolecular potential and a limited number of approximations, represent the model of a physical system that is used to test against experimental data or preexisting theoretical models. The computer generates either the motion or different states of the particles, and the average values of the physical quantities of interest can be calculated. The two main molecular simulation techniques, *molecular dynamics* (MD) and *Monte Carlo* (MC) techniques [All87, Hey98], implement these ideas. The first follows a dynamical approach, utilizing Newton equations of motion, the second a statistical mechanics approach, using the concept of configuration space. Nowadays these techniques have reached such a level of sophistication that they are able to reproduce experimental results with good accuracy [Ant97, Buk01].

It is commonly assumed that intermolecular interactions are confined to pairs of molecules [Pan87, Pan88, Pla97, Sad96a], and contributions involving three, four or more atoms are ignored. When this assumption is invoked, the molecular properties are assumed to be 'pair-additive.' Generally, interactions between pairs of molecules make the overwhelming contribution to the overall intermolecular interaction. However, it is also documented [Elr94] that three-body interactions can make a significant contribution to intermolecular interactions in liquids, (see Chapter 2). Despite this, molecular simulations rarely account rigorously for the effect of three-body interactions [Sad96b, Sad98a, Sad98b, Sad98c, Ant97]. Instead, the typical molecular simulation assumes pair additivity, and uses a simple 'effective' intermolecular potential in which many-body effects are said to be included in the values of the intermolecular parameters.

In the following sections we summarize the aims of our work (section 1.1) and give a brief account of the background and progress in molecular simulation regarding the topics we investigated (section 1.2 and 1.3).

1.1 Aims

The aim of this work is to use molecular simulation to investigate the role of three-body interatomic potentials in noble gas systems for two distinct phenomena: phase equilibria and shear flow. In particular we studied the vapour-liquid coexisting phase for pure systems (argon, krypton and xenon) and for an argon-krypton mixture. We also studied the dependence of the shear viscosity, pressure and energy with the strain rate in planar Couette flow. We give here a brief review of the previous work in these fields to better delineate our task. The rest of the thesis is arranged as follows: in Chapter 2 we give details of the interatomic potentials and of the techniques used. In Chapter 3 and Chapter 4 we report the results obtained for phase equilibria and planar Couette flow simulations respectively. Chapter 5 contains our conclusions and recommendations.

1.2 Background

Previous work [Sad96b, Ant97, Sad98a] regarding the role of three-body interactions on the phase behaviour of pure atomic systems has been restricted to the Axilrod-Teller term [Axi43] and the calculations have been confined mainly to argon. In addition, calculations on the influence of three-body interactions on phase behaviour of some theoretical binary mixtures are also available [Sad98b, Sad98c]. Sadus and Prausnitz [Sad96b] reported that the Axilrod-Teller term contributes typically 5% of the overall energy of the liquid phase of argon. Calculations for the vapour-liquid coexistence of argon by Anta et al. [Ant97] and Sadus [Sad98a] using a combination of the Lennard-

Jones and Axilrod-Teller potentials indicate that the inclusion of three-body interactions deteriorates the agreement between theory and experiment for the coexisting liquid phase densities. This failure can be attributed to the effective nature of the Lennard-Jones potential (see Chapter 2). The use of 'effective' intermolecular potentials is a source of considerable inaccuracy and uncertainty in molecular simulations. For example, in Chapter 3 we show that three-body interactions contribute significantly to the phase behaviour of fluids, whereas this effect had been hidden previously by the use of effective intermolecular potentials. The agreement between experiment and theory for the phase envelope is improved considerably by explicitly accounting for three-body interactions. However, accounting for three-body interactions requires considerably more computing resources than simple pair interactions. In the worst case, the computing time of a system of N molecules scales in proportion to N^2 for pair interactions, compared with N^3 for three-body interactions. Although computation-time saving algorithms have been developed [Sad99, see also Appendix 2] to avoid the worst case scenario, accounting for three-body interactions typically requires at least one order of magnitude more computing time than simple pair calculations. This means that such calculations are far from routine, even with today's high performance computers. However, because of the importance of three-body interactions, it is highly desirable to include them in molecula r simulations.

Anta et al. [Ant97] reported good results for vapour-liquid coexistence of argon using the Aziz-Slaman [Azi86, Azi93] potential in conjunction with the Axilrod-Teller term. Unlike the Lennard-Jones potential, the Aziz-Slaman potential is a genuine pair potential and it is thought to be the best representation of the two-body interactions for argon. However, its mathematical expression is rather complicated. For argon we used the Barker-Fisher-Watts (BFW) potential [Bar71a], for computational convenience and

because equivalent expressions are available for krypton and xenon. We also show in Chapter 3 that the Aziz-Slaman potential and BFW potential produce similar results for the argon vapour-liquid coexisting curve.

Non-equilibrium molecular dynamics (NEMD) simulations of Couette flow (see Chapter 2) are commonly reported using either the Lennard-Jones or Weeks-Chandler-Anderson (WCA) intermolecular potentials to describe interatomic interactions [Eva90, Sar98]. However, both the Lennard-Jones and WCA potentials are effective multi-body potentials and as such they do not represent two-body interactions accurately [Bar76]. Earlier simulations [Eva80, Eva81] with these potentials appear to confirm the non-analytic dependence of viscosity (h) with shear rate in the limit of low strain rate ($\dot{g}$). However, more recent work questions the $\dot{g}^{1/2}$ dependence of the shear viscosity. For example, Ryckaert et al. [Ryc88] and Ferrario et al. [Fer91a] found a $\dot{g}^2$ dependence of the shear viscosity. The significance of these results is unclear because of the high strain rates and large statistical uncertainties in the data [Tra98]. Furthermore, using profile biased thermostats, namely thermostats that make some assumption about the form of the streaming velocity profile [Eva90], under conditions of large strain rates, can induce unwanted string-phases in the fluid, which consist of highly ordered solid-like configurations [Erp84]. This significantly reduces both the shear viscosity and the hydrostatic pressure from their true values [Eva86, Eva92]. Bhupathiraju et al. [Bhu96] demonstrated that in the limit of zero strain rate the shear viscosity behaves in a Newtonian manner, i.e., the shear viscosity becomes independent of $\dot{g}$. Travis et al. [Tra98] showed that the shear viscosity may be fit by a number of functions that do not have any theoretical basis. They also showed that the viscosity profile may be successfully fit by two separate linear functions of $\dot{g}^{1/2}$ in two different strain rate regimes. Alternatively a Cross equation [Cro65], or the Quentrec local-order theory for

isotropic fluids [Que82, Tro84] were also found to give reasonable agreement with simulation data.

Of particular relevance for our current work is the mode-coupling theory [Kaw73] which predicts that in the limit of zero shear rate the shear viscosity is a non-analytic function of the strain rate, $h \approx \dot{g}^{1/2}$. This theory also predicts that the hydrostatic pressure varies as $\dot{g}^{3/2}$. Mode coupling theory does not provide guidance on how small the strain rate must be in order to observe the predicted $\dot{g}^{1/2}$ and $\dot{g}^{3/2}$ dependence for the shear viscosity and hydrostatic pressure, respectively. As NEMD simulations are typically performed at relatively high rates of strain to obtain high signal to noise ratios, such simulations cannot confirm the predictions of mode coupling theory. In the absence of simulation data at field strengths several orders of magnitude smaller than those typically achievable, the question of the validity of mode coupling theory remains open. However, most previous NEMD simulations using effective multi-body intermolecular potentials have shown that the hydrostatic pressure and internal energy *do* behave as predicted by the theory, even at these relatively high strain rates.

We are aware of only one previous NEMD study of simple atomic fluids interacting via accurate two- and three-body intermolecular potentials. Lee and Cummings [Lee94] reported NEMD simulations of planar Couette flow for a system of 108 atoms interacting via a potential composed of the Barker-Fisher-Watts two-body potential [Bar71a] plus the three-body triple-dipole potential of Axilrod and Teller (AT) [Axi43]. The three-body interaction was observed to reduce the value of the shear viscosity by only 3%. In the range of strain rates studied, Lee and Cummings found that the strain rate behaviour of the energy, pressure and shear viscosity all conformed to the predictions of mode coupling theory.

1.3 Progress in molecular simulation

Phase equilibria

It is found by experiment that only a certain number of the physical properties of a substance can have arbitrary values. The remaining properties are determined by the nature of the system. For example, considering a gas at temperature T with a given mass m and held in a container of volume V, the value of its pressure P can be obtained via an equation in m, V and T;

$$f(P,m,V,T) = 0 \qquad\qquad (1.1)$$

such an expression is known in general as the equation of state [Sea75]. In this work we are interested in thermodynamic systems, the state of which can be determined by properties like density, temperature, pressure, chemical potential, etc. The phase of the system, namely gas, liquid or solid, is an important characteristic and in particular phase transitions represent an important field of study. Both technological and scientific applications require a detailed knowledge of phase behaviour of fluids and their mixtures. For example, chemical industries need to know transition phenomena and the relative parameters (critical temperatures, pressures, etc.) to separate particular substances from their original mixtures. This wide interest is demonstrated by the large amount of experimental data [Wic73] collected and the number of semiempirical and theoretical models proposed regarding phase equilibria. Despite the substantial knowledge so far gained much more remains to be learned. For example, multicomponent mixture experiments are very rare and performed in limited temperature and pressure ranges because of their high realization costs [Gub89]. Significant information comes from equation-of-state models [San94], but they can not

be used to accurately predict properties outside the range of experiments adopted to obtain the parameters of the models.

In this regard, molecular simulation represents a complementary method [Gub96, Qui01]. Utilizing intermolecular potentials obtained from either quantum mechanics or semi-empirical calculations, and adopting fewer approximations, molecular simulation can be applied over a wider range of conditions. In fact, even if their parameters are determined from particular experimental data, they can be used under more general conditions [Bar76]. Here we give a brief description of some of the molecular simulation techniques dedicated to phase equilibria. For further details we refer to the following reviews in the literature [Gub89, All93, Pan94a, Pan95, Fre96, Pan00].

The most direct procedure to simulate phase equilibria may simply consist of adequately changing the temperature or the pressure of the system and observing the occurrence of a phase transformation. This is possible via either Monte Carlo or molecular dynamics methods. Reviews of these techniques were given by Rowlinson and Widom [Row82] and by Gubbins [Gub89]. Unfortunately, important difficulties characterize these direct methods. First-order transitions [Hua63] may show hysteresis due to a large free energy barrier separating the two phases at or near to the coexistence [Fre96]. This free energy barrier consists of the free energy of the interface. The larger the area of the interface, the higher the barrier. In a normal simulation, even with large size systems, a significant number of particles are in the proximity of the interface, which can alter the outcomes of the simulation. Long equilibration times are required and it is very difficult to maintain the coexisting phases when the two values of the densities are similar. On the other hand, the direct methods do not require random particle exchanges as other techniques do [Pan00], in order to achieve the equality of the chemical potentials (material equilibrium) in the coexisting phases. For systems with

high densities the direct method would be preferable, since particle insertions are characterized by low probabilities. However, the material equilibrium by diffusion through the interface requires long simulation times under high density conditions [Yan96]. Despite these deficiencies, the direct methods provide useful information regarding the interface properties and surface tension.

Simulating the phase coexistence without interfaces is the basic and innovative idea of the Monte Carlo (MC) Gibbs ensemble method introduced by Panagiotopoulos [Pan87, Pan88]. As discussed in more detail in Chapter 2, the coexisting phases take place in separate simulation boxes. Importantly, material equilibrium between the different phases is achieved by exchanging particles between the boxes. This also represents the weakness of the method. The higher the density of at least one phase, the lower is the probability to successfully exchange the particles. Molecular dynamics (MD) implementation of the Gibbs ensemble method was proposed by Palmer and Lo using an extended system Hamiltonian [Pal94]. Baranyai and Cummings [Bar95] reported a simpler version of the MD Gibbs ensemble, using Hoover-type equations of motion [Mel93, Mel94] and particle exchanges like in the traditional MC version [Pan88]. The MD versions are able to well reproduce the results from MC Gibbs ensemble simulations. Other versions of the technique are reviewed in the literature [Pan95, Fre96, Pan00]. In particular, for multisegment or polymeric systems, versions of the Gibbs ensemble, using biased sampling methods for particle insertion, have been proposed [Sie93, Smi95, Fre96]. Also parallel versions were presented [Loy95, Ess95, Str00]. In general, the Gibbs ensemble technique is easy to implement and can be used to get information on the properties of coexisting phases from a single simulation.

Material equilibrium is achieved when the chemical potentials of all the coexisting phases are equal. Methods for calculating the (excess) chemical potential via molecular

simulation are available [Wid63, Kof97, see also Chapter 2]. The chemical potential can be calculated also from grand canonical Monte Carlo simulations [Fre96]. Performing several canonical simulations with, for example, Widom test particle insertions [Wid63] or grand canonical Monte Carlo simulations, it is possible to determine curves of the chemical potential as a function of the pressure for the different phases of interest. The coexisting condition is found at the point of intersection of the curves [Pan94a]. Möller and Fischer [Möl90] and Lotfi et al. [Lot92] used this scheme and calculated with high accuracy the coexistence properties of pure Lennard-Jones fluids. For multicomponent systems and for pure systems near the critical point this scheme requires a significant number of simulations [Pan94a], hence other techniques are preferable.

A method that does not require the equilibration or the calculation of the chemical potential of the coexisting phases, is the Gibbs-Duhem integration introduced by Kofke [Kof93a, Kof93b]. This method for pure systems consists of the numerical integration of the (first-order nonlinear) Clausius-Clapeyron differential equation [Fre96]:

$$\frac{dP}{dT} = \frac{\Delta H}{T \Delta V} \qquad (1.2)$$

where ΔH and ΔV are the differences of the enthalpy and volume in the two phases respectively. The method requires the knowledge of a coexisting point at a given temperature and pressure, which can be obtained using other techniques. A complete phase diagram is then determined by integrating Eq. (1.2), usually by a predictor-corrector method [Gea71]. Standard molecular simulations are used to calculate the right-hand side of Eq. (1.2) relative to infinitesimal and consecutive changes in the temperature. This method was applied for vapour-liquid [Kof93a, Kof93b] and solid-liquid coexistence [Agr95] of the Lennard-Jones fluid and for vapour-liquid coexistence of the two-centre Lennard-Jones fluid [Lis96a]. For multicomponent fluids, Gibbs-Duhem integration has to use particle exchanges, but exchanges can be avoided for one

component, usually the one most difficult to be exchanged. Lisal and Vacek used Gibbs-Duhem integration for mixtures of two-centre Lennard-Jones fluids [Lis96b]. Even though numerical errors in the integration and inaccuracy of the initial coexisting point may lead to deviations from the actual phase diagram, the method is very reliable, and for the solid and highly structured phases is the most efficient among the other techniques.

In a standard Monte Carlo technique, averages of the thermodynamics quantities are calculated for the parameters chosen in the simulation. For example, to obtain values of thermodynamic quantities relative to a number of different temperatures, an equivalent number of simulations have to be performed. Ferrenberg and Swendsen envisaged a method [Fer88] that, considering only a single simulation at given values of some parameters, allows calculating the thermodynamic quantities for different values of those parameters. This concept was first applied with the Ising model [Fer88, Fer89, Dru96], using multipole histogram techniques to collect data at different points of the parameter space in order to calculate a distribution for the density of the states. The same scheme, known as histogram reweighting methods, can be used for continuous-space fluids. Details of how this procedure can be applied for phase equilibria of pure and multicomponent systems are given in the references [Wil95, Pot98, Pot99, Pan98, Pan00]. The histogram reweighting methods show better accuracy in comparison with the Gibbs ensemble [Pot98] for a given amount of computer time, and they are more reliable in deriving critical points in conjunction with finite-size formalism [Pot98]. The disadvantages of these methods are that their implementation requires more effort and their efficiency decreases rapidly with increasing system size.

Considering that we wanted to study the vapour-liquid equilibria of fluids with relatively complex intermolecular potentials requiring a reasonable accuracy, the choice of the Gibbs ensemble method suited our needs best.

Transport phenomena

Statistical mechanics devoted to equilibrium systems provides, using a molecular description, phase averages of macroscopic quantities such as for example pressure and specific heat. These phase averages are obtained through probabilistic assumptions, associating a probability to each state of the system and using analytic tools for the construction of asymptotic formulae [Khi49].

Viscous flow and thermal conduction phenomena are examples of non-equilibrium systems. They are usually called transport processes. The transport properties of atomic or molecular fluids under shear are of significant scientific and technological interest. The dependence of the shear viscosity (see Chapter 2) as a function of applied strain rate is of major importance in the design of suitable lubricants, and the viscoelastic properties of polymer melts under extensional and shear flows is important to the industrial processing of plastics. The structural design of molecules under appropriate flow fields can be aided by application of simulation methods such as non-equilibrium molecular dynamics [Eva90, Dai92]. In addition, NEMD can also be used to assess rheological models such as the Rouse or Doi-Edwards models of viscoelasticity for polymer solutions and melts [Doi86], or the mode-coupling theory of Kawasaki and Gunton [Kaw73].

Shear viscosity is one of the Navier-Stokes transport coefficients [Eva90], which relate thermodynamic fluxes to their conjugate thermodynamic forces. Fluid mechanics is able to determine the macroscopic behaviour of non-equilibrium systems, but its laws

need to be supplemented with the specification of adequate boundary conditions and with thermophysical constants like the above mentioned transport coefficients. These quantities are usually obtained through experiments. One of the aims of statistical mechanics, devoted to non-equilibrium systems, is to derive these quantities from a microscopic description of the system. For dilute gases, kinetic theory [Hey98] is able to provide values of the transport coefficients in excellent agreement with the experimental data [Bar71b]. Unfortunately, this theory can not take account of higher density fluids. It has been proved that Navier-Stokes transport coefficients are non-analytic functions of the density [Dor70, Dor72], which means that a power-series expansion is not possible.

Kubo [Kub57] demonstrated that a *linear* transport coefficient can be determined through the equilibrium fluctuations of the relative flux. For example, the (Green-Kubo) relation for shear viscosity, h, in the limit of zero shear rate is:

$$h = \frac{V}{k_B T} \int_0^\infty \left\langle P_{xy}(0) P_{xy}(t) \right\rangle dt \qquad (1.3)$$

where $-P_{xy}$ is the shear stress, k_B is the Boltzmann constant and $\left\langle \; \right\rangle$ represents an equilibrium ensemble average. Eq. (1.3) and the equivalent Green-Kubo relations [Eva90] for the remaining transport coefficients can be calculated via equilibrium molecular dynamics simulations. Time correlation functions, like Eq. (1.3), are the average response of system properties to spontaneous fluctuations, which are consequently very small. The signal-to-noise ratio is poor at long times, which may give an important contribution to the integral in Eq. (1.5) or in the Green-Kubo relations for other transport coefficients. Furthermore, the finite size of the system limits the time the correlation functions can be calculated for [All87, Hey98]. To counter these limitations NEMD techniques were invented, in which the response of the system to an *induced*

perturbation is calculated. The perturbation the system experiences is larger and consequently the signal-to-noise ratio is improved. Furthermore, these techniques can consider the steady state response to the perturbation, thus the long-time behaviour of correlation functions is avoided.

A common practice to generate a non-equilibrium state in a molecular simulation, for example to induce a momentum or energy flow, is to introduce in the simulation cell boundary regions which act on the particles as momentum or energy reservoirs. The idea behind these techniques is to simulate closely what occurs in real systems. For this reason they are called 'realistic' techniques. For example Ashurst and Hoover [Ash73, Ash75] simulated planar Couette flow using fluid-like sliding walls [Lie92] and calculated the Lennard-Jones fluid shear viscosity. Tenenbaum et al. [Ten82] used stochastic boundary conditions to simulate the contact with thermal walls. These methods can not use full periodic boundary conditions, therefore they are characterized by surface effects and inhomogeneities in the thermodynamic properties of the fluid. Lees and Edwards developed periodic boundary conditions [Lee72], which enable one to simulate homogeneous planar Couette flow in which the low-Reynolds-number velocity profile is linear [Eva90].

A different approach to simulate a non-equilibrium system consists in altering the standard equations of motion, introducing 'artificial' mechanical fields, which exert the perturbation on the systems [Hoo80, Eva84c, Eva90]. Techniques adopting this concept are called 'synthetic'. Importantly, they do not suffer from surface effects and spatial inhomogeneities. Since the mechanical fields exert work on the systems, which is converted into heat, adequate thermostats have to be used [Hoo85, Eva90] to avoid heating up the system. Gosling et al. [Gos73] used a spatially periodic field to simulate a system under a sinusoidal transverse force and calculated the viscosity utilizing an

extrapolation to infinite wavelengths of the induced velocity profile. They did not use a thermostat, but they adopted an adequately small amplitude of the force, which avoided the temperature rising too rapidly. A further step in this direction is represented by the techniques adopting non Hamiltonian dynamics [Eva90]. For example, for a Nosé-Hoover [Hoo85] thermostat, the particles of the system are weakly coupled to a thermal reservoir, which can add or remove kinetic energy. This is achieved introducing an extra term in the acceleration equations. The resulting equations of motion can not be derived from a Hamiltonian. The Evans-Gillan equations of motion for heat flow [Eva90] are a modification of the standard equations of motion obtained with the introduction of a synthetic field acting on each particle. This synthetic field reproduces the effect on the system of a real temperature gradient. No Hamiltonian is known which is able to generate the Evans-Gillan equations of motion. Both Gaussian [Eva90] and SLLOD [Eva90] equations of motion, which are described in detail in Chapter 2, can not be derived from any Hamiltonian.

Green-Kubo relations can be applied not only at equilibrium, but also to adiabatic linear (weak fields) response theory [Eva90]. When thermostats are used, to keep for example the kinetic energy constant, equivalent relations can be obtained to calculate the transport coefficients [Eva90]. Evans and Morris [Eva84a] showed that time correlation functions using either Newtonian or Gaussian isothermal equations of motion for Navier-Stokes transport coefficients like shear viscosity, self diffusion coefficient and thermal conductivity, are equivalent in the large-system limit.

A further advantage of NEMD techniques is that they can be used to study the non-linear response of systems, where the Green-Kubo relations can not be used. For strong fields, the transport coefficients can be obtained directly by relating the thermodynamic fluxes to the relevant thermodynamic forces. In the NEMD SLLOD technique for planar

Couette flow, the viscosity is derived via the ratio of the shear stress to the strain rate (see Chapter 2). It is noteworthy to point out that this direct method can not be applied efficiently for weak fields because of the deterioration in the signal to noise ratio.

The most efficient way to calculate the transport coefficients in the small field regime is to use 'synthetic' NEMD techniques in conjunction with the transient-time correlation function (TTCF) relations [Eva90]. As Green-Kubo relations extract transport coefficients from fluctuations of microscopic fluxes at equilibrium, similarly, TTCF relations extract them from fluctuations of microscopic fluxes arbitrarily far from equilibrium. TTCF can be applied to genuinely non-linear transport processes. Moreover, TTCF relations in the linear response regime reduce to the Green-Kubo relations [Eva90]. It has been shown also that the TTCF and NEMD direct method lead to the same results for strong fields. The subtraction response method [Cic75, Cic76, Cic79] can also be applied in the small field regime, but it has been demonstrated that TTCF is in general preferable in the long time limit [Eva90].

Chapter 2

Theory and Computational Techniques

This chapter is dedicated to the explanation of all the technical details regarding the simulation methods we used in this work. It is meant to supply a sound description of these methods, but for a deeper understanding we refer to the literature [All87, Fre96, Pan88, Pan00, Eva89, Eva90, Hey98]. The actual implementation of the algorithms can be found elsewhere [All87, Sad99, Fre96, Eva84a]. However in Appendix 2 we report the algorithm for three-body forces, because to the best of our knowledge, it has not been given previously in the literature.

We give details of the intermolecular potentials used to study argon, krypton and xenon, in both equilibrium and non-equilibrium simulations reported here. We draw particular attention to the three-body potentials, since they represent the focus of our investigation. We introduce the Gibbs ensemble Monte Carlo technique that is used to investigate the vapour-liquid phases of the noble gases. The general concepts of non-equilibrium systems are discussed, in order to explain the algorithms used to implement planar Couette flow simulations.

2.1 Intermolecular potentials

In this work we study properties of the noble gases argon, krypton and xenon with realistic potentials, the predictions of which have been extensively proved to be in good

agreement with experimental results. The remaining stable noble gases, helium and neon, were not considered because of uncertainties arising from quantum effects. Some molecular dynamics studies and *ab initio* calculations for helium and neon have been reported recently [Azi95, Erl98, Kir98]. Several accurate intermolecular potentials are available in the literature [Mai81] for argon, krypton and xenon. We have chosen to use the intermolecular two-body potentials proposed by Barker et al. [Bar71a, Bar74] and three-body potentials proposed by Axilrod-Teller [Axi43] and Bell [Bel71], because of their well-known accuracy and the availability of intermolecular potential parameters for argon, krypton and xenon. A recent review of intermolecular potentials is available elsewhere [Sad99].

In section 2.1.1 we introduce briefly the Born-Oppenheimer approximation, which is commonly adopted in relation to intermolecular potentials. In section 2.1.2 we give details of the two-body potentials used. In section 2.1.3 a short review on three-body potentials is given.

2.1.1 Born-Oppenheimer approximation

An intermolecular potential function can be derived from quantum mechanical calculations or from experimental data fits, or from both. In general it requires the use of the *Born-Oppenheimer approximation* [Dob57]: if H is the total Hamiltonian of an atomic or molecular system and $\mathbf{Y}$ the total wave function, the state of the nuclei and the electrons can be obtained from the Schroedinger equation:

$$H\mathbf{Y} = E\mathbf{Y} \tag{2.1}$$

where E is the total energy. H is the sum of the kinetic energy of the nuclei T_n, the kinetic energy of the electrons T_e and the electrostatic potential energy U:

$$H\mathbf{Y} = (T_n + T_e + U)\,\mathbf{Y} = E\mathbf{Y} \quad . \tag{2.2}$$

In a real system, since the velocity of the nuclei is much slower than the velocity of the electrons, T_n is much smaller than T_e. For this reason the state of the electrons can be derived adopting the approximation that the nuclei are fixed. This assumption enables one to write the total wave function $\mathbf{Y}$ as a product of a first function, $\mathbf{c}$, depending only on the nuclei coordinates, and a second function, $\mathbf{f}$, depending on the electron coordinates and depending on nuclei positions in a parametric way:

$$\mathbf{Y}=\mathbf{c}(x_n)\mathbf{f}(x_n, x_e) \tag{2.3}$$

where x_e are the electron coordinates and x_n are the nuclei positions. Considering the nuclei fixed, the Schroedinger equation for the electrons becomes:

$$(T_e +U)\mathbf{f}(x_n, x_e) = \mathrm{E}\mathbf{f}(x_n, x_e) \tag{2.4}$$

Both the energy E and the wave functions $\mathbf{f}(x_n, x_e)$ depend on the configuration x_n of the nuclei, so changing x_n as a parameter changes the energy and the wave function. For many condensed systems, given the nuclei configuration x'_n, the electrons remain in the lowest energy level (ground state) $\mathrm{E}_o(x'_n)$ for a wide range of temperature and pressure values. Hence, for any configuration (x_n, x_e) it is possible to use the relative ground state eigenvalue $\mathrm{E}_o(x_n)$ to write the Schroedinger equation for the nuclei:

$$(T_n + \mathrm{E}_o(x_n)) \; \mathbf{c}(x_n)=E \; \mathbf{c}(x_n) \tag{2.5}$$

In this way $\mathrm{E}_o(x_n)$ has the role of an intermolecular potential, $u(x_n)$, to be determined by theoretical calculations or by experimental data. The Born-Oppenheimer approximation (or adiabatic approximation) states that the electrons are moving as though the nuclei were fixed in their instantaneous positions. The nuclear motion only deforms the electronic ground state; electronic transitions from the ground state to excited ones are excluded. This approximation is applicable to the noble gases [Bor54].

The intermolecular potential $u(x_n)$ in the absence of external forces may in general be written as function of the nuclear coordinates $r_1 \ldots r_N$ as [Bel76]:

$$u(r_1,...,r_N) = \sum_{i<j}^{N} u_2(r_i, r_j) + \sum_{i<j<k}^{N} u_3(r_i, r_j, r_k) + ... \qquad (2.6)$$

where u_2, u_3… are respectively pair, triplet, etc. potential functions. Experimental evidence [Bar76] indicates that this series is rapidly convergent and for many measurable properties the pairwise additive approximation (u_2 term only) is a valid description. In principle the pairwise additive approximation is inconsistent, since any quantum mechanical estimate of the pair potential u_2 must include effects due to higher terms (u_3, u_4…) [Ege94]. The wide use of the pairwise additive approximation is motivated by its simplicity. Furthermore, the above inconsistency is overcome by using effective potentials, namely, two-body potentials that accounts for the overall effects of the other multi-body interactions. The Lennard-Jones potential [Mai81, All87, Sad99] is an example of an effective two-body potential since its parameters are evaluated from bulk experimental data which include many-body effects. In our work, focused on the noble gases argon, krypton and xenon, we intend to study the role of three-body potentials (u_3), used in conjunction with an authentic two-body potential (u_2), making the assumption that higher order terms are negligible.

2.1.2 Two-body intermolecular potential

Information to determine the intermolecular potential

The general shape of the intermolecular potential function for a noble gas dimer is known. To acquire detailed information on different regions of this function, several types of experiments may be used. To achieve this task three conditions must be satisfied, as Barker pointed out [Bar76]:

1) the experimental quantity must depend reasonably sensitively on some feature of

the potential;

2) it must be possible to measure the quantity with sufficient accuracy;

3) adequate theory and computational procedures must exist to permit calculation of

the experimental quantity from a given potential or, preferably, of the potential

from the experimental quantity.

Quantum mechanics calculations can be used to accurately determine the short-range repulsion part of the potential [Mur76] (Hartre-Fock and multi-configuration Hartre-Fock calculations). This short-range contribution arises from the overlap of the electron wave functions of two atoms. It is a rapidly varying function of the interatomic distance and is usually represented as an exponential function or as an inverse high power of the interatomic distance [Mur76]. Important information on the repulsion part of the potential comes from molecular beam scattering experiments that allow high-energy total cross-section measurements [Bar76].

For the long-range attraction part (dispersion or van der Waals forces) second-order perturbation theory [Bra83, van98] provides an asymptotic form:

$$u'(r) = -\frac{C_6}{r^6} - \frac{C_8}{r^8} - \frac{C_{10}}{r^{10}} ... \qquad (2.7)$$

where r is the interatomic distance and the coefficients C_6, C_8 and C_{10} are related to the dipole and multipole oscillator strengths which can be measured from optical properties [Leo75]. The dispersion forces follow from the correlation between the fluctuating charge densities of the two atoms and they are largely independent of the overlap of the electron wave functions of the two atoms [Mur76]. In particular, the term in r^{-6} depends

on the fluctuating dipole-dipole interaction, the term in r^{-8} on the dipole-quadrupole interaction, and so on.

Van der Waals forces in inert gases enable the formation of bound states (dimers); it is possible to observe and measure band systems [Tan70] due to transitions from ground electronic states to excited electronic states of these dimers. These measurements provide information about the curvature at the potential minimum and about the anharmonicity of the potential [Bar76]. Other information on the potential function comes from gas transport properties such as viscosity, thermal conductivity, diffusion coefficients, thermal diffusion ratio and second virial coefficient [Bar76].

All the kinds of measurement discussed so far depend only on the two-body potential. For example, the second virial coefficient, B, from the equation of state

$$\frac{PV}{RT} = 1 + \frac{B}{V} + \frac{C}{V^2} + \dots \tag{2.8}$$

is related to the potential by the *classical* relationship [All87]:

$$B = \frac{2pN}{3} \int_0^\infty \left(e^{-\frac{u(r)}{kT}} - 1 \right) r^2 dr \tag{2.9}$$

It is possible to show with the Wigner-Kirkwood [Bar71a] expansion of the partition function that the quantum contributions to the second virial coefficient for argon, krypton and xenon can be neglected.

The third virial coefficient depends on both two-body and three-body potentials, and it has been shown [Bar76 and Bar68] that the inclusion of a three-body interaction, such as the Axilrod-Teller term [Axi43], can improve significantly the agreement between the calculated value and the experimental one. The same approach has to be used with condensed phase data where three-body effects are important.

The solid state, in particular the crystal structure, provides additional useful information [Bar76]. The sublimation energy at $0\ K$ depends significantly on the depth of the minimum of the two-body potential. The lattice parameter depends on the distance where the potential has a minimum. The bulk modulus near $0\ K$ is closely proportional to the second derivative of the potential at its minimum, and the $0\ K$ Debye parameter to the square root of the same quantity. The low-temperature thermal expansion coefficient is related to the third derivative of the potential near its minimum. It is particularly noteworthy that most of the pair potentials for noble gases predict the hexagonal close-packed (hcp) crystal as the most stable structure, while noble gases crystallize in face-centred cubic (fcc) structures. It has been suggested that the use of many-body potentials can instead favor the cubic structure [Nie76, Lot97a].

Liquid state properties give the opportunity to test the potential, comparing experimental values of quantities such as pressure with calculated values obtained with *Monte Carlo* and *molecular dynamics* techniques. With the same techniques it is possible to calculate the radial distribution function $g(r)$ and compare it with the one determined from X-ray and neutron diffraction data.

Argon

Most of the techniques to derive intermolecular potentials were applied to argon since a large collection of experimental data was available. An equivalent amount of data is accessible for helium but quantum effects are now important and make the calculation more difficult. In the literature several intermolecular potentials for argon were proposed [Mai81, Sad99, Azi93]. We decided to use the two-body potential by Barker, Fisher and Watts (BFW) [Bar71a] for its accuracy and also since similar analytic expressions are available for other noble gases (krypton and xenon [Bar74]).

The BFW potential is a true two-body potential since it was derived only by properties depending on two-body interactions.

The BFW potential is a linear combination of the Barker-Pompe [Bar68] (u_{BP}) and Bobetic-Barker [Bob70] (u_{BB}) potentials:

$$u_2(r) = 0.75u_{BB}(r) + 0.25u_{BP}(r) \tag{2.10}$$

where the potentials of Barker-Pompe and Bobetic-Barker have the following form:

$$u(r) = e\left[\sum_{i=0}^{5} A_i(x-1)^i \exp[a(1-x)] - \sum_{j=0}^{2} \frac{C_{2j+6}}{d + x^{2j+6}}\right]. \tag{2.11}$$

In Eq. (2.11), $x = r/r_m$ where r_m is the intermolecular separation at which the potential has a minimum value. The other parameters are summarised in Table 2.1:

Table 2.1 Parameters of the Barker-Pompe [Bar68], Bobetic-Barker [Bob70] and Barker-Fisher-Watts (BFW) [Bar71a] potentials.

	Barker-Pompe	Bobetic-Barker	Barker-Fisher-Watts
$e/k(K)$	147.70	140.235	142.095
$s(Å)$	3.7560	3.7630	3.3605
$r_m(Å)$	3.341	3.3666	3.7612
A_0	0.2349	0.29214	0.27783
A_1	-4.7735	-4.41458	-4.50431
A_2	-10.2194	-7.70182	-8.331215
A_3	-5.2905	-31.9293	-25.2696
A_4	0.0	-136.026	-102.0195
A_5	0.0	-151.0	-113.25
C_6	1.0698	1.11976	1.10727
C_8	0.1642	0.171551	0.16971325
C_{10}	0.0132	0.013748	0.013611
a	12.5	12.5	12.5
d	0.01	0.01	0.01

The BFW potential can be written as in Eq. (2.11) with the potential parameters taken from the 4th column of Table 2.1. The s term is the value where the potential is zero and it is usually defined as the atomic diameter.

Barker et al. [Bar71a] used the following experimental data to determine the potential:

1) high-energy molecular beam data;

2) the zero-temperature and -pressure lattice spacing, energy and Debye parameter, derived from specific heat measurements of solid argon;

3) the known long-range coefficients of r^{-6}, r^{-8} and r^{-10};

4) second virial coefficients;

5) the liquid-phase pressure at one temperature and density;

6) the known coefficient of the Axillord-Teller interaction [Axi43].

The BFW potential used with Axilrod-Teller three-body interactions was demonstrated to be in good agreement with several experimental properties of argon [Bar71a]. These include pressure and internal energy of the liquid state, solid state properties (specific heat, pressure), zero-shear viscosity, thermal diffusion ratio and molecular beam scattering data. Contributions from third-order dipole-quadrupole and fourth-order triple-dipole interactions cancel each other almost completely in condensed phase proprieties of argon [Bar72a and Mar99].

Krypton and xenon

The molecule-specific nature of the BFW potential is illustrated by attempts to use Eq. (2.11) for other noble gases such as krypton and xenon. Barker et al. [Bar74] reported that modifications to Eq. (2.11) were required to obtain an optimal representation for these larger noble gases. For krypton and xenon, they determined a potential of the form:

$$u_2(r) = u_0(r) + u_1(r) \qquad (2.12)$$

where $u_0(r)$ is identical to Eq. (2.11) and $u_1(r)$ is given by

$$u_1(r) = \begin{cases} e\left[P(x-1)^4 + Q(x-1)^5\right]\exp\left[a'(1-x)\right] & x > 1 \\ 0 & x \le 1 \end{cases} \tag{2.13}$$

and a', P and Q are additional parameters obtained by fitting data for differential scattering cross-sections. We have used Eqs. (2.12) and (2.13) to calculate the properties of krypton and xenon with the parameters [Bar74] summarised in Table 2.2. It is important to stress that $u_1(r)$ in Eq. (2.13) is continuous everywhere together with its first three derivatives and has a long-range asymptotic behavior.

Table 2.2 Parameters of the two-body potentials for krypton and xenon [Bar74].

	krypton	xenon
$e/k(K)$	201.9	281.0
$s(\mathring{A})$	3.573	3.890
$r_m(\mathring{A})$	4.0067	4.3623
A_0	0.23526	0.2402
A_1	-4.78686	-4.8169
A_2	-9.2	-10.9
A_3	-8.0	-25.0
A_4	-30.0	-50.7
A_5	-205.8	-200.0
C_6	1.0632	1.0544
C_8	0.1701	0.1660
C_{10}	0.0143	0.0323
P	-9.0	59.3
Q	68.67	71.1
a	12.5	12.5
a'	12.5	12.5
d	0.01	0.01

The experimental data used to derive these potentials were [Bar74]:

1) lattice spacing and cohesive energy of the crystal at 0 K;

2) bulk modulus and Debye parameter at 0 K;

3) lower vibrational level spacings derived from spectroscopic data;

4) gas viscosity data;

5) differential scattering cross sections;

6)   second virial coefficients.

For krypton all these data turned out to be consistent. For xenon the depth of the potential, e, had to be changed from the value suggested by the cohesive energy [Bar74]. In Table 2.3 some solid state proprieties at 0 K are compared with values calculated using the potentials from Baker et al. [Bar74]. The comparison indicates relatively good agreement supporting the accuracy of the potentials.

Table 2.3 Solid state proprieties at 0 K compared with values calculated using the potentials from Baker et al [Bar74].

	Nearest-neighbour distance ($Å$)	Cohesive energy (*cal/mol*)	Bulk modulus (*kbar*)	Debye parameter Q(K)
Experimental Kr	3.9922	-2666	34.3	71.9
Calculated Kr	3.9917	-2665	35.7	71.1
Experimental Xe	4.3357	-3830	36.5	64.0
Calculated Xe	4.3355	-3754	38.2	60.9

2.1.3 Many-body potentials

Modern developments in experimental techniques and computing technology have allowed an increase in the interest and the effort towards understanding many-body effects. More accurate knowledge of the 2-body potential and access to new experimental and theoretical methods has encouraged many researchers to investigate higher many-body effects, which are necessary to describe macroscopic proprieties from a microscopic viewpoint. For a comprehensive survey on this topic we refer to the review of Elrod and Saykally [Elr94]; here we intend to highlight the most important and established aspects in order to explain and justify the use of the 3-body potential functions we have chosen.

Many-body effects in any system are usually at least one order of magnitude smaller than the two-body effects, hence, any investigation on this topic requires the knowledge of an accurate two-body potential. Noble gases satisfied this requirement and consequently they were the first system studied in this context.

Even neutral atoms, with spherical charge distributions, are characterized by long-range interactions. When atoms are brought in close proximity, the instantaneous interaction between the electrons in their orbits induces mutual polarization of the charge distributions. Usually, this effect is envisaged in terms of multipole components, dipole (D), quadrupole (Q), octopole (O) etc., in the perturbed charge distributions [Bel76]. In 1943 Axilrod and Teller [Axi43], using third-order perturbation theory, found the expression for the three-body triple-dipole long-range (dispersion) energy (DDD or AT term), valid for atoms with spherical and non-overlapping charge distributions [Mur76]. In 1970, Bell [Bel70] found a more general long-range (dispersion) third-order potential:

$$u_{3bodyDisp} = DDD + DDQ + DQQ + QQQ \qquad (2.14)$$

Doran and Zucker [Dor71] used these terms plus the third-order dipole-dipole-octupole and fourth-order third-dipole to investigate the preferred crystal structure of the noble gases. They found again that this was the hcp lattice and not the fcc as experimental data show.

The effect of short-range many-body forces has not been investigated as deeply as the many-body dispersion. As for the two-body case, short-range many-body effects originate from the overlap of the wave functions of the atoms (triplets, quadruplets etc.) [Mur76]. When the overlap of the wave functions is not negligible the exchange forces due to the Pauli exclusion principle [Bra83] become relevant. Unfortunately, the derivation of higher-order exchange energies is difficult [Mur76] and established

expressions for these interactions are not available. Only recently, the role of these terms is becoming clear [LeS83, Lot97a, Buk01]. For example, Lotrich and Szalewicz [Lot97a], using fully *ab initio* three-body potentials containing short-range contributions calculated via a symmetry-adapted perturbation theory [Lot97b], computed the binding energy of solid argon. They found that the fcc crystal is favoured over the hcp crystal by 0.01%, in agreement with experimental observation.

Barker and Pompe [Bar68] in 1968 found a two-body potential for argon which, when used in conjunction with the AT potential, was able to reproduce the experimental crystal cohesive energy and third virial coefficient accurately. Even better agreement was found using the third-order QQQ and the forth-order DDD terms. Bobetic and Barker [Bob70], with the AT potential and a slightly different two-body potential, could reproduce the experimental data of specific heat, thermal expansion coefficient and the bulk modulus of crystalline argon. Barker et al. [Bar71a] using a combination of the previous potentials were able to reproduce gas, liquid and solid properties of argon with *Monte Carlo* and *molecular dynamics* simulations. Similar potentials were reported for krypton and xenon [Bar74]. Even if the pair + AT model was successful in reproducing experimental data, a theoretical justification for the exclusion of the three-body short-range terms was not given. A better evaluation and understanding of the many-body short-range potentials was necessary.

Other work followed to investigate this issue more deeply. Molecular beam scattering experiments on noble gases absorbed onto graphite substrate were performed to highlight the importance of short-range many-body effects. They could not provide a definitive solution, due to the lack of an accurate atom-substrate potential, but they showed the necessity of more accurate potentials [Azi89]. From a theoretical viewpoint, the first simultaneous implementation of the supermolecular Møller-Plesset perturbation

theory (MPPT) and intermolecular MPPT methods [Cha88] on Ar_3 showed that the second-order exchange effects were important for the total three-body effect near the potential minimum [Cha90].

A possible explanation of the contradiction between the success of the pair + AT model and the apparent importance of more recent work [Cha90] on the exchange effects can be provided by LeSar's crystal perturbation approach [LeS83]. LeSar used a 'crystal perturbation method' to obtain an approximate Hartree-Fock many-body interaction for the argon crystal. He found that the atomic orbitals in the crystal contract in comparison with those of the gas-phase atoms, resulting in less exchange repulsion. Equivalently in the gas-phase it can be thought that the higher-order exchange terms may cancel each other reducing the total short-range many-body effect significantly. McLean et al. [McL88] using the crystal perturbation many-body interaction + AT model for argon found excellent agreement with experimental solid state data.

Recently, Bukowsky and Szalewicz [Buk01] using symmetry-adapted perturbation theory potentials [Lot97b], performed simulations of liquid, gas and liquid-vapour equilibrium of argon. They found that even if three-body short-range contributions are large, cancellations occur at the interatomic distances typical for the liquid state, making the total three-body effect very similar to that given by the triple-dipole potential.

Experimental investigations

There are two main kinds of experiments to study the effects of many-body potentials: to the first kind belong those experiments that measure macroscopic properties, so they are sensitive just to the overall contribution of the many-body terms. Experiments of the second kind measure instead microscopic properties (mainly gas

phase interactions) and they are able to distinguish low-order terms in the many-body expansion.

The crystal structure of noble gases is evidence of the importance of the many-body potentials: X-ray diffraction reveals a face centered structure for the noble gases; instead the pair potentials predict a hexagonal close-packed structure (helium excluded). The inclusion of three-body terms in the potential provides a better agreement. Crystal cohesive energy measurements [Elr94] showed a 10% deviation from the pair potential prediction, suggesting again the presence of many-body effects. Crystal spacings, as well, provide information on repulsive and attractive contributions of many-body potentials.

Measurements of the radial distribution function of liquids with X-ray and neutron-scattering techniques [Ege88] give important indications, but they are not accurate enough to discriminate many-body effects. A recent detection of three-body effects was performed by Formisano et al. [For98] measuring the static structure factor $S(k)$ for xenon. The authors claimed to have obtained the first direct experimental determination of the triple-dipole Axilrod-Teller interaction. Many-body induced dipole moments and polarizability tensors can cause absorption and scattering of light in noble gases [Gui89a, Gui89b], while the two-body induced moment is exactly zero. Measurements of this kind of absorption spectrum can indicate many-body effects. It is more difficult to discern many-body effects from two-body ones using properties like viscosity, thermal conductivity and diffusion in gases.

So far we have briefly described experiments belonging to the first kind. Now we can examine those experiments measuring microscopic properties. The third virial coefficient, C in Eq. (2.8), depends on both two-and three-body potentials. Given a two-

body potential, u_2, the contribution from the three-body terms, u_3, is proportional to [Bar76]:

$$\Delta C \propto \iint e^{\left(-\frac{u_2(r_{12})+u_2(r_{13})+u_2(r_{23})}{kT}\right)} \left\{ e^{\left(-\frac{u_3(r_{12},r_{13},r_{23})}{kT}\right)} - 1 \right\} dr_{12} dr_{13} \qquad (2.15)$$

where r_{ab} is the distance between atom a and b, whereas r_{ab} is the corresponding vector. It was shown [Bar68] that ΔC contributes up to 50% of the value of the experimental C for noble gases.

The spectroscopy of van der Waals molecules provides a useful insight into the study of many body interactions. Recent high-resolution techniques have been used to measure intramolecular vibrational modes, which give direct information on the pair and higher order potentials [Elr94].

Theoretical techniques

From a theoretical viewpoint there are two complementary approaches to study the many-body effects: quantum mechanics and statistical mechanics. The latter consists mainly of *molecular dynamics* and *Monte Carlo* methods [All87]. As discussed later, modern developments in computer resources means that these methods can be used to investigate many-body potentials extensively.

Axilrod and Teller [Axi43, Axi51] were the first to use quantum mechanics calculations to find an analytic expression of a three-body potential. Nowadays there are two general methods used in *ab initio* techniques of weakly interacting systems: supermolecular and perturbation theory [Cha88]. In the supermolecular approach, the interaction energy between two systems is the difference between the energy of the complex and the monomers' energy. Perturbation theory considers the infinitely

separated monomers as the zero-order term, and the interaction energy comes from higher-order perturbations. This method provided the most important theoretical information about many-body interactions. Another relevant theoretical method is the Gaussian effective-electron model [Jan62] in which the exchange effects are approximated by placing on each atom one "effective" electron, with a Gaussian charge distribution.

A recent development of the perturbation theory technique is a simultaneous implementation of the supermolecular MPPT and intermolecular MPPT [Cha88]. This method allows the potential energy to be separated into exchange, electrostatic, induction and dispersion contributions [Szc92] as is generally done in the study of interaction forces. In this method the many-body induction (polarization) and exchange forces appear immediately in the perturbation expansion, while the many-body dispersion terms appear with each corresponding perturbation order. Another recent and promising technique is the mentioned symmetry-adapted perturbation theory [Lot97b].

Three-body dispersion potentials

Different types of interaction are possible depending on the distribution of multipole moments between the atoms. In principle, the dispersion, or long-range non-additive three-body interaction, is the sum of these various combinations of multipole moments [Bel70]. In this work, we have considered contributions from dipoles (D) and quadrupoles (Q) which are likely to make the most substantial effects on three-body dispersion:

$$u_{3bodyDisp} = u_{DDD} + u_{DDQ} + u_{DQQ} + u_{DDD4} + u_{QQQ} \quad . \tag{2.16}$$

These terms are all third-order with the exception of the contribution of the fourth-order triple dipole term (u_{DDD4}). The main contribution to the three-body dispersion

interaction is the third-order triple-dipole term (u_{DDD}). The other terms collectively (u_{DDQ} + u_{DQQ} + u_{QQQ} + u_{DDD4}) are the higher multipole contributions.

The triple-dipole potential can be evaluated from the formula proposed by Axilrod and Teller [Axi43]:

$$u_{DDD} = \frac{v_{DDD}\left(1 + 3\cos\boldsymbol{q}_i \cos\boldsymbol{q}_j \cos\boldsymbol{q}_k\right)}{\left(r_{ij}r_{ik}r_{jk}\right)^3} \tag{2.17}$$

where the angles and intermolecular separations refer to a triangular configuration of atoms (see Figure 2.1) and where v_{DDD} is the non-additive coefficient which can be estimated from observed oscillator strengths [Leo75].
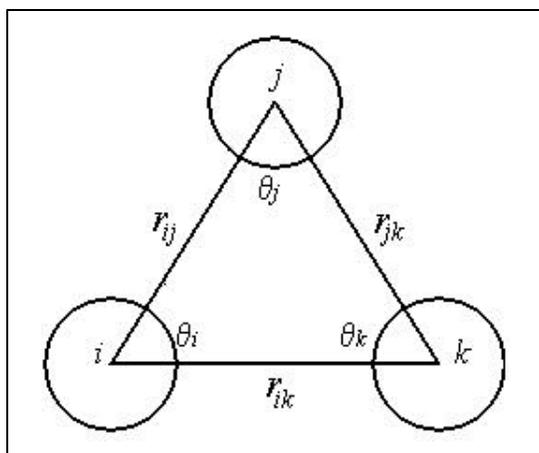
Figure 2.1 Triplet configuration of atoms i, j and k.

The contribution of the AT potential can be either negative or positive depending on the orientation adopted by the three atoms. The potential is positive for an acute triangular arrangement of atoms whereas it is negative for near linear geometries. The potential can be expected to make an overall repulsive contribution in a close-packed solid and in the liquid phase. The r^{-3} terms indicate that the magnitude of the potential is very sensitive to intermolecular separation.

Bell [Bel70] has derived the other multipolar non-additive third-order potentials:

$$u_{DDQ} = \frac{3v_{DDQ}}{16 r_{ij}^3 (r_{jk} r_{ik})^4} \times \left[9\cos\boldsymbol{q}_k - 25\cos 3\boldsymbol{q}_k + 6\cos(\boldsymbol{q}_i - \boldsymbol{q}_j)(3 + 5\cos 2\boldsymbol{q}_k) \right] \qquad (2.18)$$

$$u_{DQQ} = \frac{15v_{DQQ}}{64 r_{jk}^5 (r_{ij} r_{ik})^4} \times \begin{bmatrix} 3(\cos\boldsymbol{q}_i + 5\cos 3\boldsymbol{q}_i) + 20\cos(\boldsymbol{q}_j - \boldsymbol{q}_k)(1 - 3\cos 2\boldsymbol{q}_i) \\ + 70\cos 2(\boldsymbol{q}_j - \boldsymbol{q}_k)\cos\boldsymbol{q}_i \end{bmatrix} \qquad (2.19)$$

$$u_{QQQ} = \frac{15v_{QQQ}}{128(r_{ij} r_{ik} r_{jk})^5} \times \begin{bmatrix} -27 + 220\cos\boldsymbol{q}_i \cos\boldsymbol{q}_j \cos\boldsymbol{q}_k + 490\cos 2\boldsymbol{q}_i \cos 2\boldsymbol{q}_j \cos 2\boldsymbol{q}_k \\ + 175 \; [\cos 2(\boldsymbol{q}_i - \boldsymbol{q}_j) + \cos 2(\boldsymbol{q}_j - \boldsymbol{q}_k) + \cos 2(\boldsymbol{q}_k - \boldsymbol{q}_i)] \end{bmatrix} (2.20)$$

where Eqs (2.18), (2.19) and (2.20) represent the effect of dipole-dipole-quadrupole, dipole-quadrupole-quadrupole and quadrupole-quadrupole-quadrupole interactions, respectively. Formulae for the different ordering of the multipole moments on the three atoms (i.e., QDD, DQD, QDQ and QQD) can be generated from Eqs. (2.18) and (2.19) by cyclic permutation of the indices i, j and k. The dipole-dipole-octupole term has also been evaluated by Doran and Zucker [Dor71] but it is not considered in this work because of uncertainties in evaluating the DDO coefficient. The fourth-order triple-dipole term can be evaluated from [Dor71]:

$$u_{DDD4} = \frac{45v_{DDD4}}{64} \left[\frac{1 + \cos^2\boldsymbol{q}_i}{(r_{ik} r_{ij})^6} + \frac{1 + \cos^2\boldsymbol{q}_j}{(r_{ij} r_{jk})^6} + \frac{1 + \cos^2\boldsymbol{q}_k}{(r_{ik} r_{jk})^6} \right]. \qquad (2.21)$$

The coefficients for these three-body terms are summarised in Table 2.4.

Table 2.4 Coefficients for the three-body potentials in Eqs. (2.17), (2.18), (2.19), (2.20) and (2.21)

	argon	krypton	xenon
$\boldsymbol{n}_{DDD}$(a.u.) [a]	517.4	1554	5603
$\boldsymbol{n}_{DDQ}$(a.u.) [b]	687.5	2272	9448
$\boldsymbol{n}_{DQQ}$(a.u.) [b]	2687	9648	45770
$\boldsymbol{n}_{QQQ}$(a.u.) [b]	10639	41478	222049
$\boldsymbol{n}_{DDD4}$(a.u.) [c]	-10570	-48465	-284560

[a] from ref. [Leo75]

[b] from ref. [van98]

[c] from ref. [Bad58]

Strategies for calculating multipole moments have been discussed recently [van98]. Combining the contributions from two-body and three body interactions yields an overall intermolecular potential for the fluid:

$$u(r) = u_2(r) + u_{3bodyDisp}(r).$$ (2.22)

Table 2.5 displays the contributions to the internal energy and pressure of liquid argon that Barker et al. [Bar71a] calculated with Monte Carlo simulations using the pair + AT model, compared with the relevant experimental quantities.

Table 2.5 Contributions to the internal energy and to the pressure of liquid argon [Bar71a].

T	V	$E^{(a)}$	E^{3-body}	$E^{Quant.}$	$E^{Tot.}$	$E^{Exp.}$	$P^{(a)}$	P^{3-body}	$P^{Quant.}$	$P^{Tot.}$	$P^{Exp.}$
(K)	(cm^3/mol)	(cal/mol)	(cal/mol)	(cal/mol)	(cal/mol)	(cal/mol)	(atm)	(atm)	(atm)	(atm)	(atm)
100.00	27.04	-1525.2	87.1	15.6	-1423	-1432	239.9	364.2	42.2	646	652
100.00	29.66	-1393.6	67.9	12.5	-1313	-1324	-148.0	238.8	25.3	116	105
140.00	30.65	-1284.7	62.8	9.3	-1213	-1209	348.9	214.3	16.7	580	583
140.00	41.79	-951.4	39.5	6.4	-906	-922	-33.7	49.0	2.7	18	37
150.87	70.73	-603.8	26.6	4.6	-573	-591	34.5	13.2	1.2	49	49

[a] kinetic part + 2-body potential part

As shown in Table 2.5 the agreement with experiment is very good. Just the pressure at $T = 140$ K and $V = 41.79$ cm^3/mol diverges significantly from the experimental value. It is particularly noteworthy that the three-body contribution for the pressure plays a fundamental role to match the experimental results. For both energy and pressure, however, the quantum contribution is of minor importance.

As for argon, Barker et al. [Bar74], in using condensed phase data to derive two-body potentials for krypton and xenon in Eq. (2.12), considered three-body interactions as well. For krypton the Axilrod-Teller potential is the most relevant 3-body interaction, since the third-order dipole-quadrupole and the forth-order triple-dipole interactions

roughly cancel each other. For xenon instead, this cancellation is not complete, so Barker et al. [Bar74] considered the latter contributions deriving the two-body potential.

2.2 Monte Carlo simulation of phase equilibria

Here we give details of a molecular simulation technique, Gibbs ensemble [Pan88], which allows one to study coexisting phases of fluids. We used this technique to simulate the noble gas vapour-liquid phase. Molecular simulation is a complementary tool to the experiments and theory used to investigate the properties of thermodynamic systems and phase behavior of fluids. The latter task is not an easy one from a computational viewpoint. Phase transitions are collective phenomena that occur over long time and length scales that are difficult to reproduce by traditional molecular simulation techniques [All87]. In a system at liquid-vapour equilibria, the interface between the two phases has a prominent influence on the bulk properties if the number of particles used in the simulation is small. Hence, a large number of particles is required to avoid this problem. New simulation techniques are now available [Pan00] and amongst them the Gibbs ensemble is outstanding for its simplicity and predictive power. It eliminates the problem of the interface, performing the simulation in two different boxes, each of which contains one of the two phases considered. Even if they are separate, the boxes are correlated through particle exchanges and volume fluctuation. This characteristic permits simulations of phase equilibria utilizing a reasonable number of particles.

In section 2.2.1 we give some details of the Metropolis method, which is largely used in the Monte Carlo techniques [All87]. In section 2.2.2 we introduce the Gibbs ensemble technique, discussing the theoretical foundations and how to implement it.

2.2.1 Metropolis method

Monte Carlo simulations may be used to study molecular systems utilizing statistical mechanics. Considering for simplicity a *canonical* ensemble at temperature T, with N particles and a hamiltonian $H(r^N, p^N)$, where r^N and p^N are positions and momenta of the particles respectively, the average value of any quantity $A(r^N, p^N)$ is given by [Fre96]:

$$\langle A \rangle = \frac{\int dp^N dr^N A(r^N, p^N) \exp\left(-H(r^N, p^N)/kT\right)}{\int dp^N dr^N \exp\left(-H(r^N, p^N)/kT\right)} \qquad (2.23)$$

where the integrals are calculated over the *phase space* of the system. Usually the hamiltonian has a quadratic dependence on the momenta and for any quantity $A(p^N)$, depending just on the momenta, Eq. (2.23) is easy to calculate. More difficult is the evaluation of the average value of quantities $A(r^N)$. In this case Eq. (2.23) becomes:

$$\langle A \rangle = \frac{\int dr^N A(r^N) \exp\left(-u(r^N)/kT\right)}{\int dr^N \exp\left(-u(r^N)/kT\right)} \quad . \qquad (2.24)$$

There are different techniques to calculate Eq. (2.24). A naive method is to generate a number of random configurations (r^N) of the particles, calculate the relative values of $A(r^N)$ and energy $u(r^N)$ and to give each configuration a weight according to the Boltzmann factor $(\exp(-u(r^N)/kT))$. Unfortunately, for the majority of configurations the Boltzmann factor $(\exp(-u(r^N)/kT))$ is vanishingly small. It is more convenient instead to use the Monte Carlo importance-sampling method introduced by Metropolis et al. [Met53].

The expression in Eq. (2.24)

$$P(\mathbf{r}^N) = \frac{\exp\left(-u(\mathbf{r}^N)/kT\right)}{\int d\mathbf{r}^N \exp\left(-u(\mathbf{r}^N)/kT\right)} \tag{2.25}$$

represents the probability density to find the system in a configuration around $\mathbf{r}^N$. The Metropolis method then consists in generating configurations according to the probability density $P(\mathbf{r}^N)$, in order to consider configurations which give relevant contributions to Eq. (2.24) and then weight them evenly. An initial configuration (*old*) is chosen with a non-vanishing Boltzmann factor ($\exp(-u_{old}/kT)$), usually positioning the atoms in crystalline lattice sites. A *new* configuration is generated, for example by adding a small displacement to the old position of an atoms; the relative Boltzmann factor ($\exp(-u_{new}/kT)$) is calculated. At this stage it has to be decided whether to accept or reject the new configuration. Namely a transition probability, $\mathbf{p}(old \rightarrow new)$, to go from configuration *old* to *new* has to be determined. This transition probability can be expressed as:

$$\mathbf{p}(old \rightarrow new) = \mathbf{a}(old \rightarrow new) \times acc(old \rightarrow new) \tag{2.26}$$

where $\mathbf{a}(old \rightarrow new)$ is a transition matrix (Markov chain matrix [All87, Hoh93]) that indicates the probability to perform a trial move from *old* to *new*, and where $acc(old \rightarrow new)$ is the probability of accepting a trial move from *old* to *new*. It is useful to point out here that the Metropolis method does not need to have any knowledge about the momenta of the particles, and the temperature of the system is chosen *a priori* as a parameter.

In the Metropolis method $\mathbf{a}(old \rightarrow new)$ is chosen to be a symmetric matrix, $\mathbf{a}(old \rightarrow new) = \mathbf{a}(new \rightarrow old)$ (even if non symmetric matrixes could be chosen [Fre96]), and it is assumed that at equilibrium the average number of accepted moves

from *old* to any other *new* state is exactly cancelled by the number of reverse moves. The former is the detailed balanced condition that implies:

$$P(old)\boldsymbol{p}\,(old \rightarrow new) = P(new)\boldsymbol{p}\,(new \rightarrow old) \quad . \tag{2.27}$$

Since $\boldsymbol{a}$ is symmetric, Eq. (2.27) can be written as:

$$P(old) \times acc\,(old \rightarrow new) = P(new) \times acc\,(new \rightarrow old) \tag{2.28}$$

or:

$$\frac{acc(old \rightarrow new)}{acc(new \rightarrow old)} = \frac{P(new)}{P(old)} = \exp\!\left(-\,(u_{new} - u_{old})/kT\right) \quad . \tag{2.29}$$

Eq. (2.29) can be satisfied with many different choices for $acc\,(old \rightarrow new)$. In the Metropolis method the following choice is used:

$$acc(old \rightarrow new) = \begin{cases} P(new)/P(old) & \text{if } P(new) < P(old) \\ 1 & \text{if } P(new) \geq P(old) \end{cases} \quad . \tag{2.30}$$

This means that if $P(new) \geq P(old)$, $(u_{new} \leq u_{old})$, the trial move has to be accepted, otherwise it has to be accepted with a probability $\dfrac{P(new)}{P(old)} = \exp\!\left(-\,(u_{new} - u_{old})/kT\right)$. In the latter case a random number, from a uniform distribution in the interval [0,1], is generated and if this number is less than $acc\,(old \rightarrow new)$ the trial move is accepted. It is important to stress that the only condition imposed on $\boldsymbol{a}\,(old \rightarrow new)$ is that it has to be symmetric. For this reason several trial moves can be chosen, according to the ensemble under study. The Metropolis method, in fact, can be used for any ensemble but obviously the acceptance criteria depends on the partition function of the ensemble considered. Importantly, any choice of the trial moves has to satisfy the ergodic condition, namely that every point in configuration space can be reached in a finite number of Monte Carlo steps from any other point.

In the following sections the trial moves used in the Gibbs ensemble technique and the relative acceptance criteria are given.

2.2.2 Gibbs ensemble technique

The condition for achieving coexistence of two or more phases I, II, … at equilibrium is that the pressure and temperature in each phase must be equal $(P_I = P_{II} =… = P$; $T_I = T_{II} =… = T)$, as do the chemical potentials of all the species $(\mu_I^a = \mu_{II}^a = … = \mu^a)$. Unfortunately, it is impossible to study such systems with an ensemble where pressure, temperature and chemical potentials are fixed, since they are linearly dependent quantities, or equivalently, because constraining only intensive quantities like pressure, temperature and chemical potentials leaves the extensive quantities unbounded [Fre96].

The Gibbs ensemble technique [Pan87, Pan88] is able to study phase equilibria under the conditions that the pressure, temperature and chemical potential of the coexisting phases are equal. This is possible because even if the difference between the chemical potentials in different phases is fixed $(\Delta\mu = 0)$ the absolute values are undetermined. We applied the Gibbs ensemble technique to simulate noble gas vapour-liquid phase equilibria.

Theoretical foundations of the *NVT* Gibbs ensemble

The Gibbs ensemble Monte Carlo technique is used to simulate phase equilibria in fluids. To reproduce a macroscopic system with two coexisting phases in equilibrium, the Gibbs ensemble method simulates two separate microscopic regions within the bulk phases, away from the interface. Standard periodic boundary conditions, namely the

minimum image convention [All87], are applied. Three types of Monte Carlo moves are performed: displacements of particles within each region to satisfy internal equilibrium; fluctuations in the volume of the regions to achieve equality of the pressure; and exchanges of particles between regions to achieve equality of chemical potentials of all the species. Figure 2.2 depicts the three different moves.
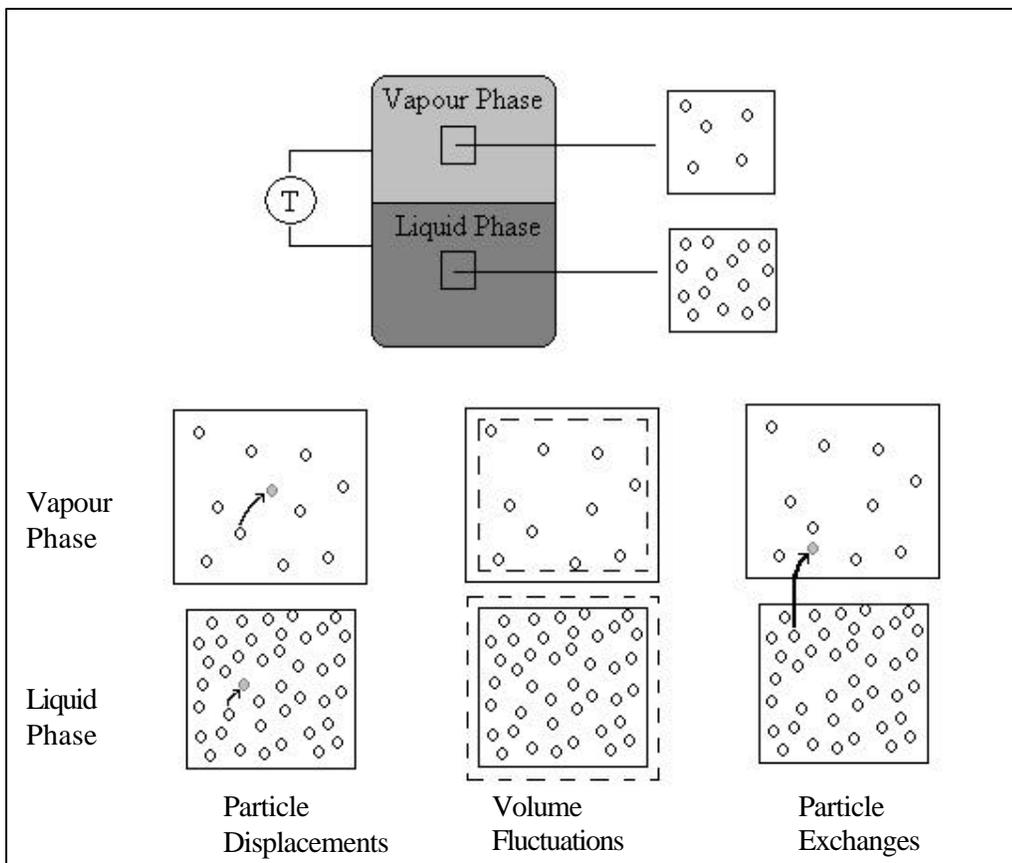
Figure 2.2 Representation of the Gibbs ensemble Monte Carlo simulation methodology.

Panagiotopoulus [Pan87] first derived the acceptance criterion from fluctuation theory, making an approximation for the particle exchange which led to a difference proportional to $1/N$, relative to the exact expression given later [Pan88]. A rigorous statistical mechanics derivation of the ensemble was reported by Smit at al. [Smi89a] and by Smit and Frenkel [Smi89b].

We are interested in the version of the Gibbs ensemble where the temperature (T), the total number of particles ($N = n_I + n_{II}$) and the total volume ($V = V_I + V_{II}$) of the two regions (boxes), *I* and *II*, are fixed. The partition function counts the number of possibilities in which N particles can be distributed in those two boxes with variable volumes, and can be expressed as [Pan95]:

$$Q_{NVT} = \frac{1}{\Lambda^{3N} N!} \sum_{n_I=0}^{N} \frac{N!}{n_I! n_{II}!} \int_0^V dV_I \, V_I^{n_I} V_{II}^{n_{II}} \int dx_I^{n_I} \exp(-u(x_I^{n_I})/kT)$$

$$\times \int dx_{II}^{n_{II}} \exp(-u(x_{II}^{n_{II}})/kT)$$

(2.31)

where **x** are the scaled coordinates of the particles in two boxes, $u(x_I^{n_{II}})$ and $u(x_{II}^{n_{II}})$ are the total potential energies in each box (depending on the intermolecular potential used) and Λ is the thermal de Broglie wavelength ($\Lambda = \sqrt{h^2/(2\pi m k_B T)}$). It can be demonstrated that the constant-volume Gibbs ensemble in the thermodynamic limit is equivalent to the canonicalensemble [Smi89a].

Eq. (2.31) states that the probability of finding the system with n_I particles in box *I* (with volume V_I) and positions $x_I^{n_I}$ and the rest of the particles in positions $x_{II}^{N-n_I}$, is given by:

$$P(n_I, V_I, x_I^{n_I}, x_{II}^{N-n_I}) \propto \frac{N! V_I^{n_I} (V_{II})^{N-n_I}}{n_I!(N-n_I)!} \exp\{-[u(x_I^{n_I}) + u(x_{II}^{N-n_I})]/kT\} \ . \qquad (2.32)$$

Using Eq. (2.32) and the detailed balance condition (Eq. (2.27)) it is possible to derive the acceptance rules [Pan88, Fre96] for trial moves for the Gibbs ensemble simulations.

For the particle displacement, the *new* configuration is generated from the *old* one, displacing randomly a particle in box *I*. The ratio between the probability relative to the *new* configuration and the probability relative to the *old* configuration is given by:

$$\frac{P(new)}{P(old)} = \frac{\exp\{-[u(\mathbf{x}_{I-new}^{n_I})]/kT\}}{\exp\{-[u(\mathbf{x}_{I-old}^{n_I})]/kT\}} \qquad . \tag{2.33}$$

Substituting Eq. (2.33) in Eq. (2.29) allows one to derive the probability of accepting the *new* configuration:

$$acc(old \rightarrow new) = \min(1; \exp\{-[u(\mathbf{x}_{I-new}^{n_I}) - u(\mathbf{x}_{I-old}^{n_I})]/kT\}) \tag{2.34}$$

In general, if the move is rejected, the *old* configuration is kept.

For the volume fluctuation, the box to be expanded is randomly chosen. If the chosen box (say box *I*) is expanded by ΔV ($V_{new}^I = V_{old}^I + \Delta V$) the other is compressed by ΔV ($V_{new}^{II} = V_{old}^{II} - \Delta V$), in order to keep the total volume constant. Using eq (2.32), the ratio between the probability relative to the *new* configuration and the probability relative to the *old* configuration can be expressed as:

$$\frac{P(new)}{P(old)} = \frac{(V_{new}^I)^{n_I}(V_{new}^{II})^{N-n_I}\exp\{-[u(\mathbf{x}_{new}^N)]/kT\}}{(V_{old}^I)^{n_I}(V_{old}^{II})^{N-n_I}\exp\{-[u(\mathbf{x}_{old}^N)]/kT\}} \tag{2.35}$$

and the probability of accepting the *new* configuration is given by:

$$acc(old \rightarrow new) = \min\left(1; \frac{(V_{new}^I)^{n_I}(V_{new}^{II})^{N-n_I}\exp\{-[u(\mathbf{x}_{new}^N)]/kT\}}{(V_{old}^I)^{n_I}(V_{old}^{II})^{N-n_I}\exp\{-[u(\mathbf{x}_{old}^N)]/kT\}}\right). \tag{2.36}$$

In writing Eq. (2.36) we assumed that the Markov chains sampled by each box are not effected by the perfectly correlated volumes. This is a good approximation away from the critical point [Pan88].

For the particle exchange one of the two boxes is randomly chosen (say box *I*). One particle is removed from the box and inserted into the other box randomly choosing the new coordinates. The ratio between the probability relative to the *new* configuration and the probability relative to the *old* configuration can be expressed as:

$$\frac{P(new)}{P(old)} = \frac{n_I!(N-n_I)!(V^I)^{n_I-1}(V-V^I)^{N-(n_I-1)}\exp\{-[u(\mathbf{x}_{new}^N)]/kT\}}{(n_I-1)!(N-(n_I-1))!(V^I)^{n_I}(V-V^I)^{N-n_I}\exp\{-[u(\mathbf{x}_{old}^N)]/kT\}} \qquad (2.37)$$

and the probability of accepting the *new* configuration is given by:

$$acc(old \rightarrow new) = \min\left(1; \frac{n_I(V-V^I)\exp\{-[u(\mathbf{x}_{new}^N)]/kT\}}{(N-n_I+1)V^I\exp\{-[u(\mathbf{x}_{old}^N)]/kT\}}\right). \qquad (2.38)$$

Implementation

The method we used to generate trial configurations is the original implementation [Pan88] where the different trial moves are performed in a fixed order. The simulation is carried in cycles. Each cycle consists of N displacements to move all the particles in each box, one attempt to change the volume and N attempts to exchange all the particles. We chose, as the initial configuration of each simulation, a face-centred cubic lattice with the desired number of particles in each box positioned randomly. A number of cycles were carried out to reach equilibrium; after this phase the macroscopic physical quantities are accumulated.

For the particle displacement moves, the *old* coordinates of the randomly selected particle (more precisely its center of mass) are changed adding random numbers between $-\Delta_{max}$ and Δ_{max}, where Δ_{max} is the maximum displacement allowed:

$$\begin{aligned}
x_{new} &\leftarrow x_{old} + (2\times rand-1)\times\Delta_{max} \\
y_{new} &\leftarrow y_{old} + (2\times rand-1)\times\Delta_{max} \\
z_{new} &\leftarrow z_{old} + (2\times rand-1)\times\Delta_{max}
\end{aligned} \qquad (2.39)$$

rand is a random number from a uniform distribution in the interval [0,1]. We chose Δ_{max} in order to have at least 50% acceptance rate. The 50% acceptance rate has no theoretical basis. Mountain and Thirumalai discussed criteria for determining the efficiency of the particle displacement moves [Mou94]. The potential energies with the

particle in the *old* position and in the new position respectively are calculated and the acceptance criterion (Eq. (2.34)) applied. It is noteworthy to stress that Eq. (2.34) requires the difference between the potential energies relative to the two configurations, so only the intermolecular energy relative to the displaced particle and the rest of the particles are required.

For the volume fluctuation move, one box, chosen randomly, is expanded by ΔV and the other compressed by $-\Delta V$. The quantity ΔV is given by:

$$\Delta V = z \times \Delta V_{max} \times \min(V^I; V^{II})$$ (2.40)

where z is a uniformly distributed random number in the range [0,1] and ΔV_{max} is the maximum fractional volume change allowed. Typically, ΔV_{max} is chosen in order to have at least 50% acceptance rate, which should guarantee that equilibrium is achieved efficiently. However, this does not have any theoretical justification. The following quantities are calculated:

$$Rat^i = \sqrt[3]{\frac{V^i_{new}}{V^i_{old}}} \qquad i = I, II$$ (2.41)

and used to scale the coordinates of the particles in each box:

$$\begin{aligned} x^i_{new} &\leftarrow x^i_{old} \times Rat^i \\ y^i_{new} &\leftarrow y^i_{old} \times Rat^i \qquad i = I, II \quad . \\ z^i_{new} &\leftarrow z^i_{old} \times Rat^i \end{aligned}$$ (2.42)

The potential energies relative to the *old* and *new* coordinates are calculated and the acceptance criterion (Eq. (2.36)) applied.

For the exchange particle move, a randomly selected particle is 'cancelled' from its original box and inserted into the other. The *new* coordinates of the particle are randomly assigned in the following way (the centre of the simulation box is the origin of the coordinates):

$$x_{new} \leftarrow (rand - 0.5) \times L$$
$$y_{new} \leftarrow (rand - 0.5) \times L \qquad L = \text{Box length} \qquad . \qquad (2.43)$$
$$z_{new} \leftarrow (rand - 0.5) \times L$$

As with the particle displacement, in order to apply the acceptance criterion in the exchange move (Eq. (2.38)) only the potential energy between the exchanged particle and the rest of the particles is required. For the exchange particle moves, in our simulations we had at least 20% acceptance rate.

NPT ensemble for binary mixtures

A constant pressure Gibbs ensemble [Pan88] can be performed only with mixtures, since for pure components the two-phase region is a line in the *P-T* plane. Thus any choice of *P* and *T* corresponds to a vanishingly small probability that the system is at the phase transition. For two-component systems the two-phase region is a finite area in the *P-T* plane [Fre96].

In the case of a *NPT* ensemble for binary mixtures, total number of particles, pressure and temperature are kept constant. The total number of particles is the sum of the total number of particles of both species, *a* and *b*, ($N = N^a + N^b$). The acceptance criterion for the particle displacement is the same as in Eq. (2.34). In the particle exchange acceptance criterion (Eq. (2.38)) n_I and $n_{II} = N\text{-}n_I$ now represent the number of particles of the species, for example *a*, being exchanged, (n_I^a and $n_{II}^a = N^a - n_I^a$) [Pan88]. The volume fluctuation acceptance criterion (Eq. (2.36)) becomes [Pan88]:

$$acc(old \rightarrow new) = \min\left(1; \frac{(V_{new}^I)^{n_I^a + n_I^b}(V_{new}^{II})^{n_{II}^a + n_{II}^b} \exp\{-[u(\mathbf{x}_{new}^N) + P(\Delta V^I + \Delta V^{II})]/kT\}}{(V_{old}^I)^{n_I^a + n_I^b}(V_{old}^{II})^{n_{II}^a + n_{II}^b} \exp\{-[u(\mathbf{x}_{old}^N)]/kT\}}\right)$$
$$(2.44)$$

where in this case it is possible that $\Delta V^I \neq -\Delta V^{II}$ since the total volume is not constant.

Calculation of the chemical potential

One of the requirements for phase equilibrium is the equality of the chemical potential (material equilibrium). A common technique used to calculate the chemical potential is the Widom test particle method [Wid63], which utilizes the interaction energy of a 'ghost' particle inserted into the system. The Gibbs ensemble technique does not rely on the knowledge of the chemical potential, but its calculation during the simulation can provide a useful check to ensure that equilibrium is achieved. During an exchange trial the energy of the particle inserted corresponds to the energy of a 'ghost' particle, so it is possible to calculate the chemical potential with ease.

Following the procedure reported by Smit et al. [Smi89b], the chemical potential is given by:

$$\boldsymbol{m} = -kT \ln\left(\frac{Q_{N+1}}{Q_N}\right) \tag{2.45}$$

where Q_N is the partition function (here we use the Gibbs ensemble Q_N, eq (2.31), at constant (N, V, T)). Substituting Eq. (2.31) in Eq. (2.45) and assuming that the boxes do not change 'identity' during the simulation, the expressions for the chemical potentials in both phases are:

$$\boldsymbol{m}_I = -kT \ln \frac{1}{\Lambda^3} \left\langle \frac{V_I}{n_I + 1} \exp(-\Delta u_I^+) \right\rangle_I$$
$$\boldsymbol{m}_{II} = -kT \ln \frac{1}{\Lambda^3} \left\langle \frac{V_{II}}{n_{II} + 1} \exp(-\Delta u_{II}^+) \right\rangle_{II} \tag{2.46}$$

where $\langle \ \rangle_I$ represents an ensemble average in the Gibbs ensemble restricted to box I and Δu_I^+ is the energy of a "ghost" particle in box I (equivalently for $\langle \ \rangle_{II}$ and Δu_{II}^+).

Finite -size effects at criticality

In general, phase transitions consist of changes between an ordered state and a disordered state. Thermodynamic properties of systems approaching the transition point can show anomalies due to complex microscopic behaviour which gives rise to observable macroscopic effects. As the disordered region of the transition approaches the ordered one, individual microscopic fluctuations start to have a strongly correlated behavior. Close to the transition, the size of the region over which this coherence extends becomes so large that it persists out to macroscopic lengths.

In the Gibbs ensemble technique the use of a finite system and periodic boundary conditions makes the study of phase transitions close to the critical points difficult. In a real system the correlation length that measures the spatial extent of density fluctuations tend to infinity. The finite size simulation cell can not capture this behaviour. Work regarding the finite-size effects on the Gibbs ensemble was reported [Rec93, Pan94b] in two- and three-dimension, for symmetric square-well and Lennard–Jones fluids.

In the Gibbs ensemble, away from the critic al region of the phase transition, the densities and compositions of both phases can be evaluated by averaging these quantities in each simulation box. When approaching the critical point, anomalous fluctuations in the density and composition are observed, due to the formation of droplets or bubbles of the opposite phase in one of the two boxes. Under these conditions, a procedure of collecting information is to use histograms of the frequency of occurrence of a certain density in each of the two boxes. The equilibrium densities can be defined as the densities relative to the peaks of the probability distribution function [Pan95]. Getting even closer to the critical point, the free energy penalty for formation of interfaces in both boxes becomes smaller [Sm89a] and exchanges of

identities of the two boxes are observed. The coexisting densities can not be determined with high accuracy [Pan95].

To predict the critical temperature and density using the Gibbs ensemble simulations the rectilinear diameter rule and scaling relationship are applied [Pan95]:

$$\frac{\boldsymbol{r}_{liq.} - \boldsymbol{r}_{vap.}}{2} = \boldsymbol{r}_{crit} + C(T_{crit.} - T); \qquad \boldsymbol{r}_{liq.} - \boldsymbol{r}_{vap.} \propto (T_{crit.} - T)^{\boldsymbol{b}} \qquad (2.47)$$

where $\boldsymbol{b}$ is an exponent that experimental results and modern theories of critical phenomena indicate to be ≈ 0.325 in three-dimension [Pan95]. It was shown that for Lennard-Jones fluids [Pan94b] the use of Eq. (2.47) predicts the critical temperature within an accuracy of $\pm 1\%$, but it gives a significantly larger uncertainty for the critical density.

At this stage we point out that it is not the interest of our work to determine critical temperature and density of the systems simulated, since our aim is only to test the interatomic potentials for coexisting phases.

Some mathematical considerations

The *NVT* Gibbs ensemble is characterized by a simple mathematical constraint that, to our knowledge, has never been highlighted. The only reference found to this issue is reported by Bruce [Bru97] which we quote to introduce the issue itself:

"In Gibbs ensemble one needs only to ensure that the overall density lies somewhere in the range between those of the coexisting phases; this constraint sharpens with the approach to the critical point" [Bru97].

Considering the one species case we can write the system of equations:

$$N = N_I + N_{II} \; ; \; V = V_I + V_{II} \; ; \; \boldsymbol{r}_I = \frac{N_I}{V_I} \; ; \; \boldsymbol{r}_{II} = \frac{N_{II}}{V_{II}} \qquad (2.48)$$

where N_I (N_{II}), V_I (V_{II}) and r_I (r_{II}) are the number of particles, the volume and

density at any time in box I (II) respectively. For each simulation the total number of

particles, N, the total volume, V, and consequently the total density ($r = \dfrac{N}{V}$) are fixed.

The question we want to answer is:

given the total density $r = \dfrac{N}{V}$, is it possible to accommodate any value of r_I and r_{II}

in box I and II at any time during the simulation?

For this purpose we have to find the solutions for the variables (unknowns) N_I, N_{II},

V_I and V_{II} of the system in Eq. (2.48), where N and V are fixed values (chosen from

the simulation) and r_I and r_{II} are any given positive values. Using simple methods of

linear algebra one can show that, if

$$r_I \neq r_{II} \tag{2.49}$$

the system in Eq. (2.48) always has the solution:

$$N_I = \frac{N - r_{II}V}{1 - \dfrac{r_{II}}{r_I}} \quad ; \quad V_I = \frac{N - r_{II}V}{r_I - r_{II}} \tag{2.50}$$

but we have to impose that :

$$0 \leq N_I \leq N \quad ; \quad 0 \leq V_I \leq V \tag{2.51}$$

which are satisfied if:

$$r_I \leq r \leq r_{II} \text{ or } r_{II} \leq r \leq r_I \quad . \tag{2.52}$$

So the answer to the above question is 'yes' as long as r_I and r_{II} satisfy Eq. (2.52).

This means that during the simulation the density in one box is at any instant greater

than or equal to r while in the other box is less than or equal to r, as physical

intuition suggests. In order to obtain the expected results, r must be chosen to lie

between the expected densities of the two coexisting phases, if they are known. If they are not known, explorative runs have to be performed. When r is chosen outside the coexisting diagram the densities in both boxes happen to fluctuate near the value of r. This is a clear signal that a different value of r has to be chosen.

In the case of *NPT* Gibbs ensemble for binary mixture we have to follow the same scheme. The total number of particles of both species, N^a and N^b, are fixed. The question we want to answer now is:

given the total number of particles of both species, N^a and N^b, is it possible to accommodate in box I and II any value of r_I and r_{II} and any value of the compositions (x_I^a, x_I^b, x_{II}^a and x_{II}^b) at any time during the simulation?

The system of equations we now have to consider is:

$$
\left.
\begin{aligned}
N^a &= N_I^a + N_{II}^a \;\;;\;\; N^b = N_I^b + N_{II}^b \\
r_I &= \frac{N_I^a + N_I^b}{V_I} \;\;;\;\; r_{II} = \frac{N^a - N_I^a + N^b - N_I^b}{V_{II}} \\
x_1^a &= \frac{N_I^a}{N_I^a + N_I^b} \;\;;\;\; x_{II}^a = \frac{N^a - N_I^a}{N^a - N_I^a + N^b - N_I^b}
\end{aligned}
\right\}
\tag{2.53}
$$

where the unknowns are V_I, V_{II}, N_I^a, N_{II}^a, N_I^b and N_{II}^b and the conditions to impose are:

$$
0 \le N_I^a \le N^a
\tag{2.54}
$$

$$
0 \le N_I^b \le N^b
\tag{2.55}
$$

which are satisfied if:

$$
\frac{x_{II}^a}{x_{II}^b} \le \frac{N^a}{N^b} \le \frac{x_I^a}{x_I^b} \;\;\; \text{for } x_I^a \ge x_{II}^a
\tag{2.56}
$$

or equivalently:

$$\frac{x_{II}^a}{1-x_{II}^a} \le \frac{N^a}{N-N^a} \le \frac{x_I^a}{1-x_I^a} \quad \text{for } x_I^a \ge x_{II}^a \quad . \tag{2.57}$$

Again, the answer to the above question is 'yes' as long as N^a and N^b satisfy Eqs. (2.56) or (2.57). Eqs. (2.56) and (2.57) state that the ratio N^a/N^b should not to be chosen greater (or less) than both x_{II}^a/x_{II}^b and x_I^a/x_I^b, as physical intuition suggests. For a *NPT* Gibbs ensemble with more than two components the answer to the above question is in general negative. This is because the equivalent system to Eq. (2.53), for example in a three-component mixture case, would contain 9 equations in 8 unknowns, which is in general not solvable. This does not mean that the simulation is not feasible. In fact, in the Gibbs ensemble technique the average values of the compositions and densities are important and not just the instantaneous values. However, Eq. (2.57) *must* be satisfied for each component. Similar considerations apply for a multicomponent *NVT* Gibbs ensemble, in which Eqs. (2.52) and (2.57) *must* be satisfied.

2.3 Synthetic Non-Equilibrium Molecular Dynamics

In this section we focus on planar Couette flow where adjacent parts of the fluid are moving with different relative velocities. Such systems are not in thermodynamic equilibrium, so viscous forces generate the transport of momentum between co-moving layers. A non-equilibrium molecular dynamics computer simulation [All87, Eva90] allows one to solve the equations of motion of each molecule of the system, and directly calculate the transport coefficients. In the following sections we describe the computer technique known as synthetic non-equilibrium molecular dynamics (NEMD) [Eva90] applied to planar Couette flow, which is used to calculate the shear viscosity of the fluid directly from the dynamics of the system (see Chapter 4).

In section 2.3.1 we give some details of homogeneous planar Couette flow, introducing the physical quantities necessary to describe the transport of momentum, namely the pressure tensor, strain rate and shear viscosity. In section 2.3.2 we describe how to derive these quantities from a microscopic description. In section 2.3.3 we give some details of the NEMD algorithm to simulate planar Couette flow, and in the last section we introduce the non-equilibrium pair distribution function which provides insight into the structure of the fluid and allows one to calculate the pressure, energy and viscosity indirectly.

2.3.1 Planar Couette flow

Figure 2.3 depicts a planar Couette flow where an atomic fluid is confined by two parallel plates of area A, distant L apart.
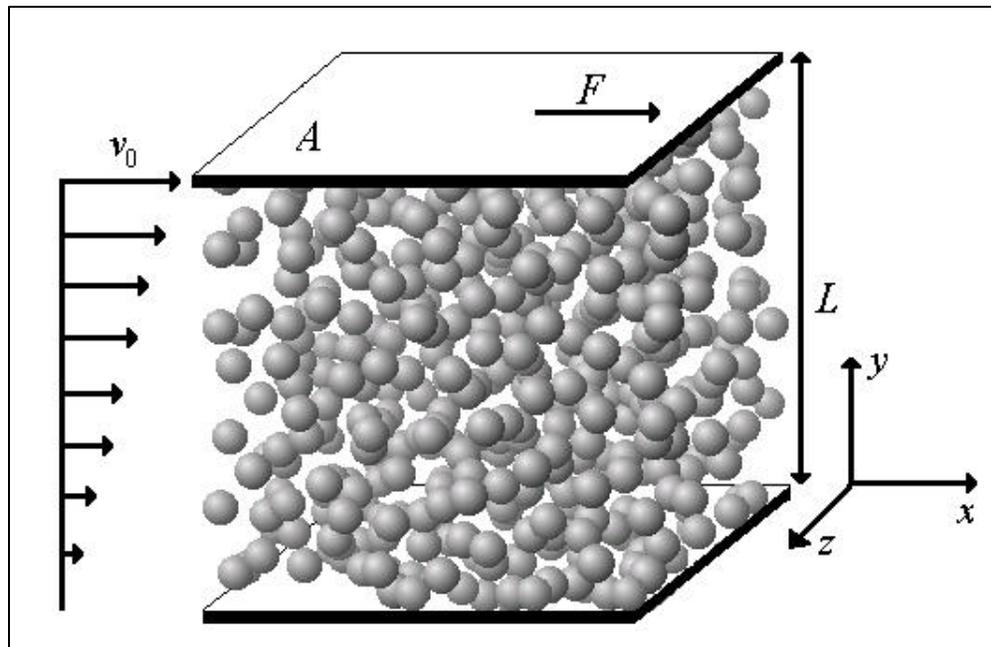
Figure 2.3 Laminar flow of an atomic fluid between a moving upper plate and stationary lower plate.

The upper plate slides in the positive x-direction at a constant velocity v_0, while the other plate is stationary. Here L is a macroscopic quantity, or more precisely, L is much larger than the range of the interatomic interactions.

Two general types of behaviour can occur depending on the nature of the fluid. With some fluids the force F used to maintain the velocity of the upper plate constant is proportional to the velocity itself; these fluids are called Newtonian. Fluids for which the force is not proportional to the velocity are called non-Newtonian [Pry66]. A more general definition states that a fluid is Newtonian if the stress exerted is directly proportional to the rate of deformation and does not depend on the deformation itself [Fer91b]; a fluid is non-Newtonian otherwise.

Consider, for simplicity, that the liquid in Figure 2.3 is Newtonian. The velocity of each atom is the sum of two different components; one is due to the thermal motion, the other is due to the streaming velocity of the fluid. For weak to moderate flows, it can be experimentally proved that the streaming velocity (directed in the x-direction) of the fluid varies linearly if measured in the y-direction, from zero at the lower plate to v_0 at the upper one. The fluid is thus said to be in a condition of steady laminar flow with a velocity gradient $\dfrac{v_0}{L}$ [Pry66]. At steady state, the force F_x^{fluid} per unit area exerted by the fluid in the x-direction on the upper plate is equal (but with opposite sign) to the force F used to drag the plate itself. F_x^{fluid} is related to v_0 by the expression:

$$\frac{F_x^{fluid}}{A} = -\frac{F}{A} = -h\frac{v_0}{L} \tag{2.58}$$

where h is the coefficient of shear viscosity, and the negative sign indicates that the force is in the negative x-direction [Pry66].

Considering Eq. (2.58), it becomes convenient to define two quantities that account for the mutually perpendicular directions of the force F_x^{fluid} (x-direction) and of the velocity gradient $\frac{v_0}{L}$ (y-direction):

$$P_{xy} = -h \frac{\partial v_x}{\partial y} \tag{2.59}$$

where $P_{xy} = \frac{F_x^{fluid}}{A} = -\frac{F}{A}$ is simply the force per unit area exerted by the fluid on the upper plate and it is a negative quantity. The x-subscript represents the direction of the force, whereas the y-subscript is the direction perpendicular to the plate. $\frac{\partial v_x}{\partial y} = \frac{v_0}{L}$ is the velocity gradient (or the strain rate). Here the x-subscript represents the component of the velocity that is not zero, and can only vary in the y-direction. The introduction of these quantities is necessary to describe satisfactorily the system under study, and their experimental measurements allow the calculation of h via Eq. (2.59).

The upper plate exerts a force $F = -P_{xy}A$ on the adjacent fluid, and during a time Δt it will transfer a momentum equal to $-P_{xy}A\Delta t$. The fluid itself will transfer this momentum to the lower plate with a rate equal to $-\frac{L}{\Delta t}$. This is the x-component of the momentum being transferred along the negative y-direction, 'layer by layer' in the fluid. The momentum flow is given by:

$$-P_{xy}A\Delta t \times \left(-\frac{L}{\Delta t}\right) = P_{xy}V \tag{2.60}$$

where V is the volume of the fluid between the plates.

In the following sections we discuss how to treat the momentum flow in Eq. (2.60) and the strain rate $\frac{\partial v_x}{\partial y}$ within a molecular description.

2.3.2 Pressure and strain rate tensors

Eq (2.60) states that the x-component of momentum flows throughout the fluid, from the upper plate to the lower. Describing a homogeneous fluid as a collection of particles interacting via central forces, the x-component of momentum can be transferred in the y-direction in two ways:

1) a particle i with thermal momentum p_{ix} and p_{iy} (x- and y-component respectively), moves, in an infinitesimal time Δt, a distance $\dfrac{p_{iy}}{m}\Delta t$ in the y-direction. Hence the particle transports its own x-component momentum p_{ix} in the y-direction at a rate

$p_{ix} \times \dfrac{\dfrac{p_{iy}}{m}\Delta t}{\Delta t} = \dfrac{p_{ix}p_{iy}}{m}$. This is valid for each particle of the fluid, so adding the contributions from all the particles, the kinetic contribution to momentum flow is given by:

$$\sum_i \frac{p_{ix}p_{iy}}{m} \quad . \tag{2.61}$$

2) The second contribution comes from the intermolecular forces. Let $F(r_{ij})$ be the magnitude of the (central) force between two particles i and j, where r_{ij} is their distance apart. The x-component of the force acting on particle j is $F(r_{ij})\dfrac{x_{ij}}{r_{ij}}$, where x_{ij} is the distance between i and j in the x-direction. In the time Δt this force will produce a change in the x-component momentum of particle j equal to $F(r_{ij})\dfrac{x_{ij}}{r_{ij}}\Delta t$.

Due to Newton's third law of dynamics, particle i experiences an equal change of momentum but of opposite sign. It can be thought that particle j gains momentum

and particle i loses it. If y_{ij} is the distance between the particles in the y-direction, the velocity with which this momentum transfer occurs is simply $\dfrac{y_{ij}}{\Delta t}$. Hence the momentum flow is $F(r_{ij})\dfrac{x_{ij}}{r_{ij}}\Delta t \times \dfrac{y_{ij}}{\Delta t} = F(r_{ij})\dfrac{x_{ij}y_{ij}}{r_{ij}}$. Adding the contributions from all the pairs of particles, the contribution to the momentum flow due to the intermolecular forces can be expressed as:

$$\sum_{i}\sum_{j>i}F(r_{ij})\frac{x_{ij}y_{ij}}{r_{ij}} \quad . \tag{2.62}$$

Adding together the contributions from Eq. (2.61) and Eq. (2.62) and using Eq. (2.60), the momentum flow for a homogeneous fluid can be related to the molecular properties as follows [Pry66, Irv50]:

$$P_{xy}V = \sum_{i}\frac{p_{ix}p_{iy}}{m} + \sum_{i}\sum_{j>i}F(r_{ij})\frac{x_{ij}y_{ij}}{r_{ij}} \quad . \tag{2.63}$$

We note here that the above expression is only valid for a homogeneous fluid. The derivation for an inhomogeneous fluid is more complex, but may be found in references [Irv50, Tod95].

Eq. (2.63) can be generalized for any kind of arbitrary flow geometry by writing similar relationships for all the possible combinations of the subscripts ($\boldsymbol{a}$, $\boldsymbol{b}$=x, y, z), which generates a 2nd rank tensor of the form [Pry66]:

$$\mathbf{P} = \begin{pmatrix} P_{xx} & P_{xy} & P_{xz} \\ P_{yx} & P_{yy} & P_{yz} \\ P_{zx} & P_{zy} & P_{zz} \end{pmatrix} \quad . \tag{2.64}$$

Eq. (2.63) is a general relationship, but for a detailed derivation with three-body forces see Appendix 2. Interchanging x and y in Eq. (2.63) it is clear that the tensor $\mathbf{P}$ is

symmetric ($P_{ab} = P_{ba}$). In the equilibrium case the off-diagonal elements are zero (in the kinetic part in Eq. (2.63), p_{ix} and p_{iy} have the same probability to be positive or negative, so the sum of the contributions from all the particles turns out to be zero) and the diagonal elements are all the same. They can be identified as the instantaneous hydrostatic pressure [All87]:

$$P^{eq} \cdot V = \frac{P^{eq.}_{xx} + P^{eq.}_{yy} + P^{eq.}_{zz}}{3} V = NkT + \frac{1}{3} \sum_i \sum_{j>i} F(r_{ij}) \bullet r_{ij} .$$
(2.65)

It is common practice to use Eq. (2.65) as the definition of hydrostatic pressure also in the non-equilibrium case and to call the tensor **P** in Eq. (2.64) the pressure tensor. In general the pressure tensor is a function of temperature, density and strain rate,

$$\mathbf{P} \equiv \mathbf{P}\left(T, r, \frac{\partial v_x}{\partial y}\right).$$

The strain rate $\dfrac{\partial v_x}{\partial y}$ can also be defined as a tensor. In general, it represents the change of the **a**-component of the velocity of the fluid in the **b**-direction, namely:

$$\frac{\partial v_a}{\partial b} , \qquad a, b = x, y, z .$$
(2.66)

Considering all the possible combinations of the suffixes, we can write the following tensor, identified as the strain rate tensor:

$$\nabla \mathbf{v} = \begin{pmatrix} \dfrac{\partial v_x}{\partial x} & \dfrac{\partial v_y}{\partial x} & \dfrac{\partial v_z}{\partial x} \\ \dfrac{\partial v_x}{\partial y} & \dfrac{\partial v_y}{\partial y} & \dfrac{\partial v_z}{\partial y} \\ \dfrac{\partial v_x}{\partial z} & \dfrac{\partial v_y}{\partial z} & \dfrac{\partial v_z}{\partial z} \end{pmatrix} .$$
(2.67)

For planar Couette flow, the only non-zero element of the tensor in Eq. (2.67) is $(\nabla \mathbf{v})_{xy} = \dfrac{\partial v_x}{\partial y}$ which is usually defined by the symbol $\dot{g}$, i.e. the strain rate.

In the following sections we will describe how synthetic NEMD may be used to simulate a planar Couette flow.

2.3.3 Synthetic NEMD for planar Couette flow

Consider a system of N particles interacting via an intermolecular potential $u(r^1,...,r^N)$ (see for example section 2.1). In a molecular dynamics simulation [All87] one solves Newton's (or Hamiltonian's) equations of motion for each particle:

$$\left.\begin{array}{l} \dot{\boldsymbol{r}}_i = \dfrac{d\boldsymbol{r}_i}{dt} = \dfrac{\boldsymbol{p}_i}{m} \\[3mm] \dot{\boldsymbol{p}}_i = \dfrac{d\boldsymbol{p}_i}{dt} = \boldsymbol{F}_i \end{array}\right\} \tag{2.68}$$

where $\boldsymbol{r}_i$ is the position of particle i, $\boldsymbol{p}_i$ its momentum and $\boldsymbol{F}_i$ is the total force acting

on the particle ($\boldsymbol{F}_i = \sum\limits_{j \neq i}^{N} \boldsymbol{F}_{ij} = -\sum\limits_{j \neq i}^{N} \dfrac{du_{ij}}{d\boldsymbol{r}_{ij}}$). Usually periodic boundary conditions

[All87] are applied to simulate bulk properties, since they minimize boundary effects. Several algorithms [All87] can be used to solve the equations of motion in Eq. (2.68); in our (NEMD) simulations we used a fourth-order Gear predictor-corrector method [All87, Eva84b, Gea71, see also below].

In order to calculate transport coefficients, *inhomogeneous* non-equilibrium molecular dynamics techniques try to closely simulate the conditions used in the experimental apparatus to measure the same transport coefficients [Lie92]. To maintain the system under non-equilibrium steady state flow, these techniques adopt boundary conditions (for example sliding walls) which, unfortunately, affect the transport properties of the fluid because the size of the simulated system is comparable with the range of the interatomic interactions [Lie92, Tod95]. For these reasons synthetic algorithms [Eva90], which use fictitious forces, were implemented to maintain the

system in a homogeneous non-equilibrium steady state. The fictitious forces continuously exert work on the system to prevent relaxation to equilibrium. This work causes a heating of the system, which must be removed by a thermostat. Fictitious forces and thermostats are introduced by modifying the Newtonian equations of motion. In what follows we describe how the synthetic NEMD SLLOD method [Eva84c, Eva90], used in our work, re-casts the equations of motion to simulate planar Couette flow.

SLLOD equations of motion

Consider a canonical ensemble of N particles at temperature T. The distribution function is:

$$f_0 = \frac{e^{-H_0/kT}}{\int e^{-H_0/kT} d\boldsymbol{r}^1 ... d\boldsymbol{r}^N d\boldsymbol{p}^1 ... d\boldsymbol{p}^N} \tag{2.69}$$

where

$$H_0 = H_0(\boldsymbol{r}^1,...,\boldsymbol{r}^N, \boldsymbol{p}^1,...,\boldsymbol{p}^N) = \sum_{i=1}^{N} \frac{\boldsymbol{p}_i \cdot \boldsymbol{p}_i}{2m} + u(\boldsymbol{r}^1,...,\boldsymbol{r}^N). \tag{2.70}$$

H_0 is seen to be the total internal energy of the system.

Consider now the instant at which the system is subject to a linear velocity profile. At time t=0 the distribution function is changed to the local distribution function

$$f_l = \frac{\exp\left[\frac{-1}{kT}\left(\sum_{i=1}^{N} \frac{(\boldsymbol{p}_i + \hat{\boldsymbol{x}}m\dot{g}y_i) \cdot (\boldsymbol{p}_i + \hat{\boldsymbol{x}}m\dot{g}y_i)}{2m} + u(\boldsymbol{r}^1,...,\boldsymbol{r}^N)\right)\right]}{\int \exp\left[\frac{-1}{kT}\left(\sum_{i=1}^{N} \frac{(\boldsymbol{p}_i + \hat{\boldsymbol{x}}m\dot{g}y_i) \cdot (\boldsymbol{p}_i + \hat{\boldsymbol{x}}m\dot{g}y_i)}{2m} + u(\boldsymbol{r}^1,...,\boldsymbol{r}^N)\right)\right] d\boldsymbol{r}^1 ... d\boldsymbol{p}^N} \tag{2.71}$$

$$(\hat{\boldsymbol{x}}: x\text{-direction unit vector})$$

by transforming the *x*-component of the velocity of each particle, imposing a linear velocity profile [Eva84c, Eva90]:

$$\dot{x}_i(0^+) = \dot{x}_i(0^-) + \dot{g}y_i \ . \tag{2.72}$$

This is a canonical ensemble (locally in equilibrium) upon which is superimposed a linear velocity profile with strain rate $\dot{g} = dv_x/dy$ (zero-wave-vector strain rate [Eva90]). It is important to realize that f_l is simply a local equilibrium distribution function, i.e. molecular relaxation has not yet taken place. The distribution function of this ensemble can be obtained by considering the response of a canonical ensemble f_0 at $t=0$ to a fictitious strain rate field $\dot{g}(t)$ where the system evolves with the following equations of motion [Eva84c]:

$$\left. \begin{aligned} \ddot{x}_i &= F_{ix}/m + \dot{g}(t)y_i \\ \ddot{y}_i &= F_{iy}/m \\ \ddot{z}_i &= F_{iz}/m \end{aligned} \right\} \quad \text{with} \quad \left. \begin{aligned} \dot{g}(t) &= 0 \quad \text{for } t < 0 \\ \dot{g}(t) &= \dot{g} \quad \text{for } t \geq 0 \end{aligned} \right\} \tag{2.73}$$

Eq. (2.73) are equivalent to the following first-order equations of motions:

$$\left. \begin{aligned} \dot{x}_i &= p_{ix}/m + \dot{g}y_i \\ \dot{y}_i &= p_{iy}/m \\ \dot{z}_i &= p_{iz}/m \end{aligned} \right\} \tag{2.74}$$

$$\left. \begin{aligned} \dot{p}_{ix} &= F_{ix} - \dot{g}p_{iy} \\ \dot{p}_{iy} &= F_{iy} \\ \dot{p}_{iz} &= F_{iz} \end{aligned} \right\} \ . \tag{2.75}$$

It is important to point out that Eq. (2.74) and Eq. (2.75) can not be derived from a Hamiltonian. p_{ix} is the peculiar (thermal) momentum ($p_{ix}^{tot.} - p_{ix}^{stream.\,vel.}$) rather than the laboratory momentum.

The shear viscosity is defined as:

$$h = -\frac{1}{\dot{g}} \left\langle P_{xy} \right\rangle_{t \to \infty} = -\frac{1}{2\dot{g}} \left\langle P_{xy} + P_{yx} \right\rangle_{t \to \infty} \tag{2.76}$$

where $\langle\ \rangle_{t\to\infty}$ represents a time average on the dynamics of the system.

Differentiating H_0 in Eq. (2.70), and using Eqs. (2.74), (2.75) and (2.63) we have the following equation:

$$\dot{H}_0 = -\dot{g}P_{xy}V \qquad (2.77)$$

which states that the work exerted by the external field in an *adiabatic* planar Couette flow results in a change of the internal energy. As a consequence, the system heats up. This behaviour is revealed by an increase of the kinetic energy, where as usual, the kinetic energy is identified with the kinetic temperature as:

$$\frac{3}{2}NkT = \sum_{i=1}^{N}\frac{p_i \cdot p_i}{2m} \quad . \qquad (2.78)$$

Since we want to simulate Couette flow at constant temperature, we need to introduce a thermostat in the equations of motion. For this purpose Eq. (2.75) is re-written as:

$$\left.\begin{array}{l} \dot{p}_{ix} = F_{ix} - \dot{g}p_{iy} - ap_{ix} \\ \dot{p}_{iy} = F_{iy} - ap_{iy} \\ \dot{p}_{iz} = F_{iz} - ap_{iz} \end{array}\right\} \qquad (2.79)$$

where a is a Gaussian thermostatting multiplier [Eva90] derived by constraining the kinetic energy (hence the temperature) to be constant:

$$\frac{dT}{dt} = 0 \quad \Rightarrow \quad \frac{d\left(\sum_{i=1}^{N}\dfrac{p_i \cdot p_i}{2m}\right)}{dt} = 0 \quad \Rightarrow \quad a = \frac{\sum_{i=1}^{N}\left(F_i \cdot p_i - \dot{g}p_{ix}p_{iy}\right)}{\sum_{i=1}^{N}p_i \cdot p_i} \quad . \qquad (2.80)$$

In Eqs. (2.74), (2.79) and (2.80) it is assumed that the linear velocity profile is stable, which is true at low Reynolds number [Eva90].

The SLLOD equations of motions must be implemented with compatible periodic boundary conditions [Eva90]. For planar Couette flow (Eq. (2.74) and Eq. (2.79)), Lees-

Edwards boundary conditions [All87, Eva90] can be used. In the next section we give some details of these boundary conditions.
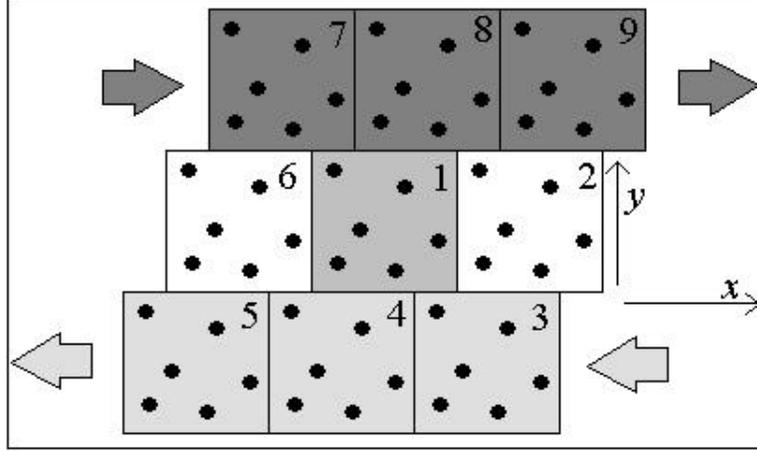
Figure 2.4 Representation of the Lees-Edwards boundary conditions [All87, Eva90].

Lees-Edwards boundary conditions

Figure 2.4 depicts an infinite periodic system subjected to shear in the x-y plane. Box 1 is the simulation box. The boxes in the middle layer (2, 1 and 6) are stationary. Boxes in the lower layer (3, 4 and 5) move in the negative x-direction at a speed $\dot{g}L$, where L is the length of the (cubic) box. The boxes in the upper layer (7, 8 and 9) move in the positive x-direction at a speed $\dot{g}L$. At each step of the simulation the relative distances (x_{ij}, y_{ij} and z_{ij}) between pairs of particles i and j are calculated with Lees-Edwards boundary conditions [All87, Eva90] in the following way:

$$
\begin{aligned}
x_{ij} &\leftarrow x_{ij} - dxd \times anint(y_{ij}/L) \times L \\
x_{ij} &\leftarrow x_{ij} - anint(x_{ij}/L) \times L \\
y_{ij} &\leftarrow y_{ij} - anint(y_{ij}/L) \times L \\
z_{ij} &\leftarrow z_{ij} - anint(z_{ij}/L) \times L
\end{aligned}
\qquad (2.81)
$$

In Eq. (2.81)

$$
dxd = mod(\dot{g} \times t_{\text{el.}}; L) \ , \qquad (2.82)
$$

where $mod(a \; ; \; b)$ is a function that returns the remainder of the division of b into a and $t_{\text{el.}}$ is time elapsed during the simulation. $anint(a)$ is a function that returns the nearest integer to a.

It is convenient to replace particles in the simulation box as they cross the boundaries. After each step of the simulation, the following algorithm (similar to Eq. (2.81)) must be used for the coordinates (x_i, y_i, z_i) of the particles:

$$
\begin{aligned}
x_i &\leftarrow x_i - dxd \times anint(y_i / L) \times L \\
x_i &\leftarrow x_i - anint(x_i / L) \times L \\
y_i &\leftarrow y_i - anint(y_i / L) \times L \\
z_i &\leftarrow z_i - anint(z_i / L) \times L
\end{aligned}
\tag{2.83}
$$

where we note that the origin of the coordinate system is the centre of the simulation box. If the particle crosses the lower x-z face of the simulation box it will 'reappear' at the upper x-z face, and the streaming velocity ($\dot{g}L$) will be added to its total velocity. If it crosses the upper x-z face reappearing in the lower x-z face, the streaming velocity ($\dot{g}L$) will be subtracted from its total velocity. In the other cases the total velocity is not changed.

Gear predictor-corrector method

To solve the first-order SLLOD equations of motion (Eqs. (2.74) and (2.79)), we used a fourth-order Gear predictor-corrector method [All87, Eva84b, Gea71] for its efficiency and accuracy. Despite its 4th order accuracy it requires only first derivatives of the intermolecular potential which is calculated once per time-step. Let r_i be the position of particle i, the scaled time derivatives can be defined as:

$$
\boldsymbol{r}_{1i} = \Delta t \left(\frac{dr_i}{dt}\right) \; ; \boldsymbol{r}_{2i} = \frac{1}{2}\Delta t^2 \left(\frac{d^2 r_i}{dt^2}\right) \; ; \boldsymbol{r}_{2i} = \frac{1}{6}\Delta t^3 \left(\frac{d^3 r_i}{dt^3}\right) \; ; \boldsymbol{r}_{2i} = \frac{1}{24}\Delta t^4 \left(\frac{d^4 r_i}{dt^4}\right) \tag{2.84}
$$

where Δt is the time step. Equivalently for the momentum $\boldsymbol{p}_i$, we have:

$$\boldsymbol{p}_{1i} = \Delta t\left(\frac{d\boldsymbol{p}_i}{dt}\right) \; ; \boldsymbol{p}_{2i} = \frac{1}{2}\Delta t^2\left(\frac{d^2\boldsymbol{p}_i}{dt^2}\right) \; ; \boldsymbol{p}_{3i} = \frac{1}{6}\Delta t^3\left(\frac{d^3\boldsymbol{p}_i}{dt^3}\right) \; ; \boldsymbol{p}_{4i} = \frac{1}{24}\Delta t^4\left(\frac{d^4\boldsymbol{p}_i}{dt^4}\right) \quad (2.85)$$

The Taylor series expansion for $\boldsymbol{r}_i$ and $\boldsymbol{p}_i$ is truncated at the 4th order, and using a matrix form we can write the predicted values (superscript p) of $\boldsymbol{r}_i$ and $\boldsymbol{p}_i$ and their derivatives in the following way:

$$\begin{pmatrix} \boldsymbol{r}_i^{\text{p}}(t+\Delta t) \\ \boldsymbol{r}_{i1}^{\text{p}}(t+\Delta t) \\ \boldsymbol{r}_{i2}^{\text{p}}(t+\Delta t) \\ \boldsymbol{r}_{i3}^{\text{p}}(t+\Delta t) \\ \boldsymbol{r}_{i4}^{\text{p}}(t+\Delta t) \end{pmatrix} = \begin{pmatrix} 1 & 1 & 1 & 1 & 1 \\ 0 & 1 & 2 & 3 & 4 \\ 0 & 0 & 1 & 3 & 6 \\ 0 & 0 & 0 & 1 & 4 \\ 0 & 0 & 0 & 0 & 1 \end{pmatrix} \begin{pmatrix} \boldsymbol{r}_i(t) \\ \boldsymbol{r}_{i1}(t) \\ \boldsymbol{r}_{i2}(t) \\ \boldsymbol{r}_{i3}(t) \\ \boldsymbol{r}_{i4}(t) \end{pmatrix} \quad (2.86)$$

$$\begin{pmatrix} \boldsymbol{p}_i^{\text{p}}(t+\Delta t) \\ \boldsymbol{p}_{1i}^{\text{p}}(t+\Delta t) \\ \boldsymbol{p}_{2i}^{\text{p}}(t+\Delta t) \\ \boldsymbol{p}_{3i}^{\text{p}}(t+\Delta t) \\ \boldsymbol{p}_{4i}^{\text{p}}(t+\Delta t) \end{pmatrix} = \begin{pmatrix} 1 & 1 & 1 & 1 & 1 \\ 0 & 1 & 2 & 3 & 4 \\ 0 & 0 & 1 & 3 & 6 \\ 0 & 0 & 0 & 1 & 4 \\ 0 & 0 & 0 & 0 & 1 \end{pmatrix} \begin{pmatrix} \boldsymbol{p}_i(t) \\ \boldsymbol{p}_{1i}(t) \\ \boldsymbol{p}_{2i}(t) \\ \boldsymbol{p}_{3i}(t) \\ \boldsymbol{p}_{4i}(t) \end{pmatrix} \quad (2.87)$$

When the predicted values are calculated, Lees-Edwards periodic boundary conditions (Eq. (2.83)) are applied to reintroduce particles into the simulation box, which may have crossed the boundaries. The relative distances between pairs of particles are first calculated by Eq. (2.81) and then used to determine the forces acting on each atom. Finally, Eq. (2.74) and Eq. (2.79) are used in the corrector step to calculate the corrected values (superscript c) of $\boldsymbol{r}_i$ and $\boldsymbol{p}_i$ and their derivatives:

$$\begin{pmatrix} \boldsymbol{r}_i^{\text{c}}(t+\Delta t) \\ \boldsymbol{r}_{i1}^{\text{c}}(t+\Delta t) \\ \boldsymbol{r}_{i2}^{\text{c}}(t+\Delta t) \\ \boldsymbol{r}_{i3}^{\text{c}}(t+\Delta t) \\ \boldsymbol{r}_{i4}^{\text{c}}(t+\Delta t) \end{pmatrix} = \begin{pmatrix} \boldsymbol{r}_i^{\text{p}}(t+\Delta t) \\ \boldsymbol{r}_{i1}^{\text{p}}(t+\Delta t) \\ \boldsymbol{r}_{i2}^{\text{p}}(t+\Delta t) \\ \boldsymbol{r}_{i3}^{\text{p}}(t+\Delta t) \\ \boldsymbol{r}_{i4}^{\text{p}}(t+\Delta t) \end{pmatrix} + \Delta\boldsymbol{r}_i \begin{pmatrix} c_0 \\ c_1 \\ c_2 \\ c_3 \\ c_4 \end{pmatrix} \quad (2.88)$$

$$\begin{pmatrix} \boldsymbol{p}_i^{\mathrm{c}}(t+\Delta t) \\ \boldsymbol{p}_{i1}^{\mathrm{c}}(t+\Delta t) \\ \boldsymbol{p}_{i2}^{\mathrm{c}}(t+\Delta t) \\ \boldsymbol{p}_{i3}^{\mathrm{c}}(t+\Delta t) \\ \boldsymbol{p}_{i4}^{\mathrm{c}}(t+\Delta t) \end{pmatrix} = \begin{pmatrix} \boldsymbol{p}_i^{\mathrm{p}}(t+\Delta t) \\ \boldsymbol{p}_{i1}^{\mathrm{p}}(t+\Delta t) \\ \boldsymbol{p}_{i2}^{\mathrm{p}}(t+\Delta t) \\ \boldsymbol{p}_{i3}^{\mathrm{p}}(t+\Delta t) \\ \boldsymbol{p}_{i4}^{\mathrm{p}}(t+\Delta t) \end{pmatrix} + \Delta\boldsymbol{p}_i \begin{pmatrix} c_0 \\ c_1 \\ c_2 \\ c_3 \\ c_4 \end{pmatrix} \tag{2.89}$$

where:

$$\Delta\boldsymbol{r}_i = \begin{pmatrix} x_{1i} - (p_{ix} + \dot{\boldsymbol{g}}y_i)\Delta t \\ y_{1i} - p_{iy}\Delta t \\ z_{1i} - p_{iz}\Delta t \end{pmatrix} \tag{2.90}$$

$$\Delta\boldsymbol{p}_i = \begin{pmatrix} p_{1ix} - (F_{ix} - \boldsymbol{a}p_{ix} - \dot{\boldsymbol{g}}p_{iy})\Delta t \\ p_{1iy} - (F_{iy} - \boldsymbol{a}p_{iy})\Delta t \\ p_{1iz} - (F_{iz} - \boldsymbol{a}p_{iz})\Delta t \end{pmatrix}. \tag{2.91}$$

Here c_0, c_1, c_2, c_3 and c_4 are the corrector coefficients which depend upon the order of the differential equation being solved [Gea71]. In our case, $c_0 = 251/720$, $c_1 = 1$, $c_2 = 11/12$, $c_3 = 1/3$ and $c_4 = 1/24$.

Other methods can be used to integrate equations of motion of the particles. The commonly used leap frog method [Ver67] solves second order equations of motion, hence it is not suitable to solve first order Eqs. (2.74) and (2.79). The Runge-Kutta method [Gea71] is appropriate but expensive computationally. We have chosen to use the fourth-order Gear predictor-corrector method for its good accuracy and because of programming convenience.

2.3.4 Non-equilibrium pair distribution functions

Given a canonical ensemble (*NVT*), where the origin of the coordinate system is arbitrarily chosen, it is possible to define distribution functions for the particle positions. The simplest such function is the pair (2nd order) distribution function g($\boldsymbol{r}_1$, $\boldsymbol{r}_2$). In a homogeneous atomic fluid, it is proportional to the probability of finding a particle at $\boldsymbol{r}_2$

in a volume element $d\boldsymbol{r}_2$ if, at the same time, there is a particle at $\boldsymbol{r}_1$ in volume $d\boldsymbol{r}_1$ [Ege94]. This function is useful since it can be easily calculated from a molecular simulation, providing insight into the liquid structure. It can also be measured experimentally [Ege94], allowing a direct comparison between theory and experiment. Furthermore, the pair distribution function, when known, provides an alternative way to calculate any pair function of the system, such as the two-body configurational pressure, energy and viscosity. Hence it can be used to test the correctness of those pair functions calculated directly from a molecular simulation. Higher order distribution functions can be defined in a similar way [Ege94].

For a homogeneous liquid in thermal equilibrium or under steady state uniform flow, $g(\boldsymbol{r}_1, \boldsymbol{r}_2)$ does not depend upon the choice of the origin of the coordinates [Ege94]. Hence $g(\boldsymbol{r}_1, \boldsymbol{r}_2)$ depends upon the difference $\boldsymbol{r} = \boldsymbol{r}_1 - \boldsymbol{r}_2$ and can be defined as an ensemble average over all possible pairs [All87]:

$$g(\boldsymbol{r}) = \frac{V}{N^2}\left\langle \sum_{i=1}^{N}\sum_{j>i}^{N} \boldsymbol{d}(\boldsymbol{r} - \boldsymbol{r}_{ij}) \right\rangle \tag{2.92}$$

where $\boldsymbol{d}(\boldsymbol{r} - \boldsymbol{r}_{ij})$ is the delta function. Further, for an isotropic liquid $g(\boldsymbol{r})$ depends only upon the magnitude of $\boldsymbol{r}$, so it is a spherically symmetrical function. In this case $g(\boldsymbol{r})$ is easily calculated as:

$$g(r) = \frac{\langle N_r \rangle}{4\boldsymbol{p}\boldsymbol{r}\, r^2 dr} \tag{2.93}$$

where $\langle N_r \rangle$ is the average number of particles between a spherical shell of radius r and thickness dr. In planar Couette flow $g(\boldsymbol{r})$ is not a spherically symmetrical function and can be approximated as [Gre52, Han80]:

$$g(\boldsymbol{r}) = g(r) + \dot{\boldsymbol{g}}\,\boldsymbol{n}(r)\sin^2\boldsymbol{q}\,\sin\boldsymbol{f}\cos\boldsymbol{f} \tag{2.94}$$

where we use the polar coordinates:

$$\left. \begin{array}{l} x = r \sin \boldsymbol{q} \cos \boldsymbol{f} \\ y = r \sin \boldsymbol{q} \sin \boldsymbol{f} \\ z = r \cos \boldsymbol{q} \end{array} \right\} .$$
(2.95)

In Eq. (2.94), $g(r)$ is the standard radial distribution function (Eq. 2.93). In this work we have calculated this quantity for a system in equilibrium and for planar Couette flow (see Chapter 4). The function $\boldsymbol{n}(r)$ represents the purely radial part of the distortion and it can be estimated by the expression [Han80]:

$$\boldsymbol{n}(r) = \frac{15}{8\boldsymbol{p}} \frac{1}{\boldsymbol{\dot{g}r} \, r^2 dr} \left\langle \frac{x_{ij} \, y_{ij}}{r_{ij}^2} \right\rangle$$
(2.96)

where $\left\langle \dfrac{x_{ij} \, y_{ij}}{r_{ij}^2} \right\rangle$ is the average of the quantity $\dfrac{x_{ij} \, y_{ij}}{r_{ij}^2}$ for each particle contained in a spherical shell of radius r and thickness dr. We have calculated $\boldsymbol{n}(r)$ for planar Couette flow (see Chapter 4). For a system in equilibrium $\boldsymbol{n}(r)$ is zero.

In what follows we give the expressions of the two-body potential contributions to the pressure, energy and viscosity in terms of $g(r)$ and $\boldsymbol{n}(r)$.

Two-body potential pressure, energy and viscosity as functions of $g(r)$ and $\boldsymbol{n}(r)$

The two-body potential contribution for the pressure can be written as [All87]:

$$P^{2b} = \frac{1}{3V} \sum_{i=1}^{N} \sum_{j>i}^{N} (F_{ix}^{2b} x + F_{iy}^{2b} y + F_{iz}^{2b} z) =$$

$$\frac{1}{3V} \sum_{i=1}^{N} \sum_{j>i}^{N} \left(-\frac{x}{r} \frac{du^{2b}}{dr} x - \frac{y}{r} \frac{du^{2b}}{dr} y - \frac{z}{r} \frac{du^{2b}}{dr} z \right) = -\frac{1}{3V} \sum_{i=1}^{N} \sum_{j>i}^{N} \left(r \frac{du^{2b}}{dr} \right) .$$
(2.97)

Using Eq. (2.92) and Eq.(2.94) we can write:

$$P^{2b} = -\frac{1}{3}\frac{r^2}{2}\int g(r)r\frac{du^{2b}}{dr}r^2\sin\mathbf{q}\,d\mathbf{q}\,d\mathbf{f}\,dr =$$

$$-\frac{r^2}{6}\int(g(r)+\dot{\mathbf{g}}\,\mathbf{n}(r)\sin^2\mathbf{q}\sin\mathbf{f}\cos\mathbf{f})\frac{du^{2b}}{dr}r^3\sin\mathbf{q}\,d\mathbf{q}\,d\mathbf{f}\,dr =$$

$$-\frac{r^2}{6}\int g(r)\frac{du^{2b}}{dr}r^3\sin\mathbf{q}\,d\mathbf{q}\,d\mathbf{f}\,dr -$$

$$\frac{r^2}{6}\int\dot{\mathbf{g}}\,\mathbf{n}(r)\sin^2\mathbf{q}\sin\mathbf{f}\cos\mathbf{f}\frac{du^{2b}}{dr}r^3\sin\mathbf{q}\,d\mathbf{q}\,d\mathbf{f}\,dr$$

$$(2.98)$$

where:

$$-\frac{r^2}{6}\int\dot{\mathbf{g}}\,\mathbf{n}(r)\sin^2\mathbf{q}\sin\mathbf{f}\cos\mathbf{f}\frac{du^{2b}}{dr}r^3\sin\mathbf{q}\,d\mathbf{q}\,d\mathbf{f}\,dr = 0 \qquad (2.99)$$

since:

$$\int_0^{2\mathbf{p}}\sin\mathbf{f}\cos\mathbf{f}\,d\mathbf{f} = 0 \qquad . \qquad (2.100)$$

Hence:

$$P^{2b} = -\frac{r^2}{6}\int g(r)\frac{du^{2b}}{dr}r^3\sin\mathbf{q}\,d\mathbf{q}\,d\mathbf{f}\,dr = -\frac{2\mathbf{p}r^2}{3}\int_0^{\infty}g(r)\frac{du^{2b}}{dr}r^3dr \quad . \qquad (2.101)$$

Equivalently for the two-body potential energy we can write:

$$E^{2b} = 2\mathbf{p}N\mathbf{r}\int_0^{\infty}g(r)u^{2b}r^2dr \qquad . \qquad (2.102)$$

Eq. (2.101) and Eq. (2.102) state that P^{2b} and E^{2b} do not depend on the radial part of the distortion, $\mathbf{n}(r)$, and the only dependence on the shear rate $\dot{\mathbf{g}}$ comes from the distortion of $g(r)$ under shear (since $g(r)^{equil.} \neq g(r)^{non-equil.}$). Following the same procedure we can write a similar expression for the 2-body potential shear contribution to the viscosity which depends only on $\mathbf{n}(r)$:

$$\mathbf{h}^{2b} = \frac{2\mathbf{p}r^2}{15}\int_0^{\infty}\mathbf{n}(r)\frac{du^{2b}}{dr}r^3dr \quad . \qquad (2.103)$$

Chapter 3

Investigation of Three-Body Interactions on the Phase Behaviour of Noble Gases

In the following sections we report the results obtained studying the role of three-body interatomic potentials on noble gas coexisting phases. Section 3.1 gives details of the Gibbs ensemble simulations for vapour-liquid coexisting phases of argon, krypton and xenon as pure fluids and of an argon-krypton mixture. In section 3.2 we report the analytic expression of an effective potential which we found to reproduce the main feature of the two-body + three-body potentials. The significance of this relationship is that three-body interactions can be estimated with sufficient accuracy from two-body interactions without incurring the computational penalty of three-body calculations. The relationship has the potential of improving both the accuracy and predictive value of pair interaction molecular simulations.

3.1 Vapour-liquid coexisting phases of noble gases

The aim of this work is to investigate the role of the dipole-dipole-dipole term and other mutipole three-body dispersion terms on the vapour-liquid phases observed for argon, krypton and xenon. As discussed in Chapter 2, we have used the potentials

proposed by Barker et al. [Bar71a, Bar74, see Eqs. (2.11), (2.12) and (2.13)] for the two-body interactions. The three-body interactions were obtained from considering the dipole-dipole-dipole (third-order DDD or Axilrod-Teller term, Eq. (2.17)), the dipole-dipole-quadrupole (third-order DDQ, Eq. (2.18)) the dipole-quadrupole-quadrupole (third-order DQQ, Eq. (2.19)), quadrupole-quadrupole-quadrupole (third-order QQQ, Eq. (2.20)) and the dipole-dipole-dipole (forth-order DDD, Eq. (2.21)).

3.1.1 Simulation details

Pure fluids

The *NVT* Gibbs ensemble technique (for details see Chapter 2) was implemented for a system of 500 atoms. The simulations were performed in cycles consisting typically of 500 attempted displacements, an attempted volume change and 500 interchange attempts. Typically, 1000-1500 cycles were used for equilibration and a further 1500-2000 cycles were used to accumulate ensemble averages. The normal convention was adopted for the reduced density ($r^* = rs^3$), temperature ($T^* = kT/e$), energy ($E^* = E/e$), pressure ($P^* = Ps^3/e$) and chemical potential ($m^* = m/e$).

Periodic boundary conditions were applied. The two-body potentials were truncated at half the box length and appropriate long range correction terms (see Appendix 1) were evaluated to recover the contribution to pressure, energy and chemical potential of the full intermolecular potential. Some care needs to be taken with the three-body potentials because the application of a periodic boundary can potentially destroy the position-invariance of three particles (see Appendix 2). We examined the behaviour of the three-body terms for many thousands of different configurations and intermolecular separations. All the three-body terms asymptote rapidly to zero with increasing

intermolecular separation. For a system size of 500 or more atoms, we found truncating the three-body potentials at intermolecular separations greater than a quarter of the length of the simulation box to be an excellent approximation to the full potential that also avoided the problem of three-body invariance to periodic boundary conditions.

The chemical potential was determined from the equation proposed by Smit et al. [Smi89a, see Chapter 2]. The uncertainties in the ensemble averages for density, temperature, energy and pressure were calculated by dividing the post-equilibrium results into ten sections. The estimated errors represent the standard deviations of the section averages. An error estimate for the chemical potential cannot be estimated in this way because it is the average of the entire post-equilibrium simulation.

Binary mixture

The *NPT* Gibbs ensemble technique was used for an argon-krypton mixture. The details of the simulations are similar to those discussed above for the pure fluids. In this work we analyzed the pressure-composition behaviour of the mixture and compared it with experimental data. The pressure-density behaviour was also studied.

The intermolecular potentials mentioned previously were developed originally for pure fluids, but they can be applied directly to binary mixtures by assuming suitable combining rules for the intermolecular parameters. In general if we denote the energy-like parameters $\boldsymbol{n}$ and $\boldsymbol{e}$ (see Chapter 2) by the symbol W, the cross potential parameters of interacting pairs and triplets can be calculated from:

$$\left. \begin{array}{l} W_{ijk} = \sqrt[3]{W_{iii}W_{jjj}W_{kkk}} \\ W_{ij} = \sqrt[2]{W_{ii}W_{jj}} \end{array} \right\} \qquad (3.1)$$

In general if we denote all the remaining parameters such as s, A, C_6 etc (see Chapter 2) by the symbol Y, the cross potential parameters of interacting pairs can be calculated from:

$$Y_{ij} = \frac{Y_{ii} + Y_{jj}}{2}$$ (3.2)

In the argon-krypton mixture simulations the potential parameters of argon e and s were used to obtain reduced quantities in the standard way. It is important to stress that these commonly used combining rules do not have physical rationale.

The three-body simulations commonly require 20 and 12 CPU hrs on the Fujitsu VPP300 and NEC SX-4/32 supercomputers, respectively.

3.1.2 Results and discussion

Pure fluids

The results of Gibbs ensemble simulations for the vapour-liquid properties of argon, krypton and xenon are reported in Tables 3.1-3.6. A comparison of simulation results with experiment is given in Figures 3.1, 3.3 and 3.4. The relative contribution to energy of the various three-body interactions for the liquid phase of argon is illustrated in Figure 3.2. The total pressure versus the temperature is reported in Figure 3.5.

Table 3.1 Vapour-liquid coexistence properties of argon from molecular simulation using the two-body BFW potential [Bar71a].

T^*	r_L^*	P_L^*	E_L^*	m_L^*	r_V^*	P_V^*	E_V^*	m_V^*
0.700	0.806(4)	-0.018(38)	-5.18(3)	-3.67	0.006(1)	0.004(1)	-0.06(2)	-3.70
0.750	0.781(3)	0.007(21)	-4.98(2)	-3.67	0.008(1)	0.006(1)	-0.08(3)	-3.68
0.825	0.741(4)	0.020(14)	-4.66(3)	-3.43	0.021(2)	0.015(2)	-0.19(3)	-3.39
0.850	0.727(5)	0.022(19)	-4.56(3)	-3.49	0.023(2)	0.017(3)	-0.21(3)	-3.42
0.875	0.711(5)	0.017(16)	-4.44(4)	-3.47	0.030(2)	0.022(3)	-0.26(3)	-3.36
0.900	0.696(5)	0.022(19)	-4.33(4)	-3.39	0.033(3)	0.025(3)	-0.29(3)	-3.38
0.925	0.678(3)	0.036(10)	-4.20(2)	-3.40	0.041(2)	0.031(3)	-0.35(3)	-3.32
0.950	0.661(10)	0.037(22)	-4.08(6)	-3.35	0.049(5)	0.037(7)	-0.41(4)	-3.30
0.975	0.644(6)	0.049(16)	-3.97(4)	-3.34	0.057(5)	0.042(6)	-0.47(4)	-3.28
1.000	0.622(7)	0.056(13)	-3.81(4)	-3.24	0.073(7)	0.051(12)	-0.59(6)	-3.23
1.025	0.597(8)	0.062(17)	-3.66(5)	-3.25	0.082(6)	0.058(11)	-0.64(6)	-3.23
1.050	0.574(9)	0.071(21)	-3.50(5)	-3.22	0.104(7)	0.069(13)	-0.82(6)	-3.18
1.075	0.540(12)	0.080(27)	-3.31(7)	-3.20	0.112(10)	0.075(19)	-0.86(8)	-3.20

Table 3.2 Vapour-liquid coexistence properties of krypton from molecular simulation using the two-body Barker et al. potential [Bar74].

T^*	r_L^*	P_L^*	E_L^*	m_L^*	r_V^*	P_V^*	E_V^*	m_V^*
0.700	0.800(4)	-0.002(33)	-5.05(3)	-3.58	0.007(2)	0.005(1)	-0.07(3)	-3.55
0.750	0.774(3)	0.001(21)	-4.84(3)	-3.55	0.010(1)	0.007(1)	-0.09(2)	-3.53
0.825	0.735(5)	0.020(19)	-4.53(4)	-3.39	0.024(2)	0.017(2)	-0.21(2)	-3.31
0.850	0.718(4)	0.013(12)	-4.41(3)	-3.35	0.026(2)	0.019(2)	-0.22(3)	-3.34
0.875	0.700(5)	0.020(15)	-4.28(4)	-3.33	0.031(4)	0.023(4)	-0.27(4)	-3.32
0.900	0.687(5)	0.034(12)	-4.18(3)	-3.28	0.041(4)	0.030(4)	-0.36(4)	-3.24
0.925	0.666(7)	0.036(16)	-4.04(4)	-3.26	0.048(7)	0.034(10)	-0.41(7)	-3.23
0.950	0.647(3)	0.044(13)	-3.91(2)	-3.23	0.059(3)	0.041(5)	-0.48(3)	-3.18
0.975	0.624(9)	0.048(18)	-3.76(6)	-3.19	0.067(5)	0.047(7)	-0.54(4)	-3.18
1.000	0.609(6)	0.065(14)	-3.66(3)	-3.16	0.087(4)	0.059(7)	-0.68(5)	-3.12
1.025	0.573(17)	0.073(26)	-3.44(9)	-3.16	0.098(12)	0.065(20)	-0.75(8)	-3.13
1.050	0.548(18)	0.084(31)	-3.28(9)	-3.12	0.131(18)	0.080(33)	-0.98(14)	-3.09
1.065	0.530(23)	0.094(46)	-3.18(12)	-3.11	0.141(16)	0.082(33)	-1.05(11)	-3.08

Table 3.3 Vapour-liquid coexistence properties of xenon from molecular simulation using the two-body Barker et al. potential [Bar74].

T^*	r_L^*	P_L^*	E_L^*	m_L^*	r_V^*	P_V^*	E_V^*	m_V^*
0.700	0.801(5)	-0.010(36)	-5.07(3)	-3.72	0.006(1)	0.004(1)	-0.06(2)	-3.63
0.750	0.777(4)	-0.005(21)	-4.88(3)	-3.43	0.011(2)	0.008(1)	-0.10(2)	-3.49
0.825	0.733(4)	0.005(15)	-4.54(2)	-3.32	0.022(3)	0.016(3)	-0.20(4)	-3.35
0.850	0.715(6)	0.021(20)	-4.41(4)	-3.42	0.027(3)	0.020(3)	-0.24(3)	-3.32
0.875	0.701(3)	0.027(20)	-4.31(2)	-3.37	0.032(3)	0.023(4)	-0.28(3)	-3.30
0.900	0.682(4)	0.026(19)	-4.17(3)	-3.34	0.037(3)	0.027(4)	-0.32(3)	-3.29
0.925	0.664(8)	0.031(16)	-4.05(5)	-3.28	0.047(6)	0.034(7)	-0.39(4)	-3.24
0.950	0.644(9)	0.038(22)	-3.91(6)	-3.25	0.055(3)	0.040(4)	-0.46(3)	-3.22
0.975	0.623(9)	0.045(21)	-3.77(6)	-3.20	0.068(6)	0.048(10)	-0.55(7)	-3.18
1.000	0.605(9)	0.063(23)	-3.65(6)	-3.18	0.082(6)	0.056(10)	-0.65(4)	-3.15
1.025	0.583(11)	0.072(19)	-3.51(7)	-3.15	0.099(9)	0.066(15)	-0.77(6)	-3.12
1.050	0.549(14)	0.083(27)	-3.30(8)	-3.15	0.123(10)	0.077(19)	-0.94(8)	-3.10
1.075	0.501(88)	0.103(183)	-3.02(48)	-3.10	0.160(17)	0.088(34)	-1.18(12)	-3.07

Table 3.4 Vapour-liquid coexistence properties of argon from molecular simulation using the two-body BFW potential [Bar71a] + three-body ($DDD + DDQ + DQQ + DDD4$) intermolecular potentials.

	T^*								
	0.750	0.825	0.850	0.875	0.900	0.925	0.950	0.975	1.00
$\mathbf{r}^*_L$	0.742(5)	0.685(8)	0.671(10)	0.658(10)	0.639(11)	0.613(11)	0.600(10)	0.564(11)	0.513(30)
$P^*_{L,tot}$	0.044(89)	0.017(38)	0.020(50)	0.028(41)	0.033(52)	0.035(41)	0.049(36)	0.045(39)	0.052(100)
$P^*_{L,2body}$	-0.914(77)	-0.854(21)	-0.825(30)	-0.809(21)	-0.788(30)	-0.743(20)	-0.718(17)	-0.673(19)	-0.591(51)
$P^*_{L,DDD}$	0.375(8)	0.271(9)	0.250(10)	0.235(8)	0.218(9)	0.190(9)	0.175(7)	0.149(7)	0.117(15)
$P^*_{L,DDQ}$	0.125(3)	0.090(3)	0.083(3)	0.078(3)	0.072(3)	0.062(3)	0.057(2)	0.049(3)	0.038(5)
$P^*_{L,DQQ}$	0.0254(7)	0.0186(7)	0.0170(7)	0.0159(6)	0.0147(6)	0.0127(7)	0.0117(6)	0.0099(6)	0.0076(11)
$P^*_{L,QQQ}$	0.0023(1)	0.0017(1)	0.0015(1)	0.0014(1)	0.0013(1)	0.0011(1)	0.0010(1)	0.0009(1)	0.0007(1)
$P^*_{L,DDD4}$	-0.124(3)	-0.074(2)	-0.068(2)	-0.063(2)	-0.058(1)	-0.0522(2)	-0.046(1)	-0.040(1)	-0.033(3)
$E^*_{L,tot\,conf.}$	-4.53(3)	-4.13(6)	-4.01(7)	-3.97(5)	-3.89(7)	-3.68(6)	-3.57(6)	-3.39(6)	-3.09(16)
$E^*_{L,2body}$	-4.73(3)	-4.33(6)	-4.16(6)	-4.06(7)	-3.99(6)	-3.83(7)	-3.71(6)	-3.49(6)	-3.19(16)
$E^*_{L,DDD}$	0.169(3)	0.132(3)	0.125(3)	0.119(3)	0.113(3)	0.103(3)	0.097(2)	0.088(3)	0.077(6)
$E^*_{L,DDQ}$	0.046(1)	0.036(1)	0.034(1)	0.032(1)	0.031(1)	0.028(1)	0.026(1)	0.023(1)	0.020(2)
$E^*_{L,DQQ}$	0.0079(2)	0.0063(2)	0.0059(2)	0.0056(1)	0.0053(1)	0.0048(2)	0.0045(1)	0.0040(2)	0.0034(3)
$E^*_{L,QQQ}$	0.00061(2)	0.00049(1)	0.00046(1)	0.00043(1)	0.00041(1)	0.00037(1)	0.00035(1)	0.00031(1)	0.00026(2)
$E^*_{L,DDD4}$	-0.0419(10)	-0.0268(4)	-0.0256(4)	-0.0240(5)	-0.0227(4)	-0.0212(5)	-0.0192(4)	-0.0178(5)	-0.0161(7)
$\mathbf{m}^*_L$	-3.47	-3.48	-3.53	-3.40	-3.35	-3.36	-3.29	-3.26	-3.28
$\mathbf{r}^*_V$	0.0095(17)	0.0174(15)	0.0218(18)	0.0295(37)	0.0350(48)	0.0401(38)	0.0536(56)	0.0605(52)	0.0655(32)
$P^*_{V,tot}$	0.0067(16)	0.0128(17)	0.0162(21)	0.0216(46)	0.0259(64)	0.0301(51)	0.0388(83)	0.0440(83)	0.0490(56)
$P^*_{V,2body}$	-0.0005(4)	-0.0016(4)	-0.0024(5)	-0.0043(13)	-0.0057(20)	-0.0071(15)	-0.0126(28)	-0.0155(31)	-0.0172(23)
$P^*_{V,DDD}\,10^{-3}$	0.0005(22)	0.0212(156)	0.0432(198)	0.0846(533)	0.1350(726)	0.1911(609)	0.442(116)	0.567(145)	0.700(138)
$P^*_{V,DDQ}\,10^{-4}$	0.001(4)	0.070(65)	0.128(66)	0.249(172)	0.406(217)	0.572(188)	1.313(341)	1.67(418)	2.067(428)
$P^*_{V,DQQ}\,10^{-5}$	0.001(6)	0.148(167)	0.239(142)	0.468(364)	0.775(418)	1.092(374)	2.486(636)	3.135(773)	3.896(864)
$P^*_{V,QQQ}\,10^{-6}$	0.0001(4)	0.135(170)	0.198(132)	0.390(336)	0.659(362)	0.931(327)	2.106(532)	2.648(646)	3.307(779)
$P^*_{V,DDD4}\,10^{-4}$	-0.0016(25)	-0.048(28)	-0.111(55)	-0.234(135)	-0.385(220)	-0.530(168)	-1.249(330)	-1.628(408)	-2.015(371)
$E^*_{V,tot\,conf.}$	-0.07(2)	-0.15(3)	-0.20(3)	-0.26(5)	-0.30(5)	-0.34(3)	-0.45(4)	-0.49(5)	-0.52(3)
$E^*_{V,2body}$	-0.07(2)	-0.15(3)	-0.20(3)	-0.26(5)	-0.30(5)	-0.34(3)	-0.46(4)	-0.49(5)	-0.52(3)
$E^*_{V,DDD}\,10^{-3}$	0.02(7)	0.39(28)	0.64(28)	0.87(45)	1.21(49)	1.55(37)	2.65(46)	2.98(55)	3.47(60)
$E^*_{V,DDQ}\,10^{-3}$	0.003(10)	0.11(9)	0.16(8)	0.21(12)	0.30(12)	0.38(9)	0.65(11)	0.72(13)	0.84(16)
$E^*_{V,DQQ}\,10^{-4}$	0.002(12)	0.19(20)	0.25(15)	0.33(23)	0.48(21)	0.62(16)	1.04(17)	1.14(20)	1.34(27)
$E^*_{V,QQQ}\,10^{-5}$	0.001(7)	0.15(18)	0.18(12)	0.24(18)	0.35(16)	0.46(13)	0.76(13)	0.84(15)	0.98(22)
$E^*_{V,DDD4}\,10^{-3}$	-0.004(6)	-0.066(36)	-0.124(59)	-0.182(83)	-0.259(111)	-0.322(75)	-0.563(102)	-0.642(115)	-0.750(119)
$\mathbf{m}^*_V$	-3.57	-3.51	-3.46	-3.36	-3.34	-3.34	-3.25	-3.25	-3.26

Table 3.5 Vapour-liquid coexistence properties of krypton from molecular simulation using the two-body Barker et al. [Bar74] + three-body ($DDD + DDQ + DQQ + DDD4$) intermolecular potentials.

	T^*							
	0.750	0.825	0.850	0.875	0.900	0.925	0.950	0.975
$\mathbf{r}^*_L$	0.712(6)	0.671(9)	0.642(9)	0.631(8)	0.616(7)	0.585(14)	0.528(23)	0.509(23)
$P^*_{L,tot}$	0.051(75)	0.026(45)	0.028(35)	0.036(39)	0.040(26)	0.048(48)	0.045(77)	0.066(71)
$P^*_{L,2body}$	-0.899(46)	-0.848(23)	-0.807(15)	-0.784(21)	-0.758(12)	-0.703(20)	-0.616(40)	-0.573(34)
$P^*_{L,DDD}$	0.390(25)	0.306(12)	0.273(9)	0.255(11)	0.233(7)	0.202(13)	0.157(13)	0.138(12)
$P^*_{L,DDQ}$	0.127(9)	0.098(4)	0.088(3)	0.082(4)	0.074(2)	0.064(4)	0.049(4)	0.043(4)
$P^*_{L,DQQ}$	0.0253(18)	0.0194(9)	0.0172(7)	0.0160(8)	0.0146(5)	0.0125(9)	0.0095(9)	0.0084(8)
$P^*_{L,QQQ}$	0.00222(2)	0.0017(1)	0.0015(1)	0.0014(1)	0.00125(5)	0.0011(1)	0.0008(1)	0.0007(1)
$P^*_{L,DDD4}$	0.00061(4)	0.00050(2)	0.00046(1)	0.00043(2)	0.00041(1)	0.00036(2)	0.00030(2)	0.00028(2)
$P^*_{L,DDD4}$	-0.047(4)	-0.039(1)	-0.037(5)	-0.035(1)	-0.032(1)	-0.030(1)	-0.027(1)	-0.024(1)
$P^*_{L,QQQ}$	-0.135(11)	-0.105(3)	-0.096(2)	-0.087(4)	-0.079(2)	-0.071(3)	-0.056(3)	-0.049(4)
$E^*_{L,tot\ conf.}$	-4.28(3)	-3.98(6)	-3.83(5)	-3.72(5)	-3.59(4)	-3.43(8)	-3.13(10)	-3.00(11)
$E^*_{L,2body}$	-4.49(4)	-4.08(7)	-3.97(5)	-3.88(6)	-3.75(4)	-3.55(8)	-3.23(10)	-3.10(11)
$E^*_{L,DDD}$	0.183(11)	0.152(4)	0.141(3)	0.134(4)	0.126(2)	0.115(5)	0.098(4)	0.090(5)
$E^*_{L,DDQ}$	0.049(3)	0.040(1)	0.037(1)	0.035(1)	0.033(1)	0.030(1)	0.025(1)	0.023(1)
$E^*_{L,DQQ}$	0.00826	0.0067(2)	0.0062(2)	0.0058(2)	0.0055(1)	0.0049(2)	0.0041(2)	0.0038(2)
$E^*_{L,DQQ}$	0.00067(2)	0.00050(2)	0.00046(1)	0.00043(2)	0.00041(1)	0.00036(2)	0.00030(2)	0.00028(2)
$E^*_{L,QQQ}$	0.000061(4)	0.000046(1)	0.000043(2)	0.000043(2)	0.000041(1)	0.000036(2)	0.000030(2)	0.000028(2)
$E^*_{L,DDD4}$	-0.039(1)	-0.037(5)	-0.035(1)	-0.035(1)	-0.032(1)	-0.030(1)	-0.027(1)	-0.024(1)
$\mathbf{m}^*_L$	-3.62	-3.37	-3.38	-3.24	-3.15	-3.24	-3.20	-3.17
$\mathbf{r}^*_v$	0.0105(12)	0.0203(15)	0.0246(20)	0.0348(37)	0.0429(17)	0.0477(31)	0.0578(33)	0.0737(61)
$P^*_{v,tot}$	0.0074(12)	0.0148(18)	0.0183(25)	0.0253(50)	0.0316(25)	0.0350(45)	0.0409(46)	0.0507(104)
$P^*_{v,2body}$	-0.00053(3)	-0.00206	-0.00278	-0.0054(17)	-0.0073(9)	-0.0095(16)	-0.0146(14)	-0.0224(42)
$P^*_{v,DDD}\,10^{-3}$	0.006(6)	0.0374(148)	0.0653(232)	0.171(77)	0.269(44)	0.338(67)	0.652(117)	1.20(29)
$P^*_{v,DDD}\,10^{-4}$	0.018(24)	0.111(42)	0.185(75)	0.497(228)	0.795(142)	0.971(183)	1.86(36)	3.44(85)
$P^*_{v,DDQ}\,10^{-4}$	0.029(53)	0.205(81)	0.327(153)	0.908(423)	1.47(29)	1.74(32)	3.33(69)	6.22(158)
$P^*_{v,DDQ}\,10^{-5}$	0.024(50)	0.168(71)	0.257(131)	0.738(345)	1.21(26)	1.40(25)	2.67(58)	5.05(131)
$P^*_{v,DQQ}\,10^{-6}$	-0.036(24)	-0.127(34)	-0.225(58)	-0.601(255)	-0.978(156)	-1.27(26)	-2.38(40)	-4.40(108)
$P^*_{v,QQQ}\,10^{-6}$	-0.09(2)	-0.18(3)	-0.21(2)	-0.29(4)	-0.36(2)	-0.38(3)	-0.47(3)	-0.58(6)
$P^*_{v,DDD4}\,10^{-4}$	-0.09(2)	-0.18(3)	-0.21(2)	-0.30(4)	-0.36(2)	-0.39(3)	-0.47(3)	-0.58(6)
$E^*_{v,tot\ conf.}$	0.18(17)	0.59(22)	0.86(24)	1.56(55)	2.08(30)	2.31(33)	3.64(46)	5.27(90)
$E^*_{v,2body}$	0.04(5)	0.14(5)	0.20(6)	0.37(14)	0.50(8)	0.54(7)	0.85(12)	1.24(22)
$E^*_{v,DDD}\,10^{-3}$	0.05(10)	0.23(9)	0.30(11)	0.58(23)	0.79(14)	0.82(11)	1.28(20)	1.89(35)
$E^*_{v,DDD}\,10^{-3}$	0.048	0.16(7)	0.20(8)	0.41(16)	0.56(11)	0.57(8)	0.89(15)	1.33(26)
$E^*_{v,DDD4}\,10^{-3}$	-0.082(50)	-0.149(38)	-0.222(48)	-0.411(138)	-0.567(77)	-0.649(94)	-0.996(113)	-1.45(25)
$\mathbf{m}^*_v$	-3.52	-3.40	-3.37	-3.25	-3.20	-3.21	-3.19	-3.13

Table 3.6 Vapour-liquid coexistence properties of xenon from molecular simulation using the two-body Barker et al. [Bar74] + three-body ($DDD + DDQ + DQQ + DDD4$) intermolecular potentials.

	T^*							
	0.750	0.825	0.850	0.875	0.900	0.925	0.950	0.975
$\mathbf{r}^*_L$	0.706(6)	0.671(9)	0.634(12)	0.617(15)	0.599(11)	0.578(13)	0.517(23)	0.511(26)
$P^*_{L,tot}$	0.009(38)	0.024(53)	0.010(46)	0.030(64)	0.031(44)	0.059(61)	0.039(79)	0.060(89)
$P^*_{L,2body}$	-0.947(26)	-0.875(29)	-0.828(20)	-0.779(31)	-0.751(21)	-0.696(34)	-0.611(39)	-0.596(42)
$P^*_{L,DDD}$	0.444(9)	0.364(15)	0.314(14)	0.288(18)	0.260(13)	0.235(14)	0.178(16)	0.169(20)
$P^*_{L,DDQ}$	0.140(3)	0.114(5)	0.0985(5)	0.090(6)	0.081(4)	0.073(5)	0.054(5)	0.0526(6)
$P^*_{L,DQQ}$	0.0268(6)	0.0216(10)	0.0184(9)	0.0168(12)	0.0150(8)	0.0136(9)	0.0100(10)	0.0095(13)
$P^*_{L,QQQ}$	0.0022(1)	0.0018(1)	0.0015(1)	0.0014(1)	0.0012(1)	0.0011(1)	0.0008(1)	0.0008(1)
$P^*_{L,DDD4}$	-0.1915(5)	-0.157(5)	-0.139(4)	-0.128(5)	-0.114(5)	-0.102(5)	-0.082(5)	-0.074(6)
$E^*_{L,tot\,conf.}$	-4.21(4)	-3.96(6)	-3.78(6)	-3.63(8)	-3.52(6)	-3.40(8)	-3.07(10)	-3.02(13)
$E_{L,2body}$	-4.48(4)	-4.10(7)	-3.93(7)	-3.80(9)	-3.64(7)	-3.53(8)	-3.17(11)	-3.13(14)
$E^*_{L,DDD}$	0.209(3)	0.181(5)	0.165(5)	0.155(6)	0.145(5)	0.135(5)	0.114(5)	0.109(7)
$E_{L,DDQ}$	0.054(1)	0.047(1)	0.042(1)	0.040(2)	0.037(1)	0.034(1)	0.028(2)	0.027(2)
$E_{L,DQQ}$	0.0087(2)	0.0075(3)	0.0067(2)	0.0063(3)	0.0058(2)	0.0054(2)	0.0044(3)	0.00434(4)
$E^*_{L,QQQ}$	0.00062(1)	0.00053(2)	0.00047(2)	0.00044(2)	0.00041(2)	0.00038(2)	0.00031(2)	0.00030(3)
$E^*_{L,DDD4}$	-0.067(1)	-0.059(1)	-0.055(1)	-0.052(1)	-0.048(2)	-0.044(2)	-0.039(1)	-0.036(1)
$\mathbf{m}^*_L$	-3.41	-3.28	-3.33	-3.30	-3.22	-3.20	-3.18	-3.15
$\mathbf{r}^*_v$	0.0109(17)	0.0227(27)	0.0245(27)	0.0313(36)	0.0414(45)	0.0513(67)	0.0566(46)	0.0746(33)
$P^*_{v,tot}$	0.0075(16)	0.0163(31)	0.0180(31)	0.0229(43)	0.0301(57)	0.0366(97)	0.0419(66)	0.0514(54)
$P^*_{v,2body}$	-0.0006(3)	-0.0025(8)	-0.0030(8)	-0.0046(11)	-0.0075(15)	-0.0113(34)	-0.0125(21)	-0.0227(20)
$P^*_{v,DDD}\,10^{-3}$	0.0050(75)	0.0686(472)	0.0838(364)	0.148(62)	0.311(116)	0.542(177)	0.717(105)	1.546(217)
$P^*_{v,DDQ}\,10^{-4}$	0.009(24)	0.198(151)	0.233(111)	0.411(175)	0.883(345)	1.518(472)	2.031(296)	4.365(650)
$P^*_{v,DQQ}\,10^{-5}$	0.002(50)	0.357(299)	0.400(216)	0.706(307)	1.559(640)	2.642(798)	3.573(524)	7.67(121)
$P^*_{v,QQQ}\,10^{-6}$	-0.006(41)	0.282(251)	0.302(184)	0.534(241)	1.213(519)	2.039(613)	2.789(412)	5.969(982)
$P^*_{v,DDD4}\,10^{-4}$	-0.0317(242)	-0.299(163)	-0.367(136)	-0.637(291)	-1.416(559)	-2.475(791)	-3.293(514)	-7.17(102)
$E^*_{v,tot\,conf.}$	-0.11(2)	-0.21(3)	-0.21(3)	-0.27(4)	-0.34(5)	-0.42(6)	-0.45(3)	-0.59(3)
$E^*_{v,2body}$	-0.11(2)	-0.21(4)	-0.21(3)	-0.27(4)	-0.35(5)	-0.42(6)	-0.45(3)	-0.60(3)
$E^*_{v,DDD}\,10^{-3}$	0.15(25)	0.94(57)	1.08(45)	1.50(49)	2.39(66)	3.38(73)	4.12(34)	6.67(68)
$E^*_{v,DDQ}\,10^{-3}$	0.02(7)	0.22(15)	0.25(11)	0.34(12)	0.56(17)	0.78(16)	0.95(8)	1.54(17)
$E^*_{v,DQQ}\,10^{-4}$	-0.01(13)	0.34(25)	0.36(19)	0.49(17)	0.83(27)	1.15(23)	1.42(13)	2.29(27)
$E^*_{v,QQQ}\,10^{-5}$	-0.02(9)	0.23(18)	0.24(14)	0.32(12)	0.56(19)	0.77(16)	0.96(9)	1.55(19)
$E^*_{v,DDD4}\,10^{-3}$	-0.078(65)	-0.307(144)	-0.356(120)	-0.479(168)	-0.815(237)	-1.158(234)	-1.415(127)	-2.316(241)
$\mathbf{m}^*_v$	-3.50	-3.34	-3.38	-3.32	-3.23	-3.19	-3.20	-3.13

The coexistence properties obtained from argon using the BFW potential are summarised in Table 3.1 and the BFW + three-body calculations are reported in Table 3.4. In Figure 3.1, experimental data for the vapour-liquid phase envelope of argon are compared with simulation results obtained in this work and data reported by Anta et al. [Ant97] for the Aziz-Slaman [Azi86] and Aziz-Slaman + Axilrod-Teller intermolecular potentials. The comparison with experiment in Figure 3.1 indicates that both the BFW and Aziz-Slaman potentials do not predict the liquid phase coexisting density of argon adequately. There is generally fair agreement for the vapour-branch of the coexistence curve. This contrasts with calculations using the Lennard-Jones potential, which normally yields good agreement with experiment for liquid densities. The good agreement often reported [Sad96b] with the Lennard-Jones potential is fortuitous and probably arises for the "effective" many-body nature of the potential. It is apparent from Figure 3.1 that genuine two-body potentials cannot predict the liquid phase densities of argon adequately. The results obtained from the BFW and Aziz-Slaman potentials are almost identical.

Anta et al. [Ant97] reported that the addition of the Axilrod-Teller term to the Aziz-Slaman potential [Azi86, Azi93] resulted in a considerable improvement in the agreement between theory and experiment as illustrated in Figure 3.1. In Figure 3.1 we also show that the addition of the three-body term to the BFW potential results in good overall agreement of theory with experimental data. The absolute average deviations (AAD) [Sad95] for the vapour and liquid densities are 36.4% and 2.3%, respectively. The lower the value of the AAD, the closer the simulation values are with the experimental data. The experimental liquid branch of the coexisting phase curves is well reproduced by our results. The agreement with the vapour branch is not equally good. It should be noticed from the simulation data, that the three-body contribution to the total

potential energy is less than 0.7% in the vapour side (in the liquid side it is greater than

3%). This means that the inclusion of three body potentials does not significantly affect

the properties of the vapour. That is why we have similar results in the vapour side for

the simulations with only the two-body potential and the simulations with two-body +

three-body potentials. The work of Anta et al. [Ant97, see Figure 3.1] for the Aziz +

AT potentials shows that the calculated vapour branch is shifted closer towards the

experimental curve. However, the AAD is about 10%. Therefore, even if their results

are more accurate, it seems that the inclusion of the three-body potentials is not

sufficient to reproduce the experimental data. We believe that this is due to a lack of

accuracy of the two-body potential for vapour densities. Interestingly, in their work on

argon, Leonhard and Deiters [Leo00] observed behaviour similar to our findings using

the Hloucha ab initio potential [Dei99] + AT potential. Using their own ab initio

potential + AT they found a behaviour similar to Anta et al.

The contributions to both pressure and configurational energy of the various

multipole terms to the three-body interactions of argon are identified in Table 3.4. The

contribution of three-body interactions to the vapour phase is negligible whereas they

make an important contribution to the liquid phase. The various three-body

contributions to the configurational energy of the liquid phase of argon are compared

graphically in Figure 3.2. Although Anta et al. [Ant97] reported values of density,

temperature, pressure and configurational energies, they did not report the contribution

of three-body interactions to either the pressure or energy. It is evident from both the

data in Table 3.4 and the comparison in Figure 3.2 that the triple-dipole term makes the

dominant contribution to three-body interactions. The other third-order multipole

interactions ($u_{DDQ} + u_{DQQ} + u_{QQQ}$) contribute approximately 32% of the triple-dipole

term. However, the effect of this contribution is offset largely by an approximately

equal contribution (26% of the triple-dipole term) from fourth-order triple-dipole interactions of opposite sign. A similar behaviour is seen by the three-body contributions of the pressure. Consequently, the Axilrod-teller term alone is an excellent approximation of three-body dispersion interaction. This conclusion is consistent with earlier work [Dor71] on the relative magnitude of three-body interactions. It is also consistent with other work [Bar72b] on the relative contributions of three-body interactions to the third virial coefficient.

To the best of our knowledge, previous work on the effect of three-body interactions on the phase behaviour of fluids has been confined exclusively to argon. In Tables 3.2, 3.3, 3.5 and 3.6 we report calculations for the vapour-liquid coexistence of krypton and xenon. The coexistence properties calculated from two-body potentials are summarised in Tables 3.2 (krypton) and 3.3 (xenon) whereas calculations including two-body and three-body terms are found in Tables 3.5 (krypton) and 3.6 (xenon). The krypton and xenon atoms are considerably larger than argon and it can be anticipated that their increased polarizability may result in an increase in the relative importance of three-body interactions. The comparison of experiment with theory for the vapour-liquid coexistence of krypton and xenon is illustrated in Figures 3.3 and 3.4, respectively. For both krypton and xenon, the two-body potentials fail to represent the liquid phase densities adequately whereas there is generally fair agreement for the vapour phase. However, it is evident that the addition of three-body interactions results in very good agreement of theory with experiment for sub-critical liquid-phase densities. For krypton, the AAD for the vapour and liquid densities are 34.5% and 1.9% respectively. For xenon, the average absolute deviations for the vapour and liquid densities are 35.8% and 1.4%, respectively. It should be stressed that in all cases the agreement between theory

and experiment represent genuine predictions and no attempt has been made to optimise the agreement by altering the intermolecular potential parameters.

The relative contribution of the various multipole terms (Tables 3.5 and 3.6) to the three-body interactions of krypton and xenon is similar to that observed for argon. Interestingly, for xenon, the magnitude of the contribution from the fourth order triple-dipole term ($DDD4$) is actually slightly greater than the dipole-dipole-quadrupole (DDQ), dipole-quadrupole-quadrupole (DQQ) and triple-quadrupole (QQQ) terms combined. Therefore, for krypton and xenon, the Axilrod-Teller term alone is a good representation of three-body interactions because the contribution of other multipole terms is offset by the contribution from the fourth-order triple dipole term.

In Figure 3.5 we report the logarithm of the total pressure (two-body + three-body) versus the inverse of the temperature, for argon, krypton and xenon. The experimental data [Var75] are also shown. We plot only the vapour pressure because the liquid pressure is characterized by large errors. The simulated pressure is shifted down in comparison with the experimental data. This is simply due to the density shift observed in the vapour branch. In fact, for the vapour the main contribution to pressure comes from the ideal part, $P \approx T \times r$ (see Eq. (2.65)), so an inaccuracy in the density causes an inaccuracy in the pressure.

A significant error relative to the total pressure in the liquid side occurs because the kinetic part and potential part of the pressure are very similar but with opposite sign. For example if we consider in Table 3.4 the value of the temperature $T^* = 0.9$ and the relative liquid density $r^* = 0.639$, the kinetic pressure is $P_{kin}^* = T^* \times r^* \approx 0.575$. The potential part is:

$$P_{L\,pot}^* = P_{L\,2body}^* + P_{L\,DDD}^* + P_{L\,DDQ}^* + P_{L\,DQQ}^* + P_{L\,QQQ}^* + P_{L\,DDD4}^* \approx -0.54 \,.$$

The total pressure is $P_{tot}^* \approx 0.035$ which is just 15% of the two different contributions. Thus a small fluctuation in the values of both kinetic and potential parts can cause a significant fluctuation in the total pressure.

This work has not considered the possibility of interactions from three-body repulsion. Sadus and Prausnitz [Sad96b] used a three-body repulsive potential [She66] in conjunction with Lennard-Jones and AT potentials. They found that three-body repulsion may offset the contribution of Axilrod-Teller interactions by as much as 45%. However, this conclusion is based largely on approximate models [She66] of three-body repulsion that are tied closely the Lennard-Jones potential. It has been suggested [Rit90] that three-body repulsion may improve the prediction of the thermodynamic properties of xenon. Recently, Bukowsky and Szalewicz [Buk01] reported calculations for argon using an *ab initio* potential, which includes three-body repulsion potentials [Lot97b]. They found that the triple-dipole potential alone is an excellent approximation of the total three-body energy because the other contributions cancel. Also our good results obtained for argon, krypton and xenon without including three-body short-range terms may indicate that those potentials do not contribute significantly to the vapour-liquid coexistence. Bukowsky and Szalewicz attribute the cause of the small discrepancies to the neglected quantum effects. Barker et al. [Bar71a] showed that these quantum effects are repulsive and amount to 15-17% of the three-body contributions. They inferred that their inclusion might bring the calculated coexistence curve even closer to the experimental data.
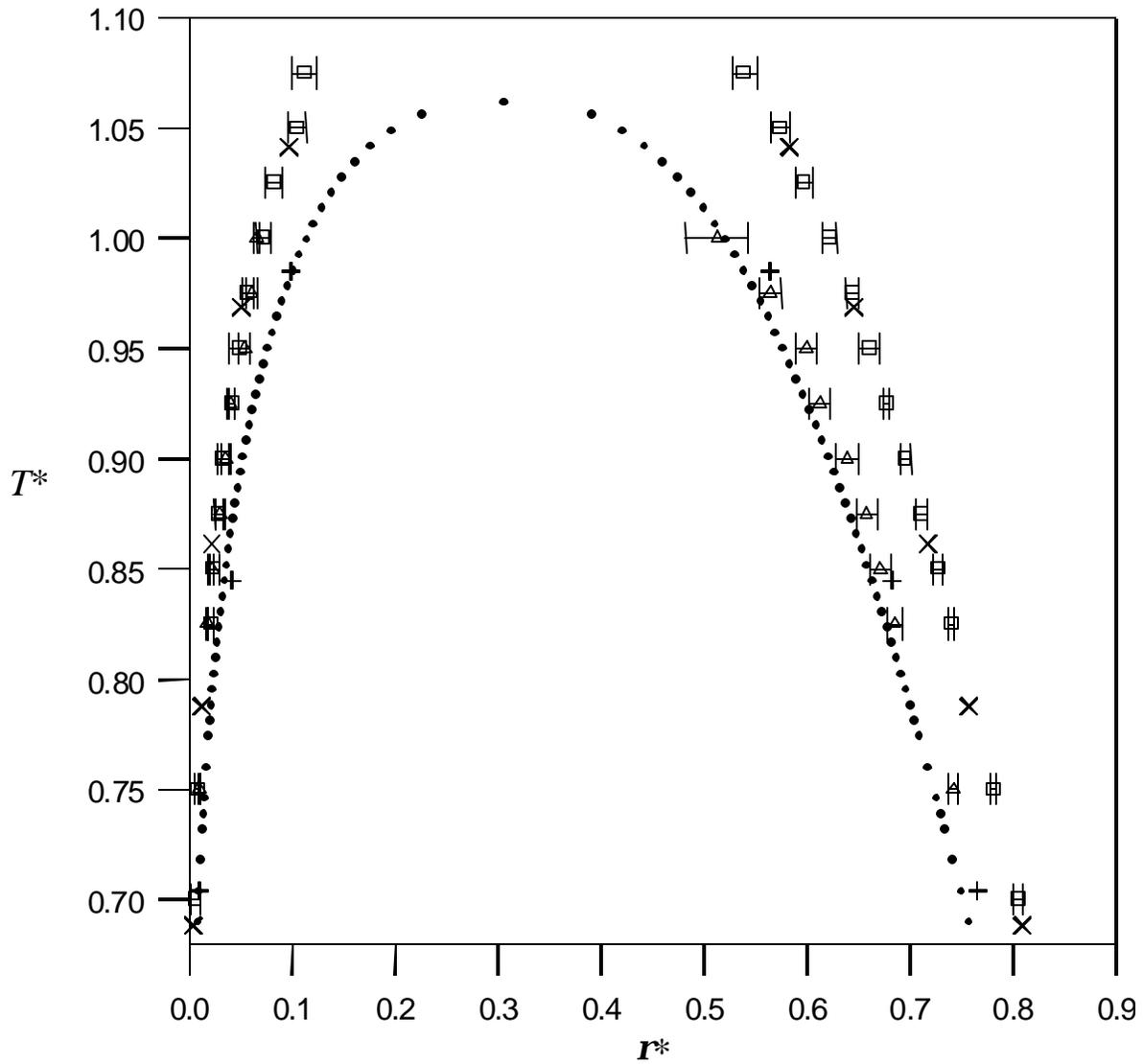
Figure 3.1 Comparison of experiment (•, [Var75]) with calculation using the BFW potential [Bar71a] (□), the Aziz-Slaman potential (✕, [Ant97]), the Aziz-Slaman + Axilrod-Teller (+, [Ant97]) and the BFW + three-body ($DDD + DDQ + DQQ + QQQ + DDD4$) potentials (+) for the vapour-liquid coexistence of argon.
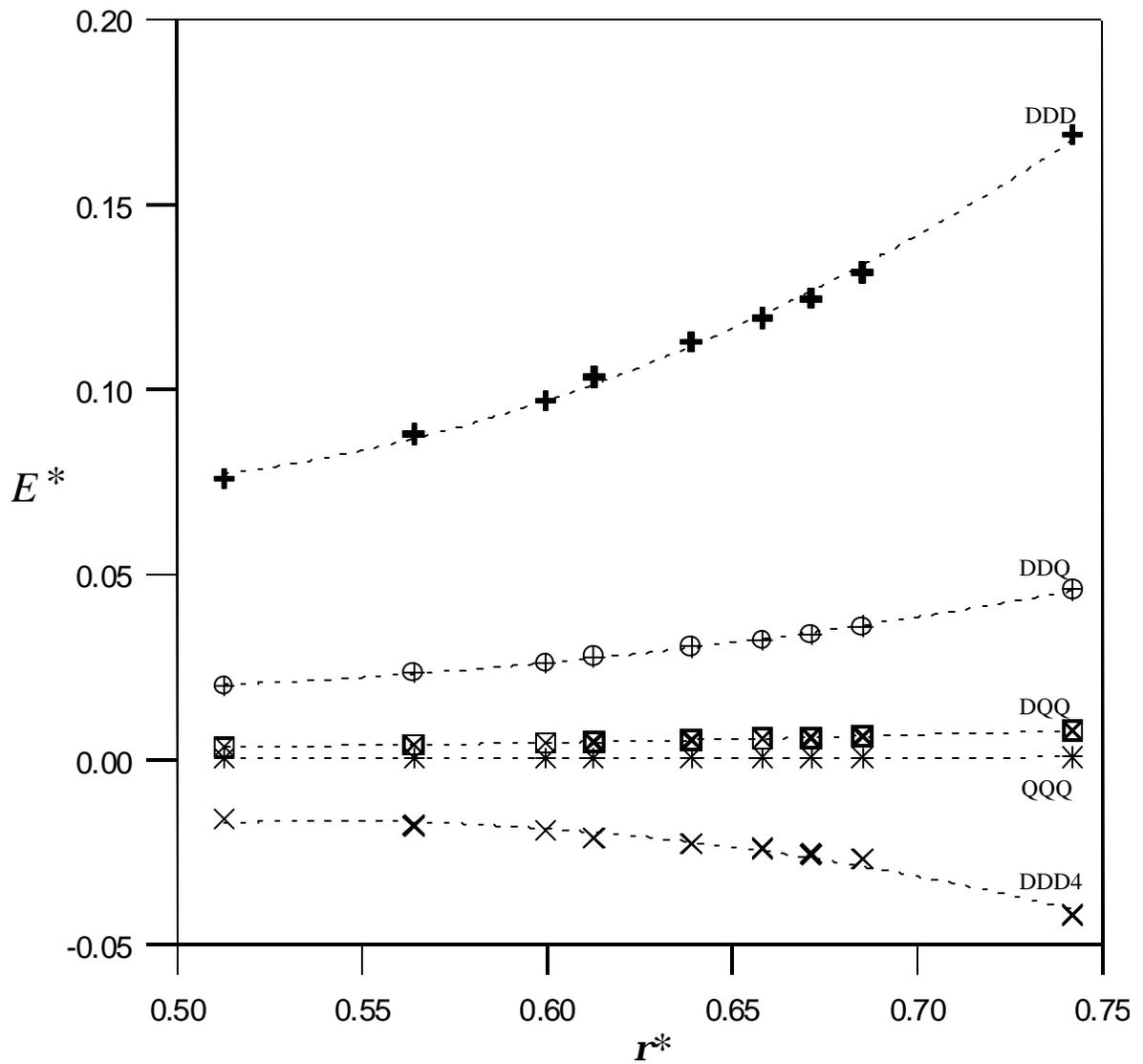
Figure 3.2. Comparison of the contribution of the various three-body terms to the configurational energy of the liquid phase of argon.
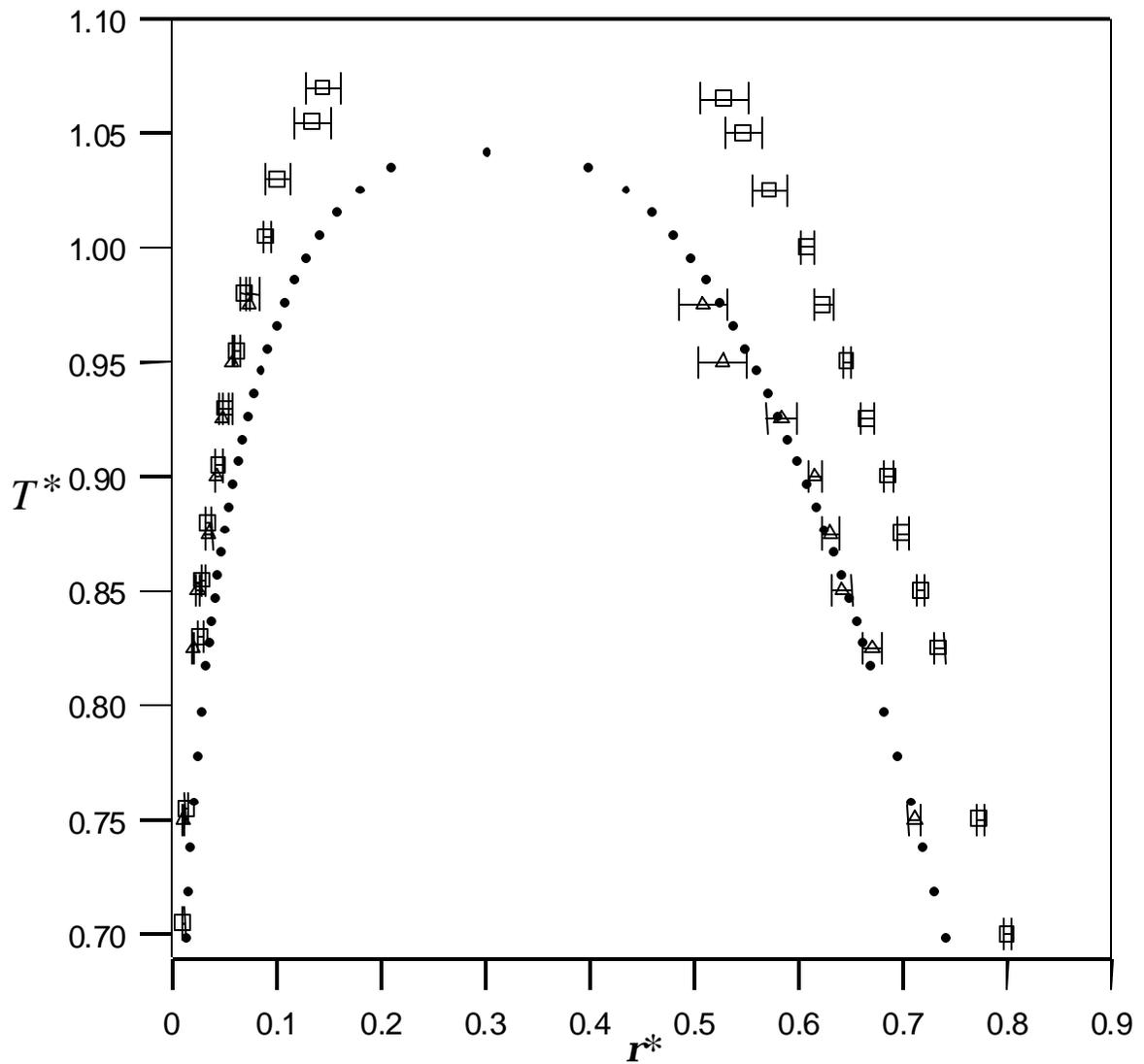
Figure 3.3 Comparison of experiment (•, [Var75]) with calculation using the two-body potential of Barker et al. [Bar74] □) and the Barker et al. [Bar74] + three-body (*DDD* + *DDQ* + *DQQ* + *QQQ* + *DDD*4) potentials (+) for the vapour-liquid coexistence of krypton.
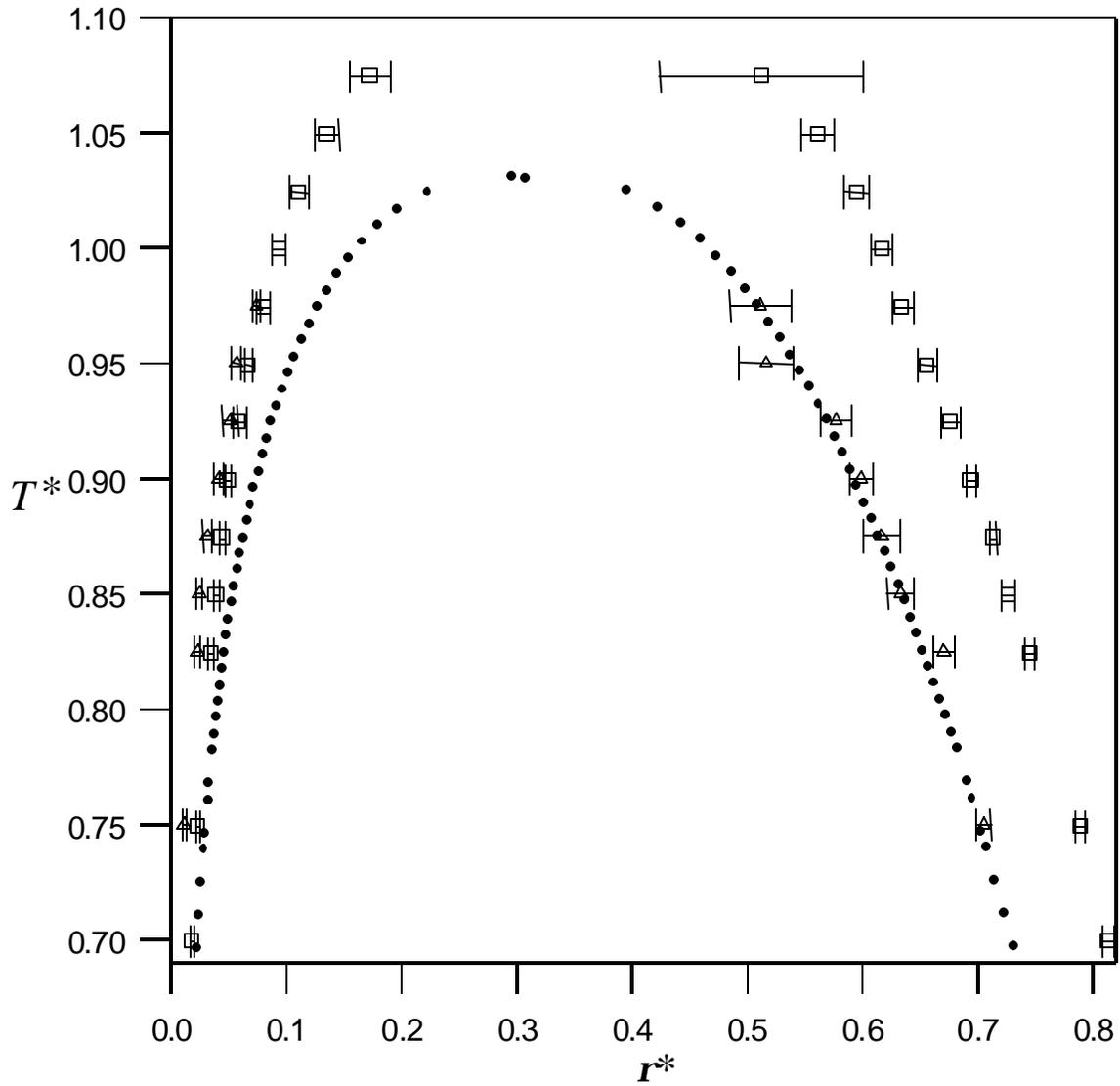
Figure 3.4 Comparison of experiment (•, [Var75]) with calculation using the two-body potential of Barker et al. [Bar74] (□) and the Barker et al. [Bar74] + three-body (*DDD + DDQ + DQQ + QQQ + DDD*4) potentials (+) for the vapour-liquid coexistence of xenon.
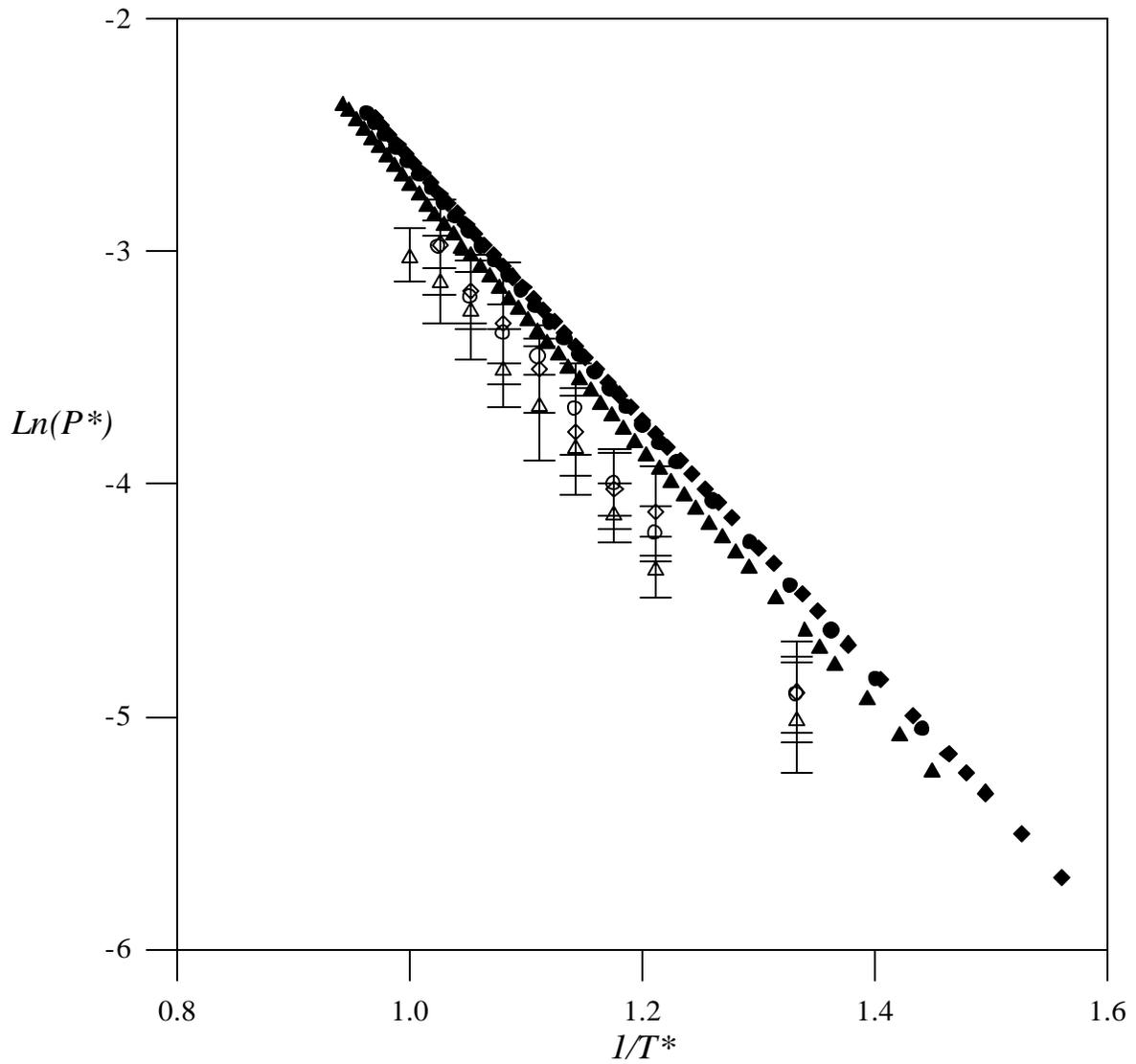
Figure 3.5 Logarithm of the pressure vs. the inverse of the temperature. Comparison between simulation results (Argon + , krypton ○, xenon ◇) and experimental data [Var75] (Argon ▲, krypton ●, xenon ◆)

Argon-krypton mixture

The results of Gibbs ensemble simulations for the vapour-liquid properties of argon + krypton are reported in Tables 3.7 and 3.8. In Tables 3.7 and 3.8, x denotes the mole fraction of the liquid (L) and vapour (V) phases. The motivation for studying the argon + krypton mixture is that it provides a rare example of a binary mixture for which quantitatively accurate intermolecular potentials are available. Therefore, comparison of the results of two-body only simulations with two-body + three-body simulations allows us to make observations concerning the role of three-body interactions. Calculations were performed for both two-body and two-body + three-body terms. The temperature of $T^{*} = 1.148$ (163.15 K) was selected because the vapour-liquid envelope at this temperature is representative of the vapour-liquid phase of the argon + krypton system. Since for pure fluids we found that the two-body + AT potentials represent the dominant terms, we did not include the other multipole three-body terms (see Chapter 2).

A comparison of theory with experiment for the pressure-composition behaviour of argon + krypton is illustrated in Figure 3.6. In general, there is good agreement between theory and experiment [Sch75] for the overall phase envelope. The liquid-phase properties are predicted accurately whereas there are noticeable deviations from experiment for the vapour-phase branch of the coexistence curve. These observations are consistent with the calculations reported for pure component phase equilibria in section 3.1. Interestingly, the results for two-body only and two-body + three-body calculations are almost identical. At a given pressure, three-body interactions do not appear to have a significant role in determining the coexistence composition. This is despite the fact that the data in Table 3.8 indicates that three-body interactions typically contribute approximately 5% of the overall configurational energy.

The pressure-density behaviour of the argon + krypton mixture is illustrated in Figure 3.7. The coexistence density of the vapour-branch is unaffected by three-body interactions. In contrast, Figure 3.7 indicates that three-body interactions can significantly affect the coexisting liquid-phase density. Experimental density data is not available for comparison with the calculations. In section 3.1 we have reported a similar density-shift for the vapour-liquid equilibria of pure noble gases resulting in good agreement with experimental data. The reduction in the liquid-phase density can be attributed to an increase in volume caused by an additional repulsive influence of the three-body term.

Table 3.7 Molecular simulation results for the vapour-liquid equilibria of argon + krypton at $T^* = 1.148$ using the two-body potential.

P^*	x_L^{Kr}	x_V^{Kr}	$P^*_{L\,tot}$	$P^*_{V\,tot}$	r^*_L	r^*_V	$E^*_{L\,2b}$	$E^*_{V\,2b}$	$m^*_{L\,Kr}$	$m^*_{V\,Kr}$	$m^*_{L\,Ar}$	$m^*_{V\,Ar}$
0.0350	0.831(5)	0.544(25)	0.019(40)	0.031(6)	0.618(6)	0.032(3)	-6.00(6)	-0.39(4)	-5.12	-5.08	-5.10	-5.12
0.0445	0.760(11)	0.409(18)	0.066(44)	0.039(7)	0.619(6)	0.042(4)	-5.80(9)	-0.41(5)	-5.04	-5.23	-4.66	-4.62
0.0495	0.680(9)	0.329(38)	0.067(43)	0.048(17)	0.613(8)	0.055(9)	-5.50(8)	-0.51(10)	-5.34	-5.33	-4.48	-4.25
0.0543	0.665(8)	0.323(24)	0.062(40)	0.052(11)	0.620(8)	0.060(7)	-5.52(10)	-0.57(7)	-5.25	-5.28	-4.25	-4.18
0.0642	0.547(7)	0.257(30)	0.064(49)	0.058(15)	0.600(8)	0.067(8)	-5.01(7)	-0.63(12)	-5.62	-5.51	-4.02	-3.99
0.0737	0.475(6)	0.216(18)	0.091(47)	0.067(19)	0.605(9)	0.093(10)	-4.85(9)	-0.82(9)	-5.48	-5.60	-3.88	-3.75
0.0787	0.432(5)	0.177(18)	0.092(55)	0.070(20)	0.596(14)	0.095(10)	-4.66(12)	-0.80(10)	-5.73	-5.80	-3.69	-3.66
0.0837	0.385(4)	0.175(14)	0.106(52)	0.074(39)	0.592(10)	0.103(19)	-4.51(8)	-0.86(17)	-5.73	-5.80	-3.66	-3.63
0.0933	0.319(5)	0.148(12)	0.069(48)	0.082(29)	0.577(6)	0.121(13)	-4.23(3)	-1.00(13)	-5.96	-5.99	-3.58	-3.52
0.0986	0.266(5)	0.138(13)	0.070(55)	0.088(40)	0.573(14)	0.168(16)	-4.08(11)	-1.36(15)	-6.20	-6.14	-3.44	-3.40
0.1041	0.225(6)	0.115(11)	0.113(30)	0.097(36)	0.573(8)	0.165(16)	-3.98(6)	-1.31(14)	-6.36	-6.30	-3.40	-3.36

Table 3.8 Molecular simulation results for the vapour-liquid equilibria of argon + krypton at $T^* = 1.148$ using the two-body + three-body intermolecular potential.

	P^*										
	0.035	0.0445	0.0495	0.0543	0.0642	0.0737	0.0787	0.0837	0.0933	0.0986	0.1041
$x_{L(Kr)}$	0.847(5)	0.738(5)	0.688(15)	0.624(3)	0.556(11)	0.474(6)	0.445(9)	0.389(5)	0.312(4)	0.264(2)	0.221(6)
$x_{V(Kr)}$	0.579(20)	0.429(19)	0.380(23)	0.332(14)	0.292(25)	0.234(19)	0.208(10)	0.184(16)	0.154(9)	0.133(6)	0.119(12)
$P^*_{L tot}$	0.029(85)	0.039(55)	0.048(72)	0.071(62)	0.083(75)	0.086(79)	0.059(81)	0.073(76)	0.069(50)	0.081(86)	0.096(78)
$P^*_{V tot}$	0.033(7)	0.036(7)	0.044(11)	0.047(18)	0.063(24)	0.066(19)	0.063(19)	0.069(19)	0.079(22)	0.080(14)	0.090(19)
P^*_{L2b}	-0.973(47)	-0.918(44)	-0.886(51)	-0.828(30)	-0.812(50)	-0.764(54)	-0.737(40)	-0.713(34)	-0.661(21)	-0.563(45)	-0.574(40)
P^*_{V2b}	-0.008(22)	-0.0085(26)	-0.0131(37)	-0.0144(68)	-0.0267(80)	-0.0353(82)	-0.0245(71)	-0.0367(74)	-0.0446(91)	-0.0479(58)	-0.0668(66)
P^*_{L3b}	0.340(22)	0.304(7)	0.282(11)	0.261(17)	0.246(12)	0.214(11)	0.186(17)	0.177(18)	0.145(12)	0.111(13)	0.115(13)
P^*_{V3b}	0.00024(11)	0.00020(8)	0.00040(15)	0.00039(29)	0.00126(59)	0.00147(49)	0.00108(43)	0.00164(48)	0.00261(83)	0.00279(42)	0.00428(97)
$\mathbf{r}^*_L$	0.577(13)	0.569(4)	0.568(9)	0.556(13)	0.566(11)	0.554(12)	0.532(20)	0.530(21)	0.510(15)	0.464(24)	0.483(23)
$\mathbf{r}^*_V$	0.036(4)	0.038(4)	0.049(6)	0.053(10)	0.077(13)	0.087(9)	0.075(10)	0.090(9)	0.105(11)	0.109(7)	0.133(10)
E^*_{L2b}	-5.65(14)	-5.27(4)	-5.12(11)	-4.85(11)	-4.74(11)	-4.44(11)	-4.21(17)	-4.07(15)	-3.76(11)	-3.37(15)	-3.39(15)
E^*_{V2b}	-0.44(8)	-0.40(4)	-0.49(7)	-0.49(13)	-0.71(13)	-0.75(9)	-0.65(8)	-0.76(7)	-0.88(10)	-0.89(5)	-1.04(8)
E^*_{L3b}	0.196(8)	0.178(3)	0.165(4)	0.156(7)	0.144(5)	0.129(4)	0.116(7)	0.111(7)	0.094(5)	0.079(5)	0.079(5)
E^*_{V3b}	0.0021(8)	0.0017(4)	0.0026(8)	0.0021(11)	0.0051(17)	0.0054(14)	0.0046(11)	0.0058(11)	0.0080(19)	0.0083(9)	0.0105(17)
$\mathbf{m}^*_{L(Kr)}$	-4.9	-5.16	-5.02	-5.31	-5.37	-5.49	-5.62	-5.7	-5.9	-5.98	-6.24
$\mathbf{m}^*_{V(Kr)}$	-4.96	-5.23	-5.21	-5.32	-5.32	-5.49	-5.66	-5.76	-5.9	-6.06	-6.19
$\mathbf{m}^*_{L(Ar)}$	-5.11	-4.63	-4.33	-4.23	-3.9	-3.75	-3.82	-3.67	-3.57	-3.52	-3.41
$\mathbf{m}^*_{V(Ar)}$	-5.15	-4.72	-4.44	-4.29	-3.98	-3.79	-3.83	-3.68	-3.57	-3.51	-3.41
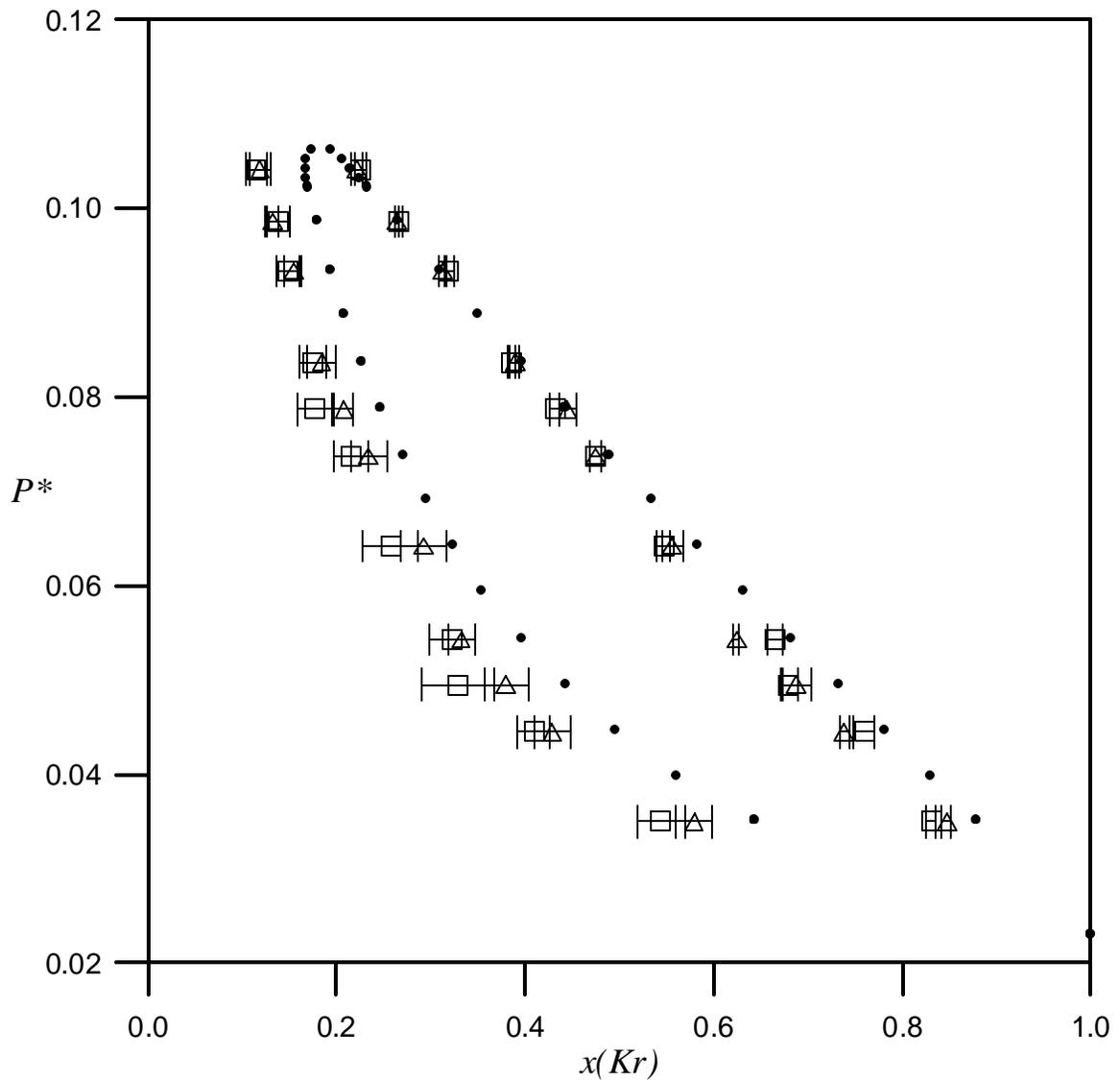
Figure 3.6 Comparison of experimental vapour-liquid equilibria at $T^* = 1.148$ (163.15 K) ($\bullet$, [Sch75]) with calculations using only two-body ($\square$) and two-body + three-body ($\triangle$) intermolecular potentials of argon + krypton.
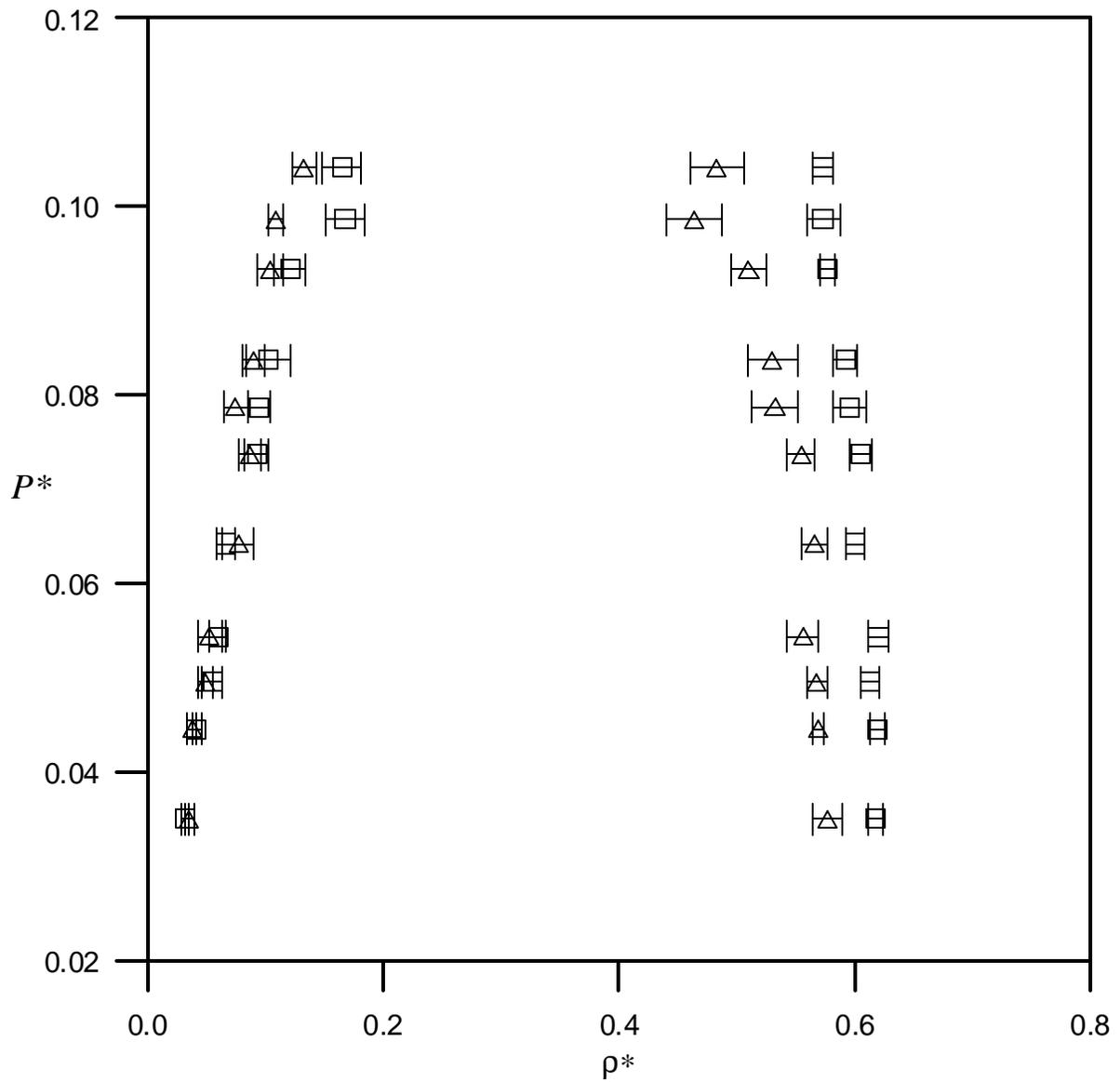
Figure 3.7 Comparison of the effect of two-body only (☐) and two-body + three-body (Δ) interactions on the vapour and liquid coexistence densities and pressures of argon + krypton.

3.2 A simple relationship between two-body and three-body potentials

The introduction of the three-body potential increases the computing time of a normal two-body potential simulation by a factor of ten. This is the main reason to adopt an effective potential that accounts for the three-body effects without incurring expensive routine calculations. Several effective potentials have been proposed [Cop68, Mur71, Miy94, Ste94, van99]. Smit et al. [Smi92] pointed out that a convenient way to account for three- and higher-body interactions consists in using pair potentials that depend on the density. In their work they report the equation of state of a fluid with a particular class of density-dependent potential in terms of the equation of state and energy of a reference fluid.

Analyzing the data from *NVT* Gibbs ensemble simulations shown in previous sections, we noticed that two- and three-body potential energies are linked by a simple relationship. We also performed standard *NVT* Monte Carlo [Sad99] simulations for 500 atoms of argon, krypton and xenon, to check if this relationship holds for different systems. The simulations were performed in cubic boxes, and the conventional periodic boundary conditions were applied [Sad99]. For pair interactions, long-range corrections were used to recover the full contribution to the intermolecular potential (see Appendix 1), whereas three-body interactions were assumed to be zero at separations greater than a quarter of the box length (see Appendix 2). A total of 40000 cycles were used with averages being accumulated after 20000 cycles. The two-body energy (E_2) was obtained by averaging the contribution of the pair potential over all distinct pairs of atoms, whereas the three-body energy (E_3) is the average of the Axilrod-Teller potential for all distinct triplets of atoms.

The ratio of three-body (E_3) to two-body (E_2) energies obtained from *NVT* Gibbs ensemble simulations is shown in Figure 3.8 as a function of reduced number density, r^*. Also results from *NVT* Monte Carlo simulations, reported in Table 3.9, are shown in Figure 3.8 to supplement Gibbs ensemble data. The temperatures used covered the temperature range for vapour-liquid coexistence of a pure fluid.

Table 3.9 *NVT* Monte Carlo simulation results for argon, krypton and xenon at different densities and temperatures.

	r^*	T^*	E_{AT}^*	E_{2b}^*	P_{AT}^*	P_{2b}^*
Ar	0.350	1.30	0.031(1)	-1.97(2)	0.033(1)	-0.24(5)
	0.400	1.20	0.044(2)	-2.35(2)	0.053(2)	-0.33(7)
Kr	0.450	1.25	0.068(2)	-2.63(4)	0.091(2)	-0.36(9)
	0.475	1.00	0.074(1)	-2.82(1)	0.106(2)	-0.59(5)
Xe	0.375	1.20	0.058(2)	-2.17(2)	0.065(2)	-0.29(5)
	0.425	1.00	0.075(2)	-2.54(2)	0.095(3)	-0.49(4)

It is apparent that the ratio is a linear function of density which is consistent with theoretical considerations [Ste94, Mur71]. Furthermore, within the statistical uncertainties of the simulation, the results for argon, krypton and xenon appear to obey the same relationship. A least-squares fit of the simulation data for argon, krypton and xenon yields the following empirical relationship between two-body and three-body energies:

$$E_3 = -\frac{2nrE_2}{3es^6} \tag{3.3}$$

As E_2 is generally negative, E_3 is positive which is consistent with simulation data. The above equation is a remarkably simple result that fits all the simulation data with an average absolute deviation of 2.0 %. The only constants in Eq. (3.3) are the triple-dipole

coefficient n, and the pair potential parameters e and s. The relationship is independent of temperature for the range of densities at which the fluid is normally a liquid.

The benefit of Eq. (3.3) is that an accurate estimate of the three-body energy contribution for fluid densities can be obtained from two-body calculations alone. To test the accuracy of this relationship, we performed Gibbs ensemble simulations for the phase equlibria of argon with the energies calculated from the BFW potential plus the contribution from Eq. (3.3). The Gibbs ensemble calculations were performed by first determining the contribution of two-body interactions. The two-body contribution was used in Eq. (3.3) to determine the contribution of three-body interactions. The combined two-body and three-body energies were then used to determine the acceptance of the Monte Carlo move. The results of these calculations are compared in Figure 3.9 with both experimental data [Var75] and the full two-body + three-body calculation reported in section 3.1 [Mar99]. The comparison indicates that the results obtained using Eq. (3.3) are nearly identical to the full two-body + three-body calculations.

It should be noted that, strictly speaking, the validity of the relationship is tied to the pair and three-body potentials used in the simulations, and only three different atomic species were considered. However, if these potentials genuinely reflect the contribution of two-body and three-body interactions, the result could be valid generally. We emphasise that the relationship should not be used for effective potentials such as the Lennard-Jones potential. The accuracy of the single relationship for argon, krypton and xenon may also indicate that the result is valid for other atoms.
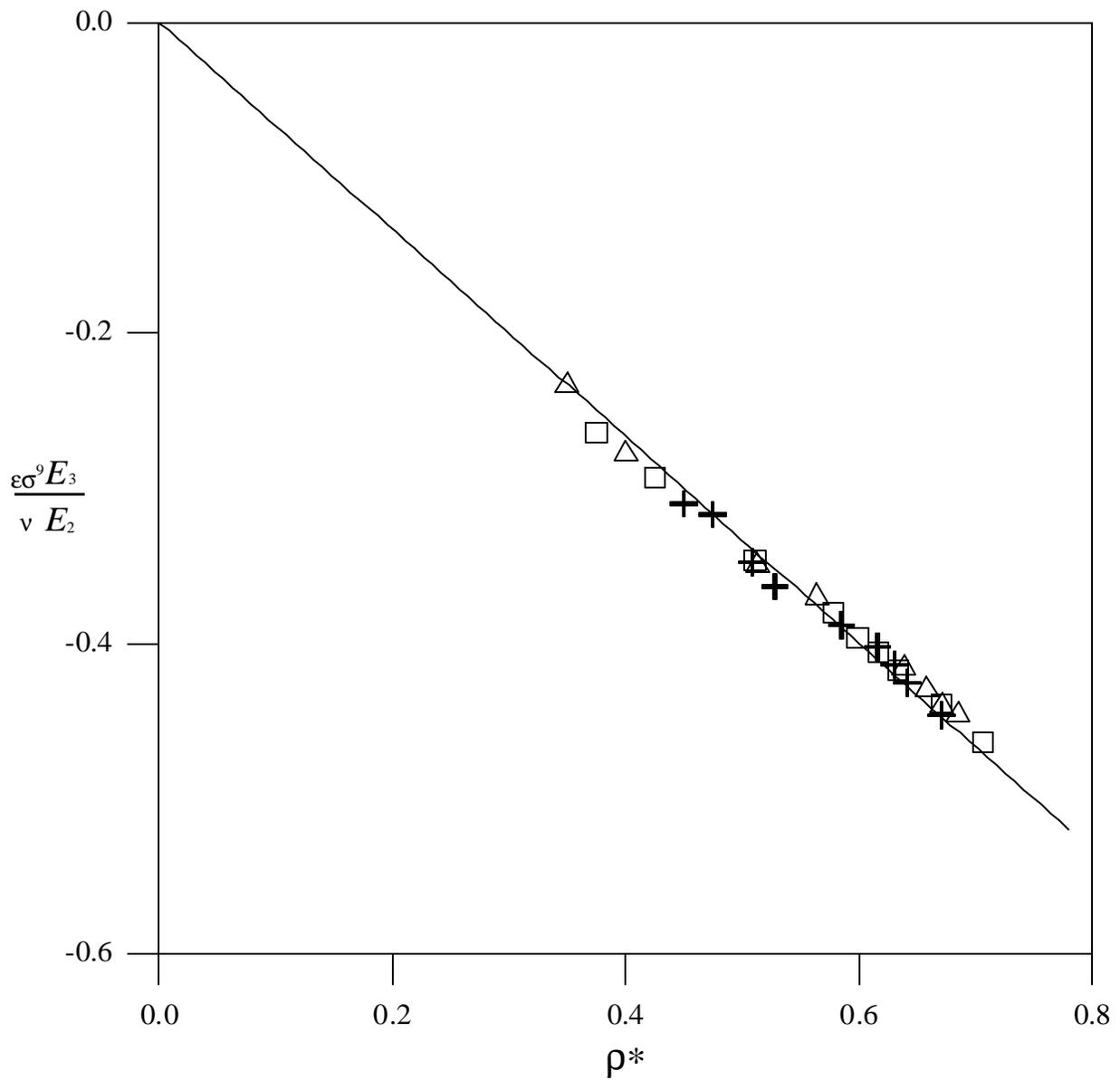
Figure 3.8 The ratio of three-body and two-body energies obtained from molecular simulation at different reduced densities. Results are shown for argon (Δ), krypton ($+$) and xenon ($\square$). The line through the points was obtained from Eq. (3.3).
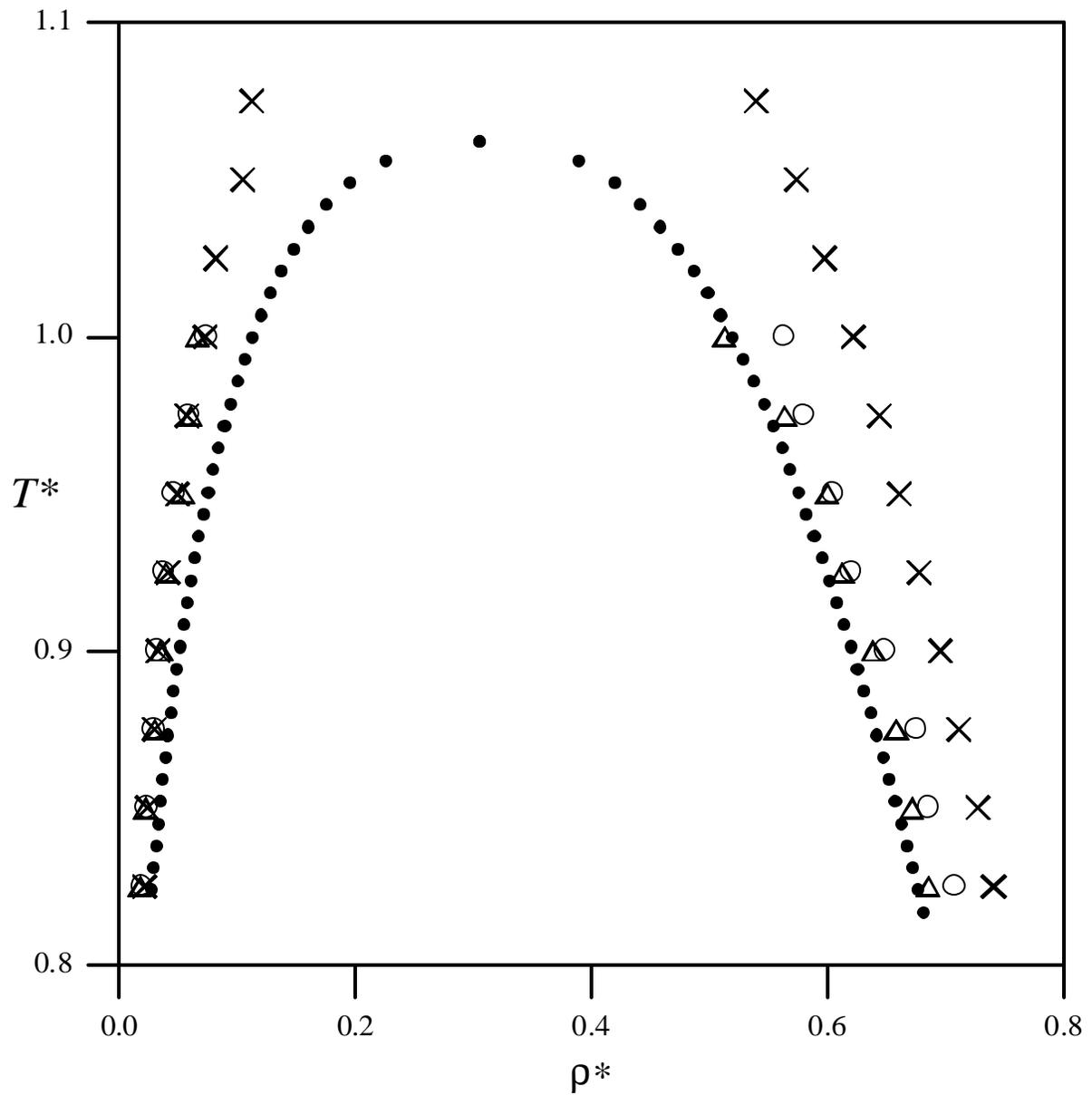
Figure 3.9 Comparison of *NVT* Gibbs ensemble calculations with experiment (●) [Var75] for the vapour-liquid equilibria of argon in the reduced temperature-density projection. Results are shown for the BFW potential (×), the BFW + Axilrod-Teller potential (Δ) and the BFW + three-body contribution from Eq. (3.3) potential (○).

Chapter 4

Shear Rate Dependence of Pressure, Energy and Viscosity in Planar Couette Flow

In this chapter, NEMD simulations of the shear viscosity of argon and xenon are presented. In the simulations with argon, the atoms interact via the Barker-Fisher-Watts (BFW) [Bar71a] and Axilrod-Teller (AT) [Axi43] intermolecular potentials (see Chapter 2). In the simulations with xenon, the atoms interact via the potential devised by Barker et al. [Bar74] and Axilrod-Teller (AT) [Axi43] potentials (see Chapter 2). An adequate system size of 500 atoms was used, resulting in greater statistical accuracy than reported elsewhere [Lee93, Lee94]. We show that the pressure is clearly not a linear function of $\dot{g}^{3/2}$, but can be described by an analytic $\dot{g}^2$ dependence. This relationship is independent of the three-body potential interaction and is only a consequence of two-body interactions. Our results also demonstrate that the shear viscosity is not necessarily a linear function of $\dot{g}^{1/2}$. The statistical accuracy of the viscosity data is however not sufficient to unambiguously determine an accurate dependence on the strain rate. In section 4.1 we give the details of the simulations performed and report the results in section 4.2. In section 4.3 we analyze for the non-equilibrium case the ratio between the three-body energy and two-body energy as done in section 3.2.

4.1 Simulation details

NEMD Algorithm

The NEMD simulations were performed by applying the standard SLLOD equations of motion for planar Couette flow (see Chapter 2). The SLLOD equations for a one-component atomic fluid flowing with streaming velocity v_x in the x-direction and constant strain rate $\dot{\boldsymbol{g}} = \dfrac{dv_x}{dy}$ were applied (see Eq. 2.72 and Eq. 2.77). The equations of motion were integrated by a 4th order Gear predictor-corrector scheme (see Chapter 2), with a reduced integration time step ($t^* = t\sqrt{\boldsymbol{e}/m\boldsymbol{s}^2}$) of 0.001. A non-equilibrium simulation trajectory is typically run for 250000 time steps. To equilibrate the system, each trajectory is first run without a shearing field. After the shearing field is switched on, the first 50000 time steps of each trajectory are ignored, and the fluid is allowed to relax to a non-equilibrium steady-state. In the simulations with argon atoms averages were taken over 5 independent trajectories, each starting at a new configuration. Thus, every pressure, energy and viscosity data point represents a total run length of $5 \times 200000 = 10^6$ time steps. In the simulations with xenon, averages are taken over 2 independent trajectories, resulting in the same statistical accuracy.

Intermolecular potentials

The total intermolecular potential adopted consists in contributions from two-body interactions (u_{2b}) and three-body dispersion interactions (u_{3b}). As previously mentioned, for argon we used BFW + AT potentials and for xenon Barker et al. [Bar74] + AT potentials. The two-body potentials were truncated at half the box length and appropriate long-range correction terms were evaluated to recover the contribution to

the pressure and energy for the full intermolecular potential (see Appendix 1). The three-body potentials were truncated at a quarter of the box length (see Appendix 2) and the long-range correction terms for energy and pressure were evaluated as:

$$E_{3b}^{Long-range} = N\mathbf{r}^2 \iint_{\substack{r_{12}<r_{13}<r_{23} \\ r_{23}>r_{3b}^{cut-off}}} g^{(3)}(r_{12},r_{13},r_{23})u_{3b}(r_{12},r_{13},r_{23})dr_{12}dr_{13} \qquad (4.1)$$

where $g^{(3)}(r_{12},r_{13},r_{23})$ is the 3rd order radial distribution function written as:

$$g^{(3)}(r_{12},r_{13},r_{23}) = g^{(2)}(r_{12})g^{(2)}(r_{13})g^{(2)}(r_{23}) \qquad (4.2)$$

using the superposition approximation [Bar71a] and setting $g^{(2)}(r_{23})$ to unity.

The long-range correction for the three-body pressure was calculated as:

$$P_{3b}^{Long-range} = \frac{3E_{3b}^{Long-range}}{V} \qquad (4.3)$$

where we used the fact that the Axilord-Teller potential is a homogeneous function [Bar71a, see also Appendix 2].

Before applying the SLLOD algorithm using these intermolecular potentials, we repeated simulations on a Lennard-Jones (LJ) fluid at the LJ triple point ($T^* = 0.722$, $\mathbf{r}^* = 0.8442$, where the superscript * stands for reduced units), reported by Evans et al. [Eva89]. Our simulations were in excellent agreement with these results, and are displayed in Figures 4.1, 4.2 and 4.3. The pressures and energies were found to vary linearly with $\dot{\mathbf{g}}^{3/2}$, whereas the viscosity varied as $\dot{\mathbf{g}}^{1/2}$, as previously observed. We further note that all subsequent simulations performed on the BFW + AT and BWLSL + AT fluids are made with *exactly* the same computer program. The only difference is the form of the intermolecular potentials, and hence forces, used in the calculation of fluid properties. This limits any possible errors that could be introduced by comparing results generated from different code.
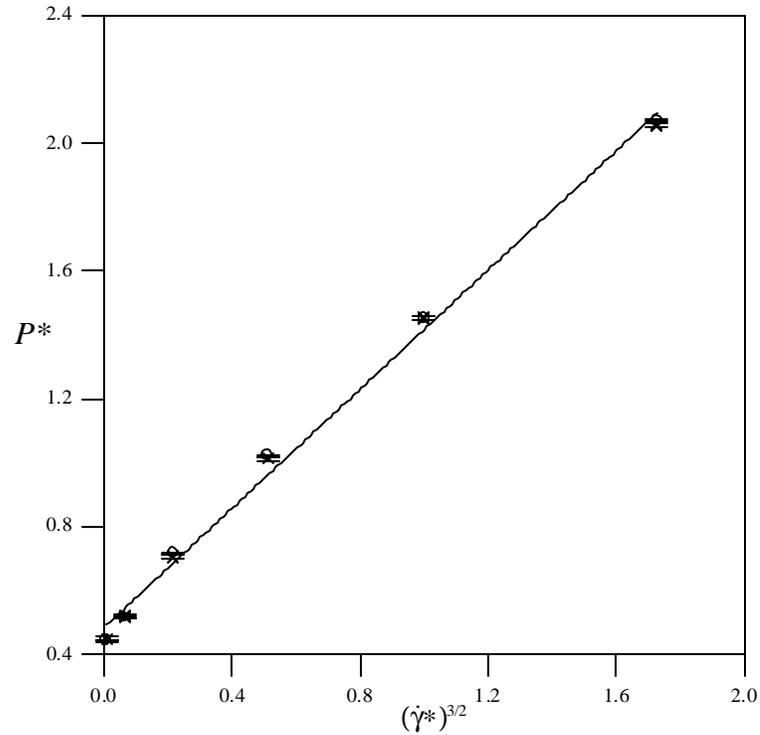
Figure 4.1 Comparison of Evans et al. [Eva89] pressure (○) with our own (✕) for a system of 2048 Lennard-Jones atoms and a cut-off =3.5 (reduced units).
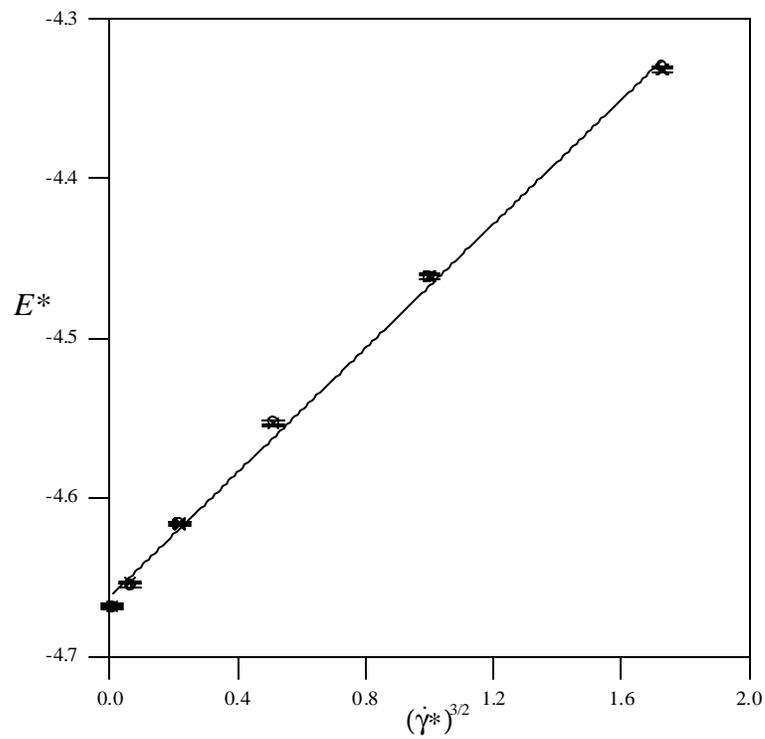
Figure 4.2 Comparison of Evans et al. [Eva89] configurational energy (○) with our own (✕) for a system of 2048 Lennard-Jones atoms and a cut-off =3.5 (reduced units).
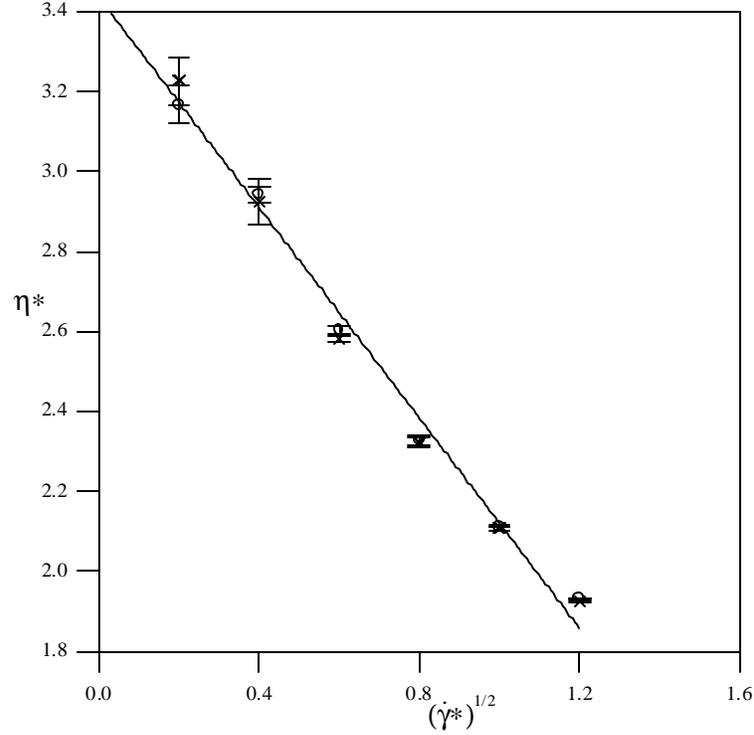
Figure 4.3 Comparison of Evans et al. [Eva89] viscosity ($\bigcirc$) with our own ($\times$) for a system of 2048 Lennard-Jones atoms and a cut-off $=3.5$ (reduced units).

4.2 Results

The results of the NEMD simulations for the pressure, energy and shear viscosity of argon at different strain rates are reported in Table 4.1. Results for xenon are reported in Table 4.2. The normal convention was adopted for the reduced density ($r^* = r s^3$), temperature ($T^* = kT/e$), energy ($E^* = E/e$), pressure ($P^* = P s^3 /e$), viscosity ($h^* = h s^2 (me)^{-1/2}$) and strain rate ($\dot{g}^* = \dot{g}[s (m/e)^{1/2}]$). All simulations for argon were performed at the state point (r^*, T^*) = (0.592 [1.034 gcm^{-3}], 0.95 [135 K]); for xenon at the state point (r^*, T^*) = (0.6 [2.222 gcm^{-3}], 0.9 [252.9 K]). These points were chosen because they are representative of the liquid phase being approximately mid-way between the triple point and the critical point (for both argon and xenon). The

number of atoms in our systems was $N = 500$, and the size of our simulation cell, L, was 9.453 (reduced units) for argon and 9.410 (reduced units) for xenon. The three-body terms were truncated at $0.25L$, whereas the two-body terms were truncated at $0.5L$. These cut-off distances further ensured that the total non-equilibrium pair distribution function was constant (i.e., equal to unity) over the range of r where long-range corrections are applied.

Table 4.1 Pressure, energy and shear viscosity at different strain rates for argon.

$\dot{g}^*$	2-body potential without 3-body potential			2-body potential with 3-body potential		
	P^*	$E^*_{conf.}$	h^*	P^*	$E^*_{conf.}$	h^*
0.0	-0.103(2)	-3.682(2)		0.017(2)	-3.557(1)	
0.078	-0.105(1)	-3.683(1)	0.72(2)	0.019(2)	-3.555(1)	0.72(3)
0.1755	-0.108(1)	-3.679(1)	0.754(5)	0.020(2)	-3.554(1)	0.742(6)
0.24	-0.102(2)	-3.683(2)	0.747(6)	0.022(1)	-3.552(1)	0.732(6)
0.312	-0.103(2)	-3.677(1)	0.753(2)	0.024(2)	-3.551(1)	0.733(5)
0.4	-0.099(1)	-3.673(1)	0.747(1)	0.031(2)	-3.550(1)	0.725(1)
0.5	-0.092(4)	-3.667(3)	0.746(6)	0.034(3)	-3.541(1)	0.725(6)
0.702	-0.079(2)	-3.656(1)	0.727(2)	0.054(1)	-3.529(1)	0.719(1)
0.9555	-0.050(1)	-3.631(2)	0.715(1)	0.084(2)	-3.511(1)	0.703(2)
1.248	0.002(1)	-3.595(1)	0.699(1)	0.135(1)	-3.480(1)	0.689(1)
1.5795	0.076(1)	-3.558(1)	0.677(1)	0.214(1)	-3.443(1)	0.668(1)
1.95	0.179(2)	-3.506(1)	0.653(1)	0.312(2)	-3.396(1)	0.644(1)

Table 4.2 Pressure, energy and shear viscosity at different strain rates for xenon.

$\dot{g}^*$	2-body potential without 3-body potential			2-body potential with 3-body potential		
	P^*	$E^*_{conf.}$	h^*	P^*	$E^*_{conf.}$	h^*
0.0	-0.161(1)	-3.696(1)		0.012(4)	-3.512(2)	
0.2	-0.156(6)	-3.672(4)	0.77(1)	0.0150(1)	-3.509(1)	0.76(1)
0.4	-0.152(5)	-3.688(2)	0.772(3)	0.0243(9)	-3.5022(4)	0.765(2)
0.6	-0.138(2)	-3.683(5)	0.758(4)	0.0387(2)	-3.4938(1)	0.749(1)
0.8	-0.1187(8)	-3.660(1)	0.753(4)	0.065(1)	-3.4795(6)	0.739(1)
1	-0.088(6)	-3.6354(7)	0.7438(7)	0.092(2)	-3.4628(8)	0.7263(8)
1.2	-0.0527(1)	-3.611(2)	0.733(2)	0.132(3)	-3.443(3)	0.716(2)
1.4	-0.0073(9)	-3.5875(5)	0.717(1)	0.184(4)	-3.4211(1)	0.706(1)
1.6	0.046(3)	-3.5577(4)	0.7021(3)	0.237(1)	-3.395(1)	0.6892(7)
1.8	0.1073(6)	-3.5304(6)	0.6882(9)	0.298(1)	-3.3689(3)	0.6789(8)

The uncertainties in the time averages for the energy, pressure and viscosity, reported in Tables 4.1 and 4.2, represent the standard errors of the averages over 5 independent non-equilibrium trajectories for argon and over 2 independent non-equilibrium trajectories for xenon. The data include calculations with the two-body potential alone and a combined two-body + AT potential. We confirmed that the two and three-body energies and pressures at equilibrium were correct by comparing them with independent calculations of these quantities obtained by Monte Carlo simulations [All87].

These results, and various attempts to fit the simulation data, are illustrated in Figures 4.4 - 4.10. In Tables 4.3 and 4.4 the coefficients of the fits are presented, as well as their respective errors. Additionally, the coefficients of both fitted equations and the absolute average deviations (AAD) [Sad95] are given. The AAD is a measure of the overall accuracy of the agreement between the fits and the simulation data and is defined as:

$$\text{AAD}(\%) = 100 \times \sum_{i=1}^{s} \frac{1}{s} \left| \frac{f^{simul.}(\dot{\boldsymbol{g}}_i) - f^{fit}(\dot{\boldsymbol{g}}_i)}{f^{simul.}(\dot{\boldsymbol{g}}_i)} \right| \qquad (4.4)$$

where s is the number of data points, $f^{simul.}(\dot{\boldsymbol{g}}_i)$ is the simulation value of the quantity considered (pressure, energy or viscosity) as a function of $\dot{\boldsymbol{g}}_i$ and $f^{fit}(\dot{\boldsymbol{g}}_i)$ is the value taken from the fitting curve.

Table 4.3 Coefficients of the fits and relative errors for argon.

	a^*	b^*	AAD %
$P = a + b\dot{g}^{3/2}$	0.0032(6)	0.1039(5)	26.72
$P = a + b\dot{g}^2$	0.0164(6)	0.0781(4)	3.97
$E = a + b\dot{g}^{3/2}$	-3.5607(4)	0.0592(3)	0.08
$E = a + b\dot{g}^2$	-3.5554(4)	0.0430(2)	0.09
$h = a + b\dot{g}^{1/2}$	0.800(2)	-0.105(2)	1.60
$h = a + b\dot{g}$	0.752(1)	-0.0535(8)	0.74
$h = a + b\dot{g}^{3/2}$	0.7360(8)	-0.0339(5)	0.45
$h = a + b\dot{g}^2$	0.7279(7)	-0.0229(3)	0.69

Table 4.4 Coefficients of the fits and relative errors for xenon.

	a^*	b^*	AAD %
$P = a + b\dot{g}^{3/2}$	0.0027(1)	0.1054(3)	16.04
$P = a + b\dot{g}^2$	0.0108(1)	0.0868(3)	3.49
$E = a + b\dot{g}^{3/2}$	-3.5224(1)	0.0616(1)	0.08
$E = a + b\dot{g}^2$	-3.5094(1)	0.0447(1)	0.04
$h = a + b\dot{g}^{1/2}$	0.849(2)	-0.125(2)	0.86
$h = a + b\dot{g}$	0.7863(2)	-0.0598(8)	0.38
$h = a + b\dot{g}^{3/2}$	0.7654(8)	-0.0367(5)	0.31
$h = a + b\dot{g}^2$	0.7549(7)	-0.0247(3)	0.57

Mode-coupling theory [Kaw73] predicts that the pressure of a fluid under shear has a linear dependence with $\dot{g}^{3/2}$. To test this prediction, we plot the total pressure of the fluid against $\dot{g}^{3/2}$ in Figure 4.4(a) for argon and in Figure 4.5(a) for xenon. If the pressure were a linear function of $\dot{g}^{3/2}$ one would expect random statistical fluctuations in the data points about the linear fit. However, a careful analysis of the data suggests a systematic deviation from the expected $\dot{g}^{3/2}$ linear behaviour.

In Figure 4.4(b) for argon and in Figure 4.5(b) for xenon the total pressure is presented as a function of $\dot{g}^2$. We find that the pressure is more closely represented by an analytic $\dot{g}^2$ dependence.
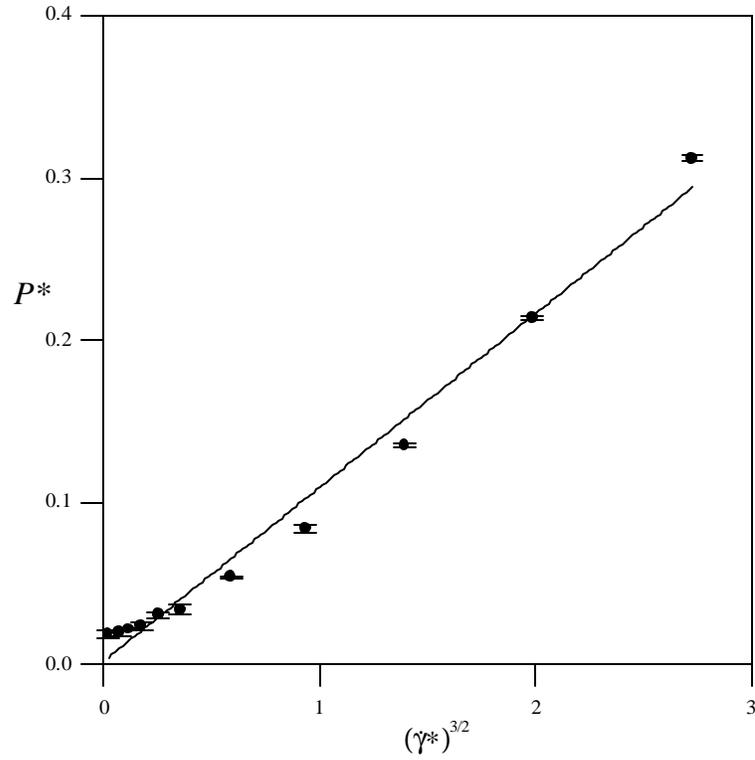
Figure 4.4a Total pressure of argon as function of $\dot{g}^{3/2}$ using 2-body + 3-body potentials.
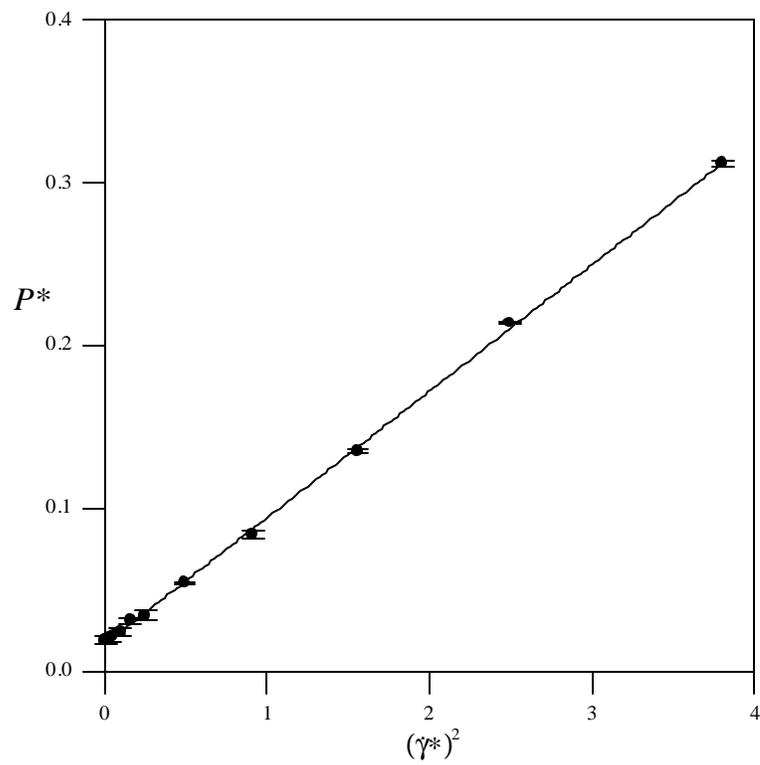
Figure 4.4b Total pressure of argon as function of $\dot{g}^2$ using 2-body + 3-body potentials.
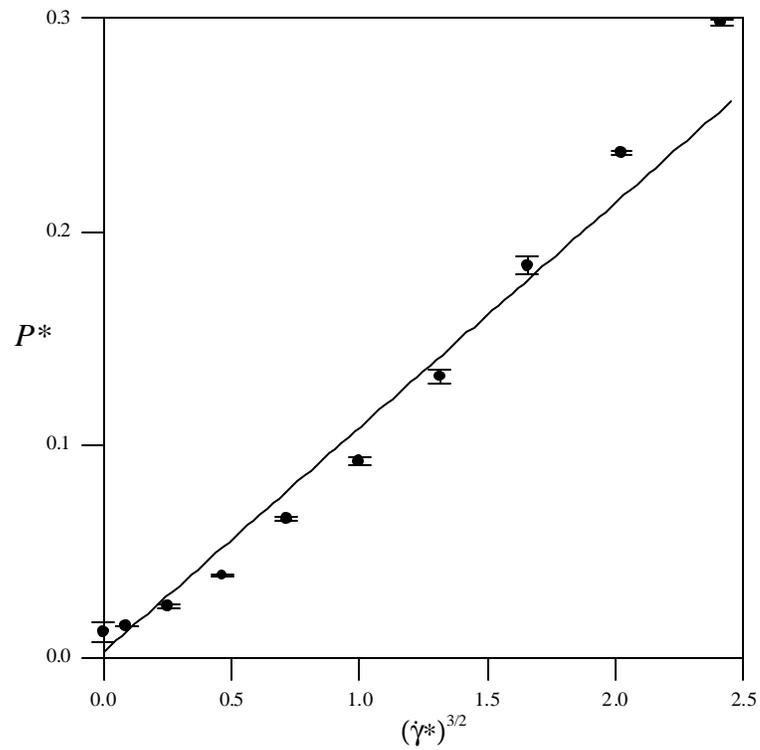
Figure 4.5a Total pressure of xenon as function of $\dot{g}^{3/2}$ using 2-body + 3-body potentials.
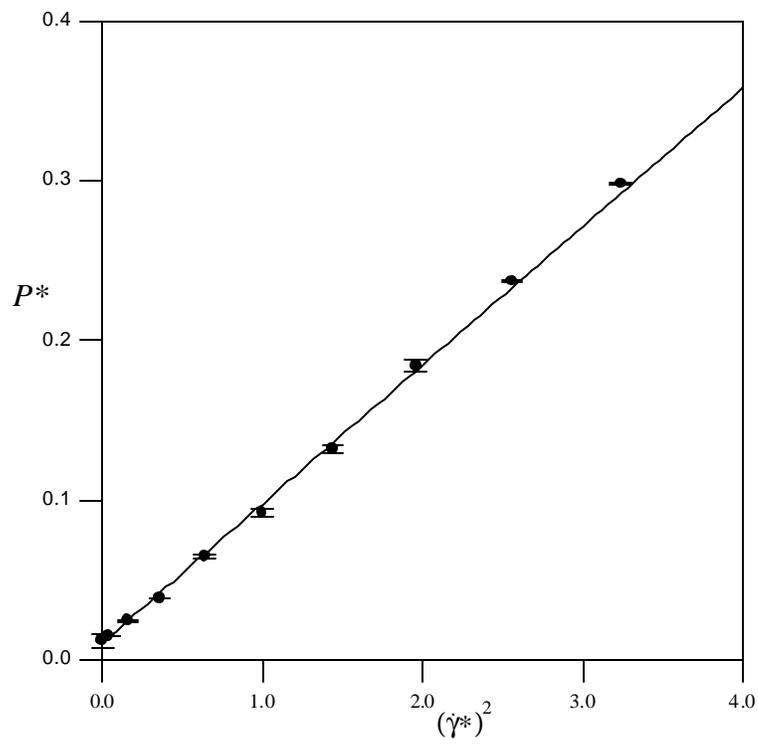
Figure 4.5b Total pressure of xenon as function of $\dot{g}^{2}$ using 2-body + 3-body potentials.

For argon at equilibrium, a pressure of approximately 1 MPa is predicted compared with an experimental value of 4 MPa [Var75]. The main contribution to the overall pressure comes from the kinetic component and two-body interactions which are of similar magnitude but of opposite sign. This means that small statistical fluctuations in the two-body contribution can greatly affect both the magnitude and sign of the total pressure. Unfortunately, a similar comparison for the xenon pressure at equilibrium is not possible because to the best of our knowledge, experimental data for the state point we used are not available.

To determine whether the $\dot{g}^2$ dependence is due to the addition of three-body interactions, we plot the two-body and full two- plus three-body contributions to the total pressure separately in Figures 4.6a and 4.6b (for argon and xenon respectively). The results for the two-body pressures are obtained from simulations involving only the two-body BFW potential interactions, without the three-body terms. It is evident that the $\dot{g}^2$ dependence is caused by two-body interactions. The three-body contributions serve only to shift the pressures higher by approximately 0.1 for argon and 0.18 for xenon. Although it could be reasonably expected that the three-body contribution to the total pressure might depend on strain rate, our simulation results suggest that any dependence is very weak for the strain rates covered.
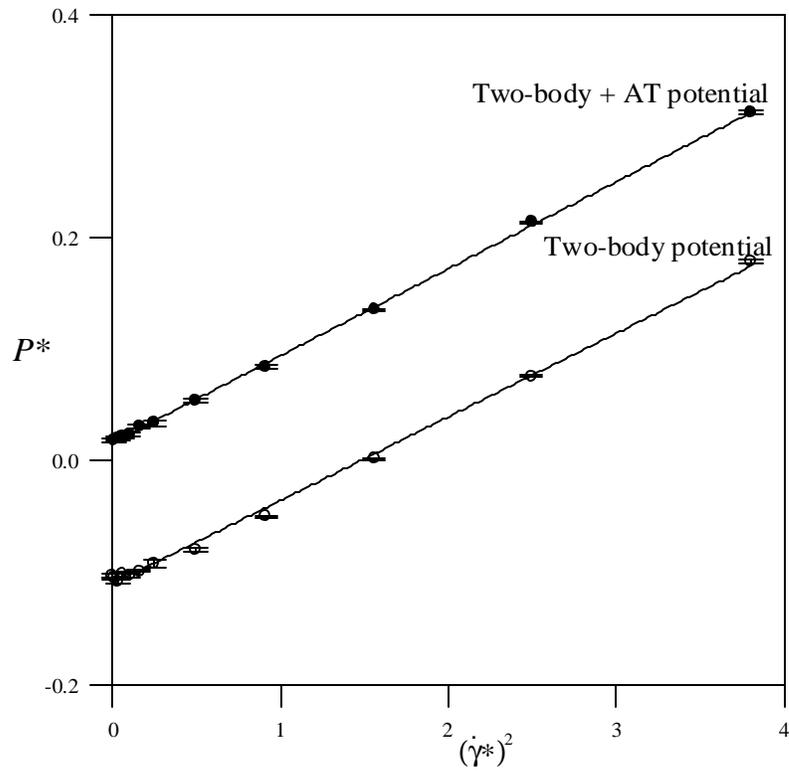
Figure 4.6a Total pressure of argon using only two-body potential (○); total pressure using 2-body + 3-body potentials (●).
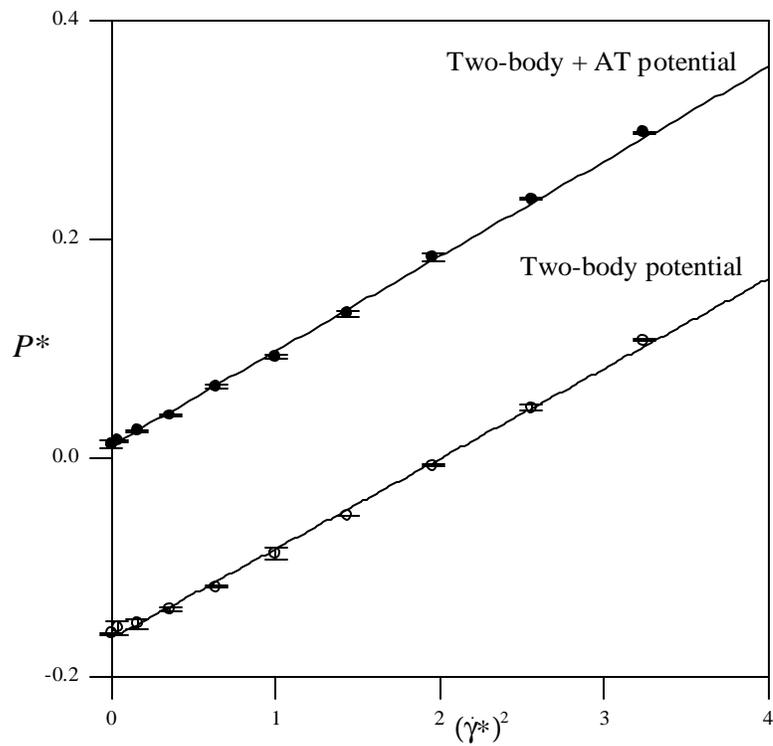
Figure 4.6b Total pressure of xenon using only two-body potential (○); total pressure using 2-body + 3-body potentials (●).

The configurational energy per particle is presented as a function of $\dot{g}^{3/2}$ and $\dot{g}^2$ in Figures 4.7 (a-b) for argon and Figures 4.8 (a-b) for xenon. The E vs. $\dot{g}^{3/2}$ plot does show a weak systematic departure from linearity. For argon the fits in $\dot{g}^{3/2}$ and $\dot{g}^2$ are similar in accuracy, but for xenon the fit in $\dot{g}^2$ is much better. The coefficients of the fits, along with the absolute average deviation are presented in Table 4.3 for argon and in Table 4.4 for xenon.
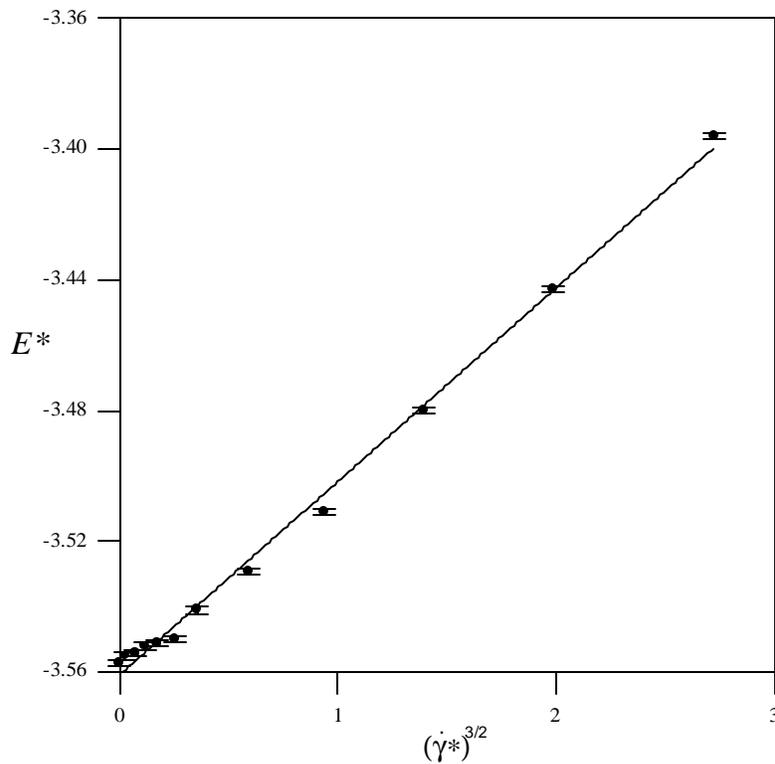
Figure 4.7a The 2-body + 3-body potential energy of argon as function of $\dot{g}^{3/2}$.
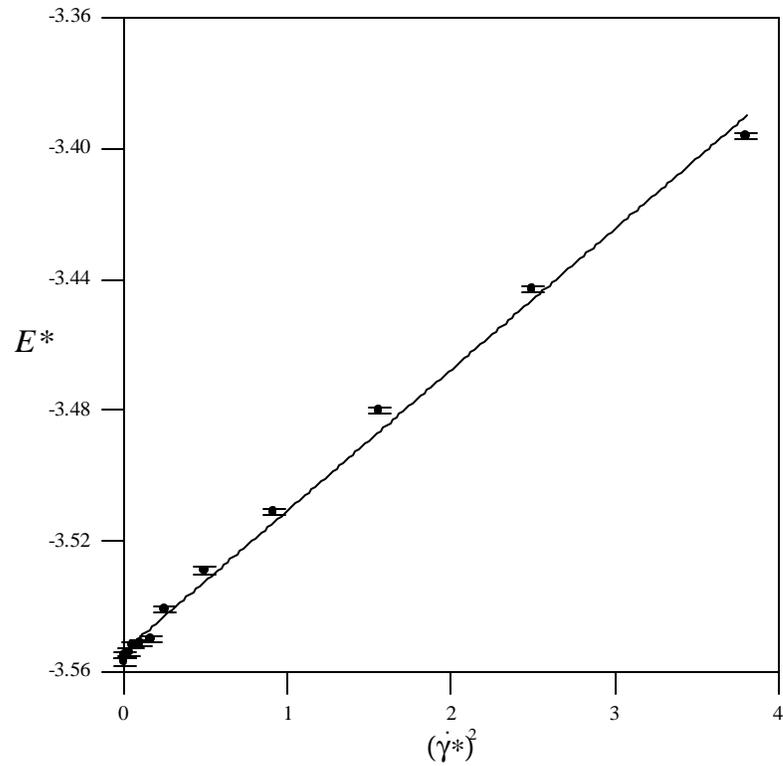
Figure 4.7b The 2-body + 3-body potential energy of argon as function of $\dot{g}^2$.
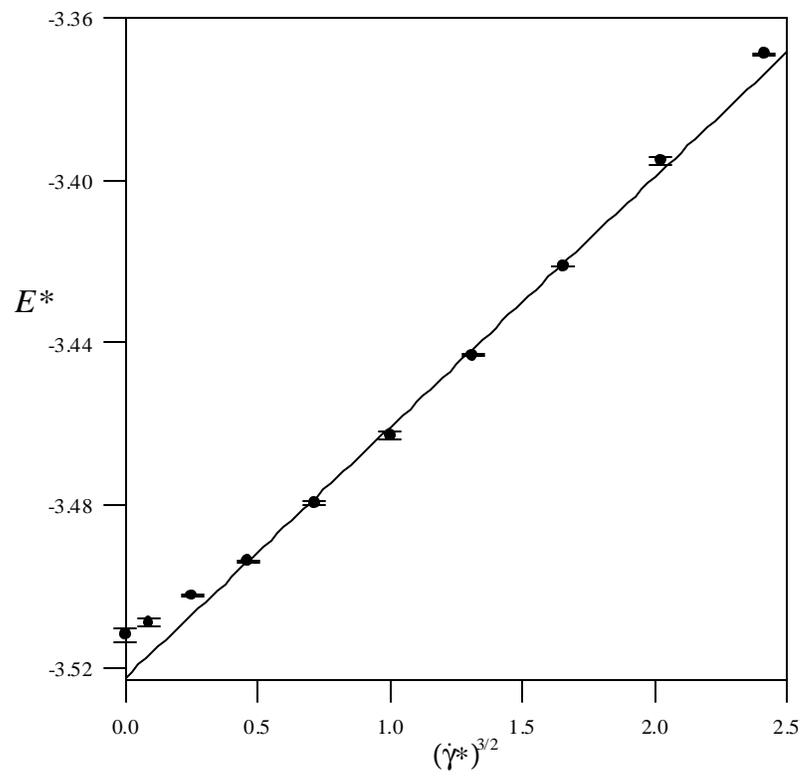
Figure 4.8a The 2-body + 3-body potential energy of xenon as function of $\dot{g}^{3/2}$.
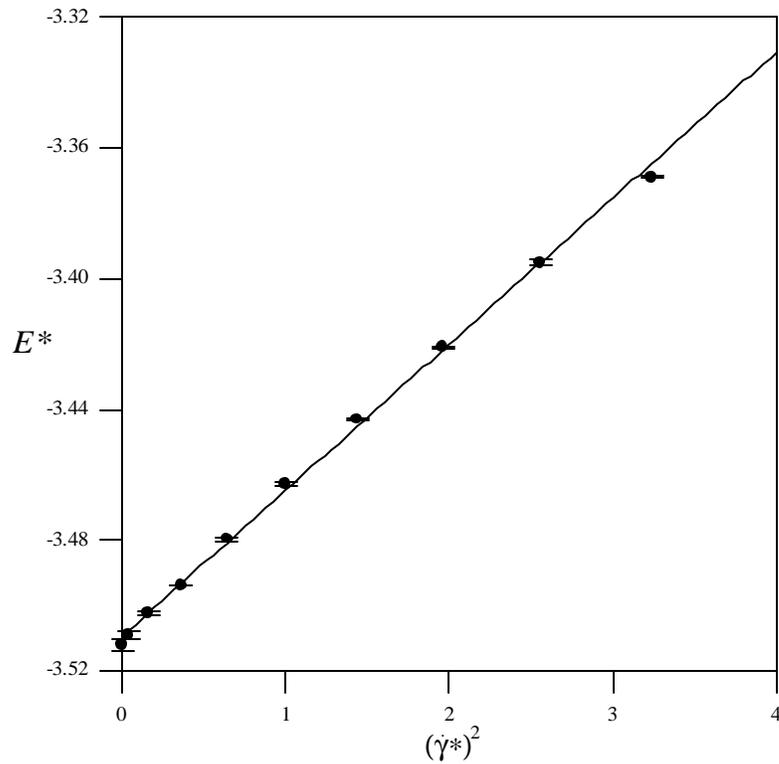
Figure 4.8b The 2-body + 3-body potential energy of xenon as function of $\dot{g}^2$.

The shear viscosity of the fluid, calculated as $h = \dfrac{-\left\langle P_{xy} + P_{yx} \right\rangle}{2\dot{g}}$, is plotted against $\dot{g}$ in Figure 4.9 for argon and in Figure 4.10 for xenon. The viscosity is not a simple function of $\dot{g}^{1/2}$, which is consistent with the conclusion reached by Travis et al [Tra98]. The statistical errors in our viscosity calculations are not sufficiently small to unambiguously determine the functional form of the viscosity profile. Any fit of h vs. $\dot{g}^n$ is reasonable, where $1/2 \le n \le 2$. For argon however, when the data is extrapolated to zero strain-rate, the values of the equilibrium viscosity predicted by the $\dot{g}$, $\dot{g}^{3/2}$ and $\dot{g}^2$ fits $[(757 \pm 1) \times 10^7, (741 \pm 1) \times 10^7, (733 \pm 1) \times 10^7 \, Nsm^{-2}$, respectively] are in good agreement with the experimental value of $740.2 \times 10^7 \, Nsm^{-2}$ [Var75]. The $\dot{g}^{1/2}$ fit actually gives the worst agreement $[(805 \pm 3) \times 10^7 \, Nsm^{-2}]$ with the experiment.
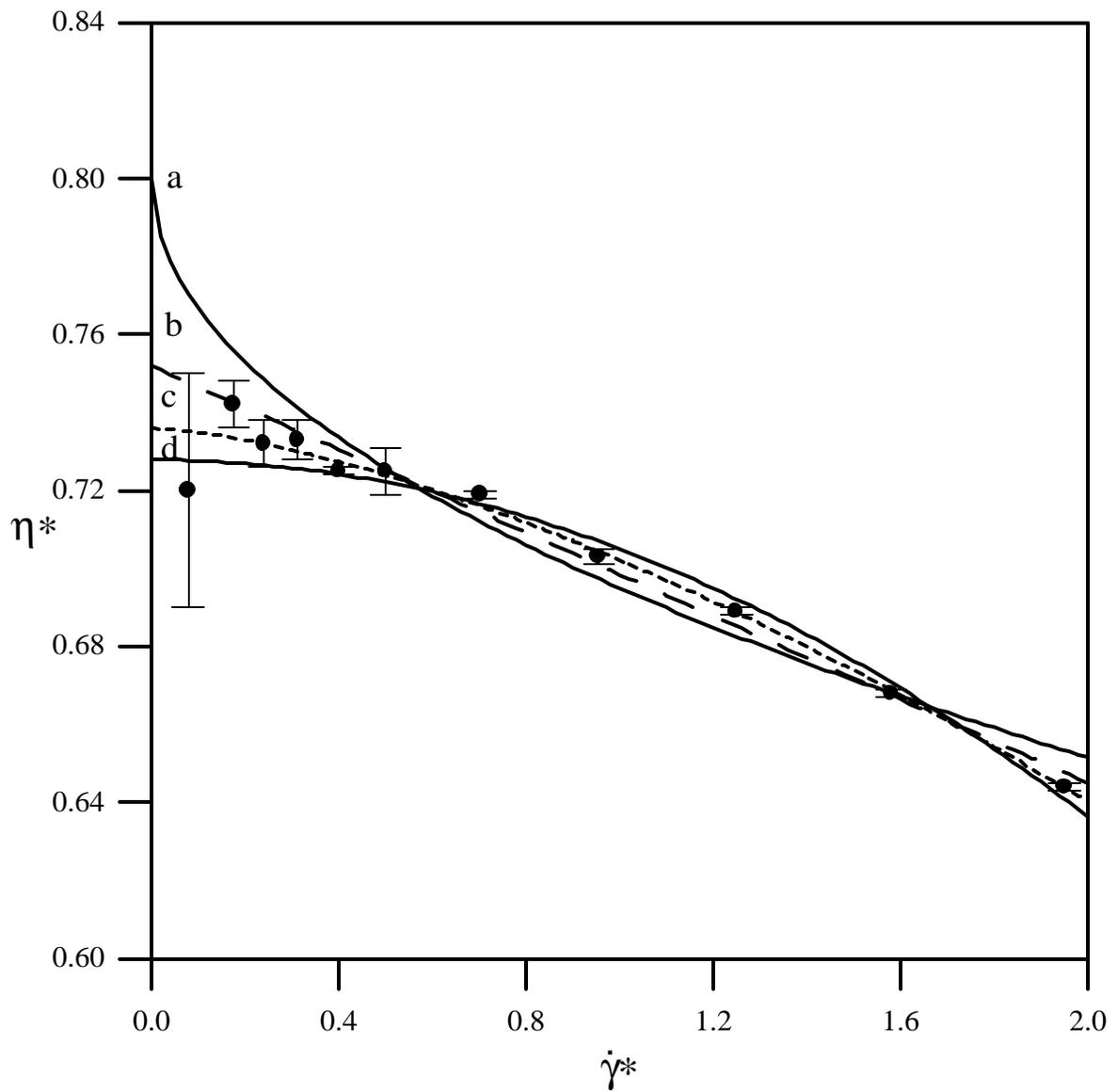
Figure 4.9 Viscosity of argon as function of the strain rate. The lines illustrate different fits with strain rate dependence to the power of (a) 1/2, (b) 1, (c) 3/2 and (d) 2. The parameters of these fits are in Table 4.3.
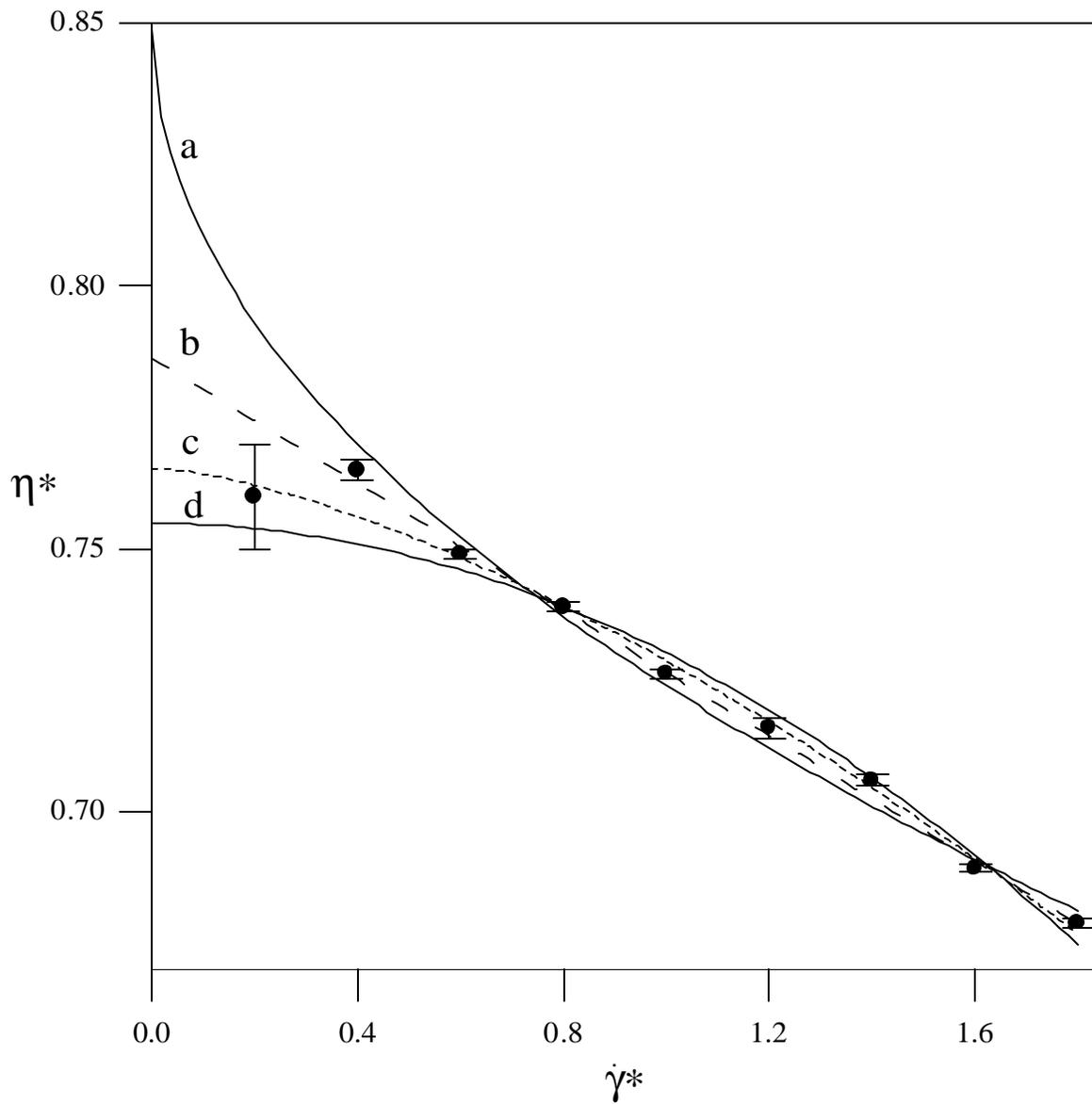
Figure 4.10 Viscosity of xenon as function of the strain rate. The lines illustrate different fits with strain rate dependence to the power of (a) 1/2, (b) 1, (c) 3/2 and (d) 2. The parameters of these fits are in Table 4.4.

Our results differ to those of Lee and Cummings [Lee93, Lee94], who observed the standard $\dot{g}^{3/2}$ dependence of the pressure with strain rate. Lee and Cummings used a system size of 108 argon atoms for both the BFW and BFW + AT calculations. Quantitative error estimates were not reported with their data. Normally, large errors in pressure can be expected for simulations involving such a small number of atoms, which can hinder the correct identification of the strain-rate dependency of pressure. We repeated their simulations for 108 argon atoms at the same state point with only the two-body BFW potential, and present the results for the pressure and energy dependence on strain rate in Figures 4.11 and Figure 4.12, respectively. Our simulations were performed by time averaging over a total of 2×10^{6} time-steps, and our statistics are thus more reliable. We do not include long-range corrections to this set of data, which would only add a constant term to shift the pressure and energy profiles. It does not change the shape, which is what we are interested in. Once again our results confirm the $\dot{g}^{2}$ dependence of both pressure and energy.

We make the observation that a system size of 108 particles is actually too small to account fully for all the possible three-body interactions, and for this reason we performed the 108 atom simulations only with the two-body BFW potential. The cut-off value for the three-body potential should not exceed one quarter of the length of the simulation cell, for geometrical constraints imposed by the three-body interactions (see Appendix 2). In their system, Lee and Cummings used a cell length, L, of 5.67 (reduced units). Their cut off radius was $0.5L = 2.835$ (reduced units), which is too large for their small system size. It is primarily for such reasons that we choose to study a larger system size of 500 atoms.
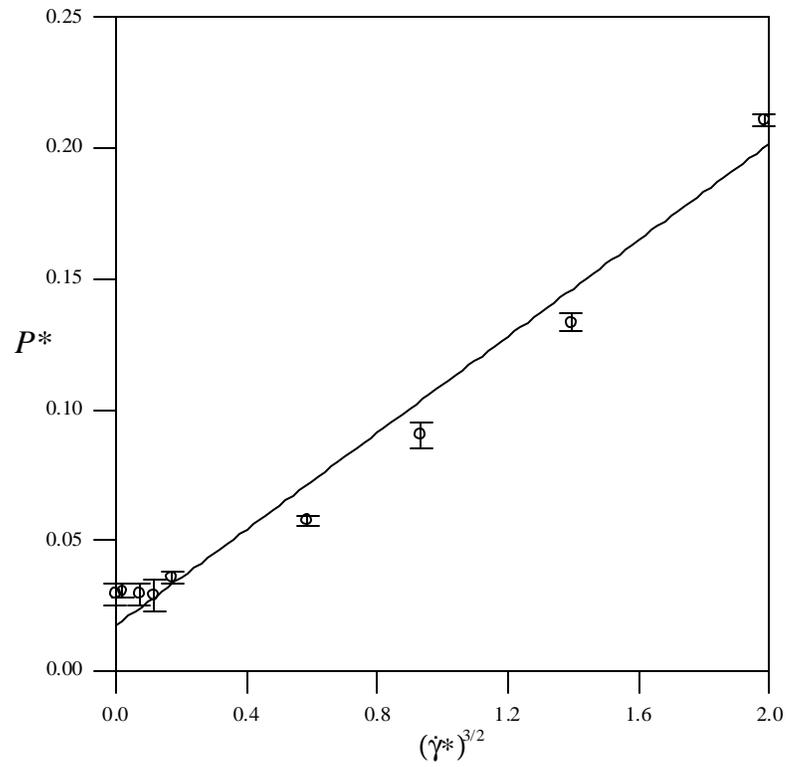
Figure 4.11a Total pressure of argon as function of $\dot{g}^{3/2}$ for 108-atom system.
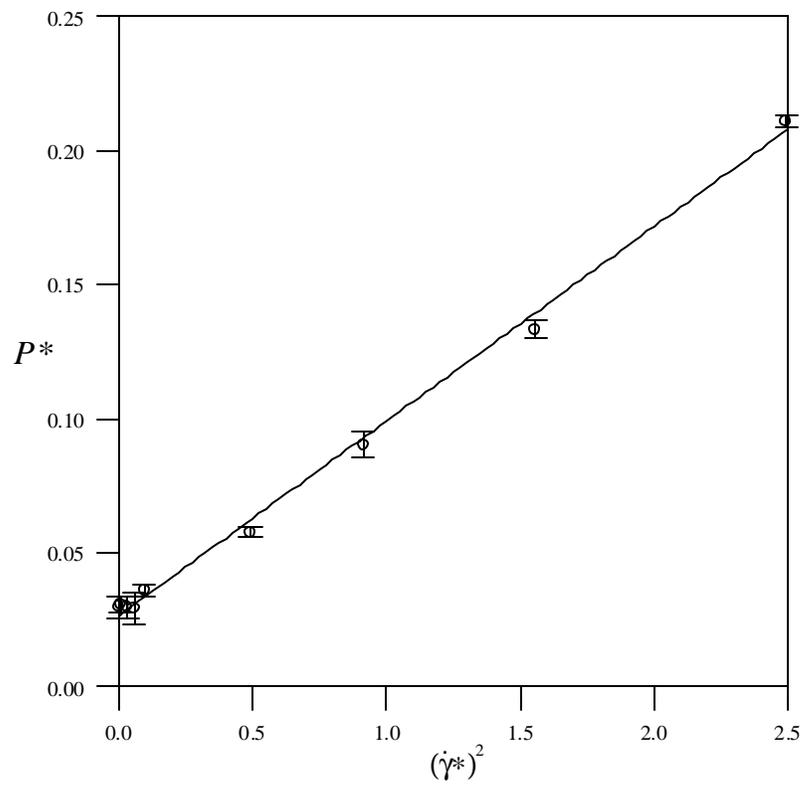
Figure 4.11b Total pressure of argon as function of $\dot{g}^{2}$ for 108-atom system.
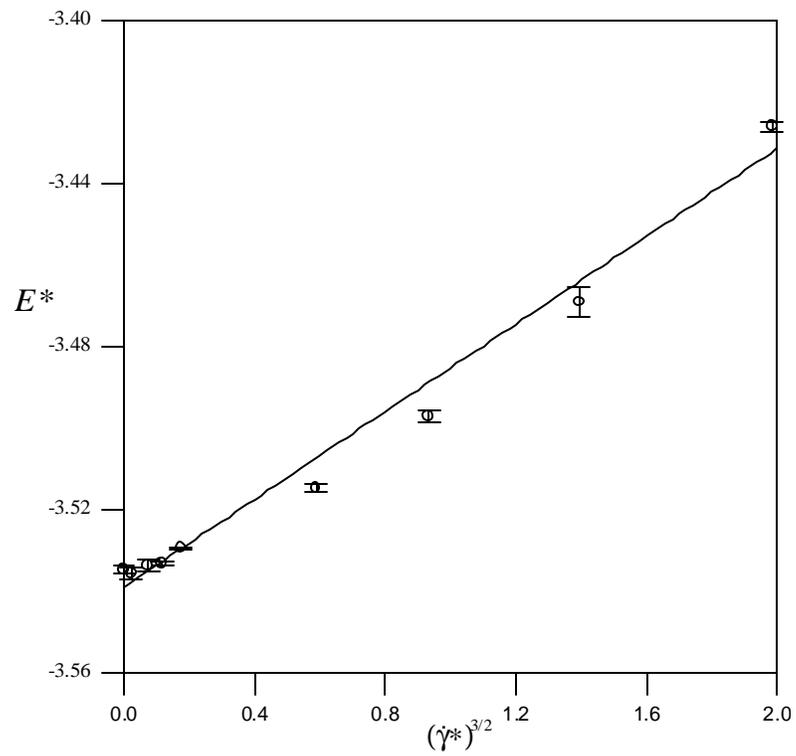
Figure 4.12a Potential energy of argon as function of $\dot{g}^{3/2}$ for 108-atom system.
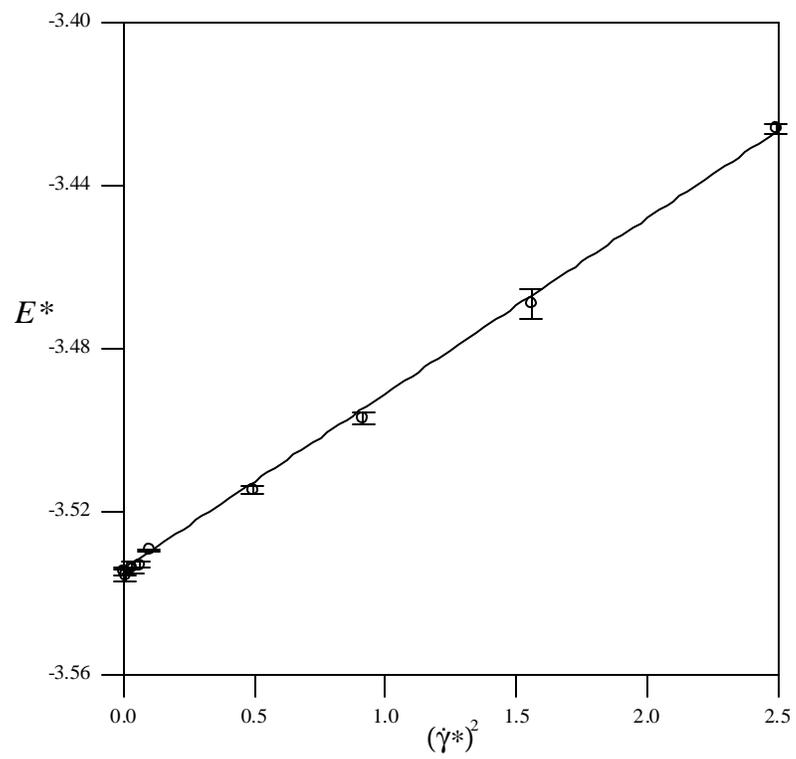
Figure 4.12b Potential energy of argon as function of $\dot{g}^2$ for 108-atom system.

The pressure tensor of the fluid was calculated by the standard Irving-Kirkwood expression [Irv50], modified to include 3-body contributions (see Appendix 2):

$$\langle \mathbf{P} \rangle = \frac{1}{V} \left\langle \sum_{i=1}^{N} \frac{\boldsymbol{p}_i \boldsymbol{p}_i}{m} + \sum_{i=1}^{N-1} \sum_{j>i}^{N} \frac{\boldsymbol{r}_{ij} \boldsymbol{F}_{ij}^{2b}}{m} + \sum_{i=1}^{N-2} \sum_{j>i}^{N-1} \sum_{k>j}^{N} \left[\boldsymbol{r}_{ij} \boldsymbol{F}_{(ij)k}^{3b} + \boldsymbol{r}_{ik} \boldsymbol{F}_{(ik)j}^{3b} + \boldsymbol{r}_{jk} \boldsymbol{F}_{(jk)i}^{3b} \right] \right\rangle (4.5)$$

where $\boldsymbol{p}_i$ is the peculiar momentum of atom i. $\boldsymbol{F}_{ij}^{2b}$ is the two-body force between atom i

and j, and terms involving $\boldsymbol{F}_{(\boldsymbol{ab})k}^{3b} = \dfrac{\partial u_{\boldsymbol{abk}}^{3b}}{\partial \boldsymbol{r}_{\boldsymbol{ab}}}$ are the corresponding three-body

contributions to the total force. The definition of the pressure we used is one third of the of the trace of the pressure tensor (see also Chapter 2):

$$P = \frac{1}{3} Tr \langle \mathbf{P} \rangle = \frac{1}{3V} \left\langle P_{xx} + P_{yy} + P_{zz} \right\rangle \tag{4.6}$$

To check that there was no error in the evaluation of Eq. (4.5), we calculated the configurational part of the pressure by another independent method, namely by integrating over the *total* non-equilibrium pair distribution function. This method will allow us to calculate the two-body potential contribution to the pressure. The three-body potential contribution to the pressure was checked by the relationship $P^{3b} = 3E/V$ ([Bar71a], see also Appendix 2). Since we keep the temperature and density constant, the kinetic contribution to the pressure is constant and given simply by $P^{Kin} = \boldsymbol{r}T$ (see Eq. (2.65)).

During the simulation we calculated the pair radial distribution function, $g(r)$, via Eq. (2.93). Therefore, we were able to calculate the two-body potential pressure in two ways: directly using Eqs. (4.5) and (4.6) (2-body potential part) and *indirectly* using $g(r)$ with Eq. (2.101).

Following the same procedure, we calculated the two-body potential energy directly using the expression:

$$E = \frac{1}{N} \left\langle \sum_{i=1}^{N-1} \sum_{j>i}^{N} u_{ij}^{2b} \right\rangle \tag{4.7}$$

and *indirectly* using Eq. (2.102). Furthermore, we calculated the quantity $\boldsymbol{n}(r)$ using Eq. (2.96) during the same simulation to calculate the shear viscosity *indirectly* via Eq. (2.103).

In Table 4.5 we show the two-body components of the pressure, energy and viscosity (for argon) calculated by Eqs. (2.101), (2.102) and (2.103) alongside of the direct values for different strain rates $\dot{\boldsymbol{g}}$. For every value of $\dot{\boldsymbol{g}}$, the quantities were calculated over a single trajectory of 50000 time-steps. Very good agreement (up to the fourth decimal place) is found between the direct calculations and those involving $g(r,\dot{\boldsymbol{g}})$ and $\boldsymbol{n}(r,\dot{\boldsymbol{g}})$. This agreement suggests that the observed dependencies of the pressure, energy and viscosity with strain rate are not a result of an error in the direct calculations of these properties.

Table 4.5 Two-body contributions of the pressure, energy and viscosity of argon.

$\dot{g}^*$	P_{2body}^* (simulation)	P_{2body}^* ($g(r,\dot{\boldsymbol{g}})$)	E_{2body}^* (simulation)	E_{2body}^* ($g(r,\dot{\boldsymbol{g}})$)	h_{2body}^* (simulation)	h_{2body}^* ($\boldsymbol{n}(r,\dot{\boldsymbol{g}})$)
0.0	-0.7136	-0.7136	-3.6384	-3.6382	-	-
0.702	-0.6720	-0.6720	-3.6118	-3.6118	0.6017	0.6016
0.9555	-0.6382	-0.6383	-3.5941	-3.5941	0.5899	0.5899
1.248	-0.5869	-0.5870	-3.5547	-3.5547	0.5837	0.5837
1.549	-0.5018	-0.5019	-3.5165	-3.5165	0.5671	0.5671
1.95	-0.4045	-0.4046	-3.4738	-3.4738	0.5436	0.5436

In Figure 4.13 we display $g(r,\dot{\boldsymbol{g}})$ and $\boldsymbol{n}(r,\dot{\boldsymbol{g}})$ for the fluid shearing with a strain rate of $\dot{\boldsymbol{g}}^* = 1.95$. Additionally, we include $g(r,\dot{\boldsymbol{g}})$ at equilibrium ($\dot{\boldsymbol{g}}^* = 0$) for comparison purposes. The difference between $g(r,\dot{\boldsymbol{g}})$ for $\dot{\boldsymbol{g}}^* = 0$ and $\dot{\boldsymbol{g}}^* = 1.95$ reflects the change

in the fluid structure with imposed strain rate, which is to be expected. It is well known that $g(r, \dot{g})$ (Eq. (2.94)) is no longer spherically symmetric at large values of $\dot{g}$ [Eva90], but becomes distorted at an angle of 45 degrees to the fluid velocity streamlines.
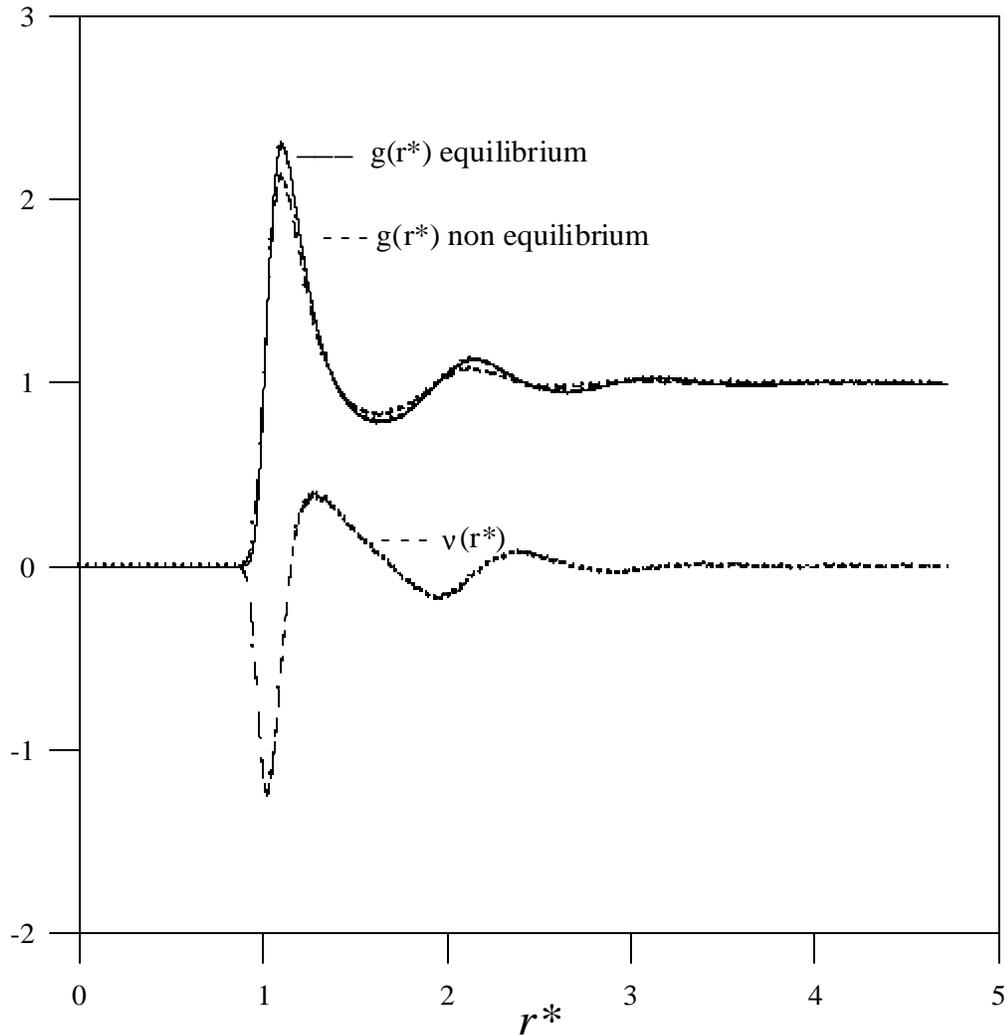
Figure 4.13 $g(r, \dot{g})$ and $n(r, \dot{g})$ for the argon fluid shearing at the highest strain rate used ($\dot{g}^* = 1.95$). $g(r, \dot{g})$ at equilibrium ($\dot{g}^* = 0$) is also reported.

There is an additional check we can perform to ensure that the SLLOD algorithm was correctly implemented, and that the pressure tensor was correctly calculated. For thermostatted planar Couette flow, the rate of energy dissipation may be expressed as:

$$\dot{H}(t) = -VP_{xy}\dot{\boldsymbol{g}} - \boldsymbol{a} \sum_{i=1}^{N} \frac{\boldsymbol{p}_i \cdot \boldsymbol{p}_i}{m} \qquad (4.8)$$

where $\dot{H}(t)$ is the time derivative of the total internal energy. For the algorithm to be

working correctly, and for the shear stress to be correctly calculated, the right-hand-side

(RHS) of Eq. (4.8) must equal the left-hand-side (LHS) for all t. This was indeed found

to be the case in all our simulations, as seen in Figure 4.14.
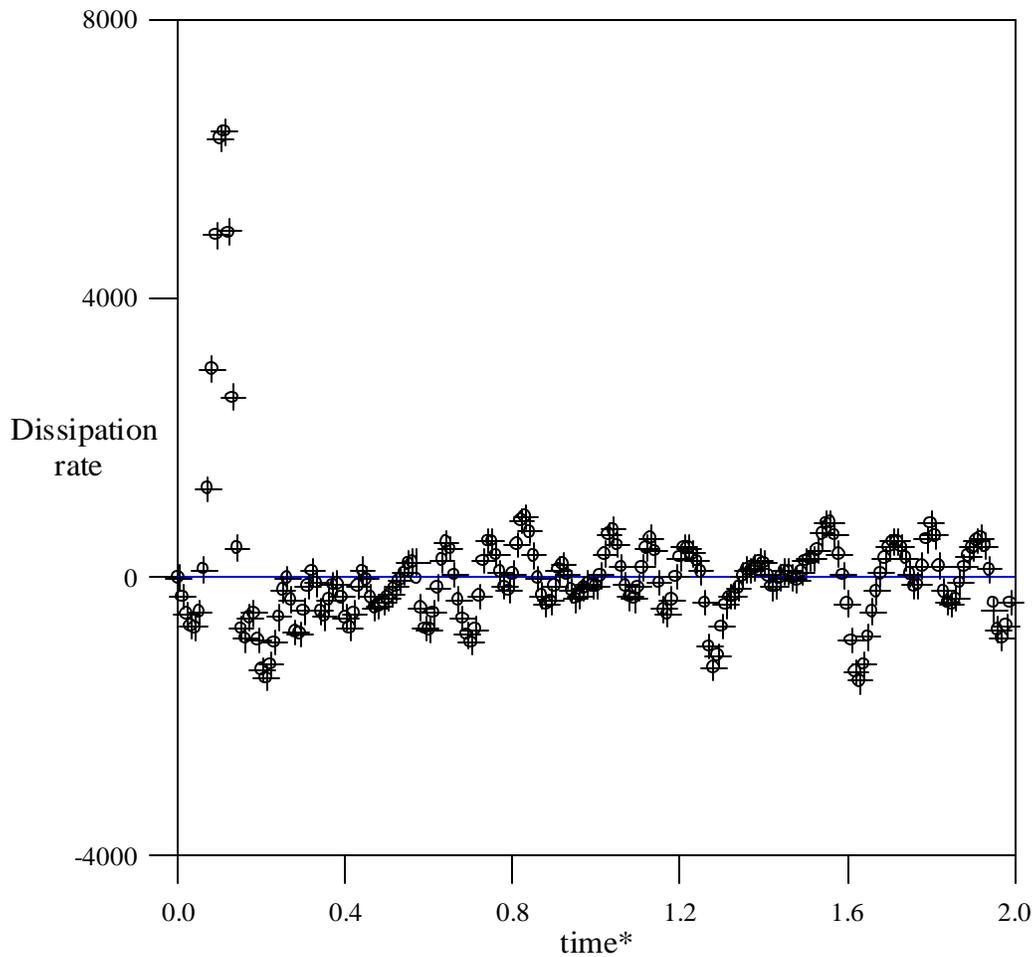
Figure 4.14 Comparison of RHS of Eq. (4.8) (+), and LHS (○). Note that at t^*=0 the
strain rate is imposed, and the fluid takes time to relax to a non-equilibrium steady state.

Figure 4.14 displays the results for a simulation where the shear stress is applied at $t^*=0$, from an equilibrium state. The high peak close to $t^*=0$ reveals that an initial amount of energy, provided by the shearing, goes to change the internal structure of the fluid, from an equilibrium state to a non-equilibrium one. Referring to Figure 4.13, this amount of energy is utilized to distort the equilibrium $g(r)$. After this initial transition, the system reaches a steady state.

Additionally, we checked that the hydrostatic pressure calculation was correct by calculating the dissipation for a fluid undergoing planar elongation. The dissipation is related to differences in the diagonal elements of the pressure tensor, and the dissipation rate is given as:

$$\dot{H}(t) = -V\dot{e}\left[P_{xx} - P_{yy}\right] - a\sum_{i=1}^{N}\frac{p_i \cdot p_i}{m} \qquad (4.9)$$

Here $\dot{e}$ is the elongation strain rate, and the fluid expands in the x-direction, whilst simultaneously contracting in the y-direction. Details of the simulation algorithm for planar elongation can be found elsewhere [Tod97, Tod99]. Our simulations confirmed the equivalence of the RHS and LHS of Eq. (4.9).

Previous work [Ryc88] that had attempted to show the analytic dependence of the viscosity on $\dot{g}$ was criticized for the relatively high rates of strain used [Tra98]. Large strain rates can induce unwanted string phases, i.e., highly ordered solid-like configurations. These string phases arise for high Reynolds number flows [Erp84], where the assumption of a linear streaming velocity profile is questionable. The linear profile is imposed upon the flow via the SLLOD equations of motion. For a freely shearing system with Lees-Edwards periodic boundary conditions, high Reynolds number flows should exhibit an S-shaped kink in the streaming velocity profile. If the assumed (linear) and actual streaming velocities are not the same, the thermostat

interprets this deviation as heat, and applies an additional force to the equations of motion for the momenta (see Eq. (2.79)). It is this additional force appearing in the term involving $\boldsymbol{a}$ that serves to stabilize the linear velocity profile and enhance the ordering of the fluid by reducing the rate of entropy production. Once the fluid's ordering is enhanced, its viscosity and pressure are reduced dramatically from their true values, which can lead to incorrect dependencies on $\dot{\boldsymbol{g}}$.

In Figure 4.15 we project a 3-dimensional snapshot of the argon fluid onto a 2-dimensional surface in the x-y plane. The fluid was sheared at the highest value of $\dot{\boldsymbol{g}}$ which we simulated, $\dot{\boldsymbol{g}}^* = 1.95$.
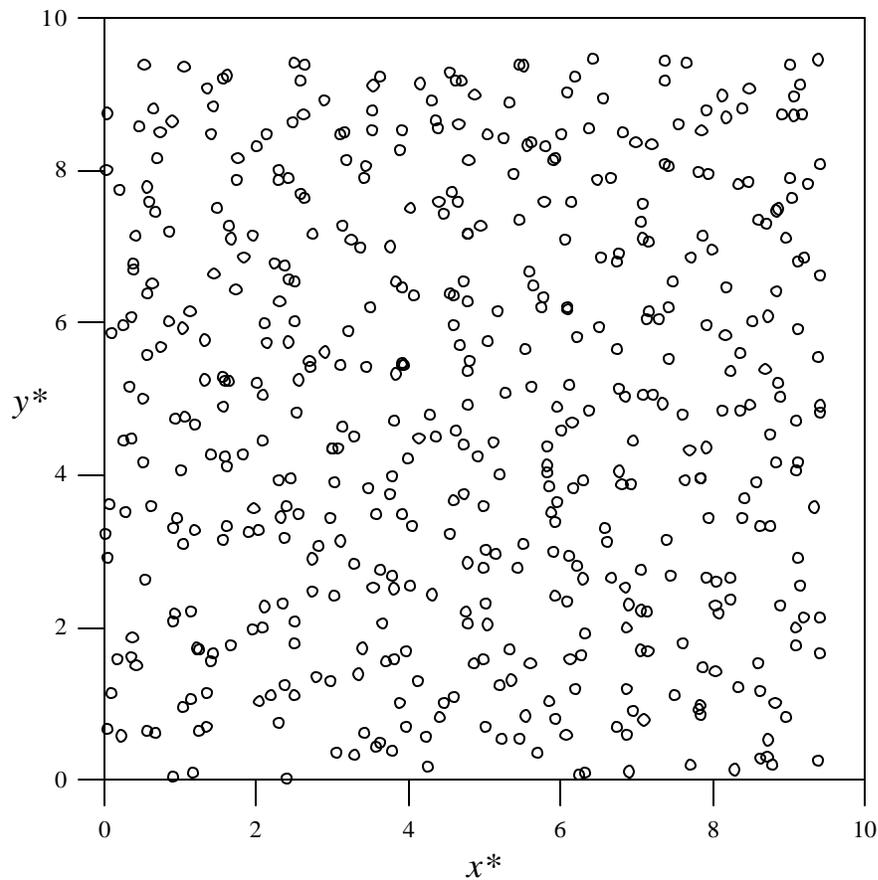
Figure 4.15 Two-dimensional projection onto the x-y plane of a three-dimensional snapshot of the argon fluid, shearing at the highest strain rate used ($\dot{\boldsymbol{g}}^* = 1.95$).

There is no obvious enhancement in the structure of the fluid. For our system, strings were only noticeable at very high values of $\dot{g}$, typically $\dot{g}^* > 5$. This is in contrast to work by Evans et al. [Eva92], who found evidence of strings for values of $\dot{g}^*$ as low as ~ 2. However, their simulations were performed on a Weeks-Chandler-Anderson (WCA) fluid [Wee71]. Our simulations have been performed on BFW fluids, both with and without the additional three-body term, where the range over which fluid atoms interact is significantly greater than for WCA fluids. In Figure 4.16 we show a full 3-dimensional snapshot of the fluid sheared at $\dot{g}^* = 11$, where now the appearance of strings is very pronounced. If strings were formed in our simulations, the anticipated side-effect should be to dramatically reduce the values of the viscosity and hydrostatic pressure at higher strain rates. Our data clearly does not support this.
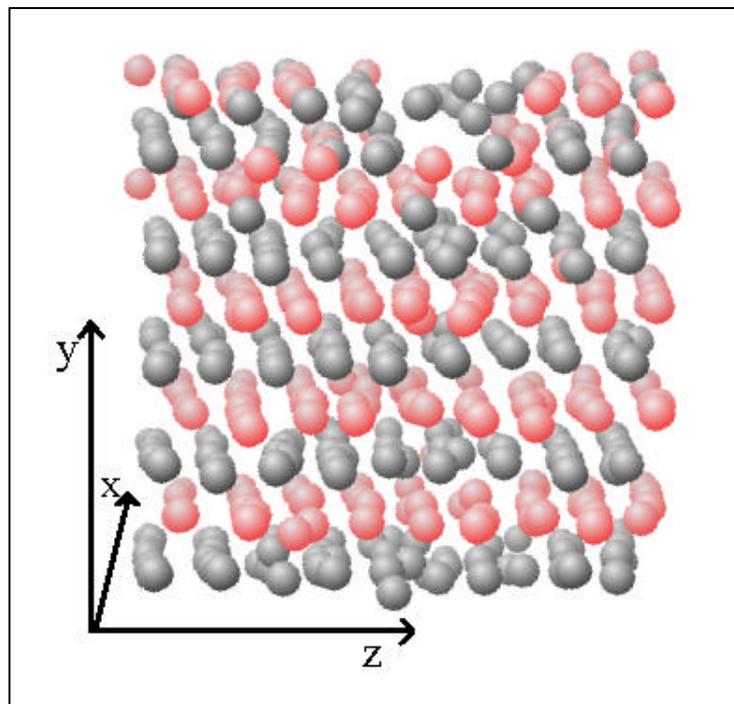
Figure 4.16 Full three-dimensional snapshot of the argon fluid, shearing at high value of $\dot{g}^* = 11$.

Finally, we checked the dependence of the pressure, energy and viscosity profiles on the size of the cut-off potential radius used. While the results presented here for argon were performed with a two-body cut-off radius of $r_{cut-off}^{2b} = 0.5L = 4.726$ (reduced units), we also performed simulations at a smaller cut-off of $r_{cut-off}^{2b} = 2.28$ (reduced units) for an argon system of 500 atoms. The shapes of these profiles remained unchanged.

4.3 Relationship between two-body and three-body potentials from NEMD simulation

It is of interest to determine the effect of different strain rates on the validity of the relationship (Eq. (3.3)). The validity of such a simple relationship for NEMD was uncertain because of the added influence of factors such as variation in the strain rate. Consequently, we analyzed the ratio between the two (E_2) and the three (E_3) body potential energies obtained with planar Couette flow simulations for different state points and strain rates.

The ratio of three-body to two-body energies for argon at different densities and temperatures is shown in Figure 4.17 as a function of strain rate. The temperatures and densities represent different state points on the liquid-phase branch of the vapour-liquid coexistence curve of pure argon. Irrespective of the state point, it is apparent that the ratio of the energies is largely independent of the strain rate. The dependence of the energy ratio on density is illustrated in Figure 4.18. The values predicted by Eq. (3.3) are also illustrated for comparison. This simple relationship fits the NEMD simulation data with an average absolute deviation of 2.3%. This is close to the same quality of

agreement (2%) that was obtained for the Monte Carlo study of equilibrium properties reported in section 3.2.

As seen in the previous sections, the transport properties of fluids, such as shear viscosity, are an aspect of fluid behaviour that could potentially benefit from the use of accurate pair-potentials and three-body interactions. In common with other applications of molecular simulation, the transport properties of fluids have largely been investigated using effective potentials. Therefore, other investigations are necessary to determine if Eq. (3.3) may be used in NEMD simulations to incorporate the effect of three-body interactions without the computational cost of a full three-body calculation.
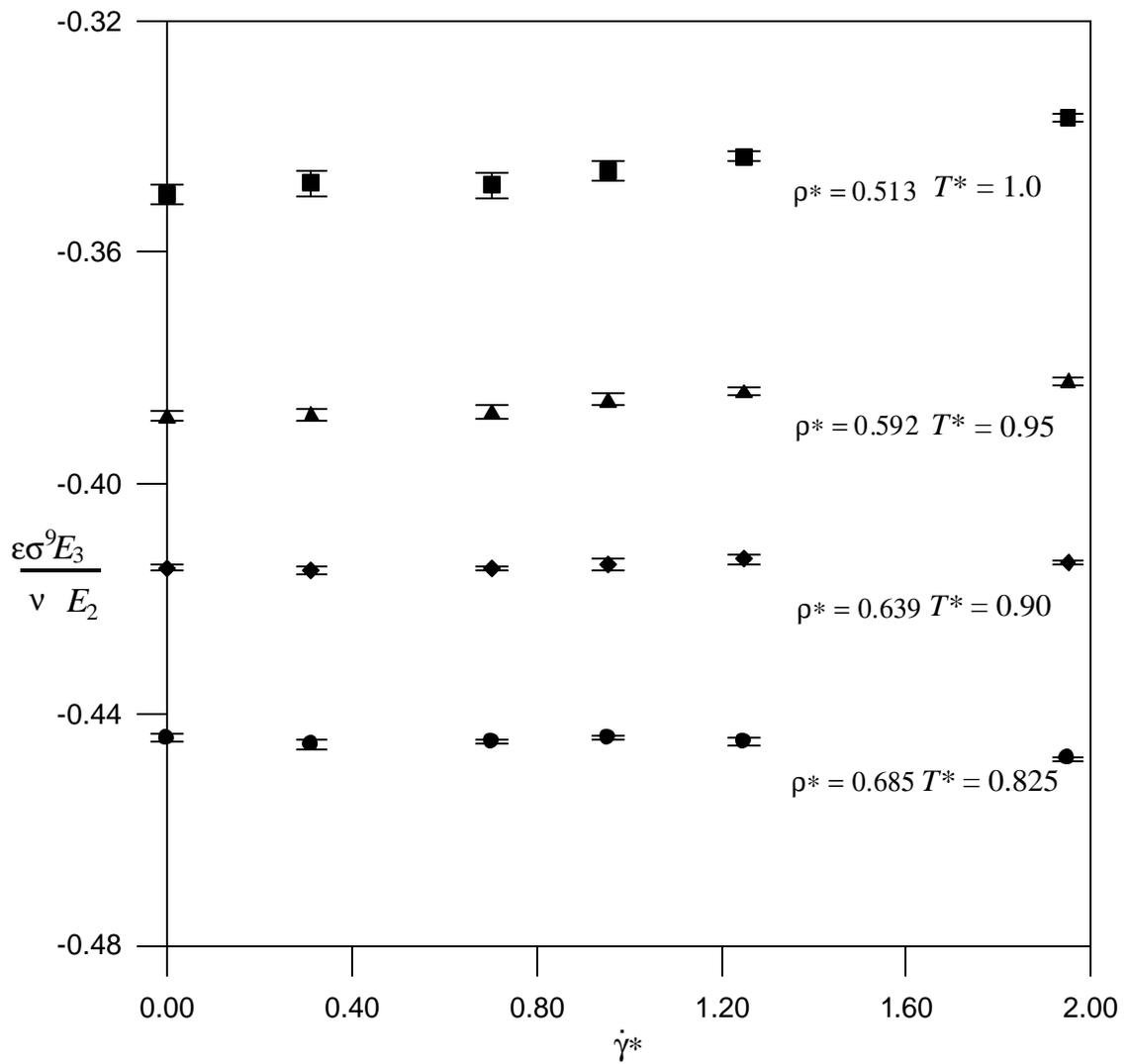
Figure 4.17 The ratio of three-body and two-body energies of argon obtained from NEMD at different state points and different strain rates.
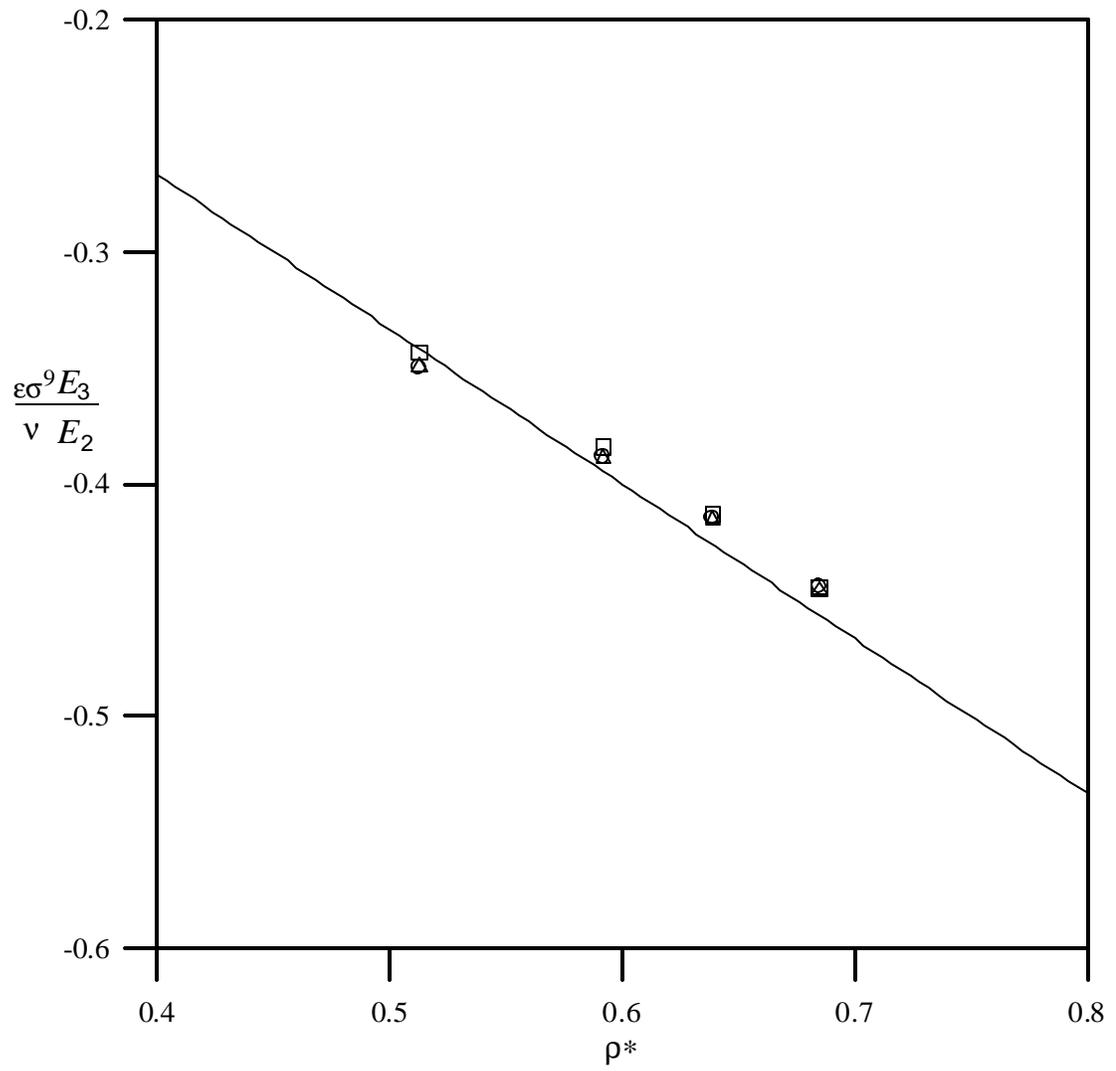
Figure 4.18. The ratio of three-body and two body energies for argon obtained from NEMD at different strain rates ($\dot{\boldsymbol{g}}^* = 0$ ($\bigcirc$), 0.702 ($\triangle$), 1.428 ($\square$)) as a function of density. The line through the points was obtained from Eq. (3.3).

Chapter 5

Conclusions and Recommendations

The results we present in this work and in the literature [Mar99, Mar00, Mar01a, Mar01b, Mar01c, Mar01d] demonstrate that three-body interactions play an important role in the overall interatomic interactions of noble gases. This is demonstrated by the good agreement between our simulation results and the experimental data for both equilibrium and non-equilibrium systems. It is our opinion that the inclusion of the three-body forces in molecular simulations attempting to reproduce accurately experimental data is worthwhile and necessary. This practice would be beneficial since it would provide new insight into the three-body effects. In fact, it may be inferred that in other atomic and molecular systems three-body forces have an equivalent importance. It is desirable to investigate this more extensively. Studying three-body potentials in complex systems requires a significant effort in terms of experimental development, theoretical approaches and computational costs [Elr94]. Nevertheless, we strongly believe that it is an important area worthy of continued investigation.

The use of effective pair potentials is obviously justified if applied either to corroborate a theory or to compare two similar molecular simulation techniques. For example the attempt, in earlier work, to validate the predictions of mode coupling theory [Kaw73] using the Lennard-Jones potential or even more simplistic potentials was reasonable. In fact, mode coupling theory predicts the general behaviour of the

viscosity and pressure vs. the strain rate, and is consequently not restricted to realistic potentials. On the other hand, the reproduction of experimental data with high accuracy and for a wide range of state points may be a prohibitive task with effective pair potentials. However, the intent to predict the experimental results with sufficient accuracy using effective pair potentials without incurring excessive computational costs is understandable and apparently feasible. There are indications that three-body effects in different properties may be accounted via mean field models [Ege88]. This approach consists in considering the many-body forces experienced by the molecules as a uniform background. The total intermolecular interactions are then considered pair-additive since they are given by a realistic pair potential corrected with this background contribution. Mean field potentials are usually temperature independent and density dependent. Their predictions are more accurate for bulk properties. Estimates on microscopic properties show some deficiencies [Ege88].

The relationship in Eq. (3.3) represents a density dependent pair potential, and it may be envisaged as an effective potential. It has the feature to have been derived from full two-body + three-body calculations. The correction term appearing in Eq. (3.3) may be considered as a background contribution due to three-body effects. The relationship was not the result of a mean field derivation, but it may represent evidence that a mean field model can be applied for the systems studied.

It is noteworthy to point out that the relationship in Eq. (3.3) is not supposed to provide high accuracy and, strictly speaking, it should be used in the range of densities and temperatures in which it was derived. To the best of our knowledge, this is the first time that such a relationship has been derived using simulation data from full two-body + three-body potential simulations. We believe that this procedure can be used to derive similar effective potentials for other systems.

In this work we did not apply three-body short-range potentials. Our results seem to demonstrate that, at least for the systems and the state points studied, these potentials should not give a significant contribution. Naturally, ours is just an *a posteriori* inference. But, very recent findings from Bukowsky and Szalewicz [Buk01] concerning the cancellations between three-body short-range potentials also strongly indicate that the triple-dipole potential is an excellent approximation of the total three-body energy. Further theoretical investigations in this direction are necessary.

A further deficiency in the literature is the investigation of the third order distribution function, $g(r_1, r_2, r_3)$. From a molecular simulation viewpoint the calculation of $g(r_1, r_2, r_3)$ is feasible, even if it is considerably more time consuming than that of the pair distribution function. The knowledge of $g(r_1, r_2, r_3)$ enables one to choose more correctly the three-body cut-off and to test accurately the superposition approximation [Bar71a] used for long range corrections. A more precise calculation of the liquid state pressure may be a beneficial consequence of such an investigation. As pointed out in Chapter 3, the total pressure is the sum of the kinetic and potential contributions. These are of the same magnitude and opposite sign. The contribution from the three-body long-range corrections may be crucial in order to match the experimental data for the liquid state.

In the past, some simulations with three-body potentials used 108-atom systems [Mur71, Bar71a, Lee94]. The size of such systems may not be compatible with an accurate determination of the three-body effects. In our work we used a 500-atom system, which was demonstrated to provide a good accuracy. However, investigations on possible scale effects may be beneficial. This is true also for mean field theory. In fact, there is the suspicion that many-body potentials show mean field behaviour because of the short cut-off applied in the simulations [Ege88].

The results for vapour-liquid coexisting phases encourage performing further computer simulations with realistic potentials. This may improve the prediction of quantities like critical temperature and density, in particular of substances for which these properties are difficult to obtain from experiment. It also very interesting to pursue the suggestion of Frenkel and Smit [Fre96] to use direct molecular dynamics techniques to investigate coexisting phases, since nowadays the increasing computer speed and use of parallel computers can allow such attempts.

We have demonstrated that use of accurate two- and three-body potentials for shearing liquid argon and xenon displays significant departure from the expected strain rate dependencies of the pressure, energy and shear viscosity. For the first time, the pressure is convincingly observed to vary linearly with an apparent analytic $\dot{g}^2$ dependence, in contrast to the predicted $\dot{g}^{3/2}$ dependence of mode-coupling theory. This dependence results primarily from the two-body potential. The 3-body term only serves to raise the magnitude of the total pressure. Recent work using a Lennard-Jones potential found a similar deviation from mode-coupling theory [Mat00, GeJ01]. In particular, they found deviations from mode coupling theory predictions away from the triple point. Further work is required to understand this behaviour. The shear viscosity is also seen not to be a simple function of $\dot{g}^{1/2}$, and our data are in general agreement with recent work of other authors [Tra98]. Our best extrapolation of the zero-shear viscosity for argon gives excellent agreement (within 1%) with the known experimental data. From the best of our knowledge, this the first time that such accuracy has been achieved with NEMD simulations. Once again, this encourages performing simulations with accurate potentials for transport properties.

Appendix 1

Long-Range Corrections for BFW Potential

In this appendix we give the analytic derivation of the long-range corrections for the BFW potential [Bar71, see also Chapter 2], more precisely for the two-body pressure and energy assuming the pair distribution $g(r)$ function equals unity over the cut-off. In the cases of the krypton and xenon potentials [Bar74, see also Chapter 2], the procedure is similar.

The two-body energy in terms of $g(r)$ may be expressed as [All87, see also Eq. (2.102)]:

$$E^{2b} = 2\boldsymbol{p}N\boldsymbol{r} \int_0^\infty g(r)u^{2b}r^2dr \quad . \tag{A1.1}$$

With a simulation cut-off r_c and assuming $g(r)$ can be approximated by unity after the cut-off (see for example Figure 4.13), the long-range corrections for the energy can be written as:

$$E_{lrc}^{2b} = 2\boldsymbol{p}N\boldsymbol{r} \int_{r_c}^\infty u^{2b}r^2dr \quad . \tag{A1.2}$$

Substituting the BWF potential in Eq. (A1.2) gives:

$$E_{lrc}^{2b} = 2pNr\, r_m^3 \int\limits_{\frac{r_c}{r_m}}^{\infty} \left\{ e\left[\sum_{i=0}^{5} A_i (x-1)^i \exp[a(1-x)] - \sum_{j=0}^{2} \frac{C_{2j+6}}{d+x^{2j+6}} \right] \right\} x^2 dx \ . \qquad (A1.3)$$

where $x = \dfrac{r}{r_m}$ and r_m is the value where the potential is a minimum. To solve the

integral in Eq. (A1.3) we have to solve each term. Consider the following terms:

$$\left. \begin{aligned} &\int\limits_{\frac{r_c}{r_m}}^{\infty} x^2 \sum_{i=0}^{5} A_i(x-1)^i \exp[a(1-x)]dx = \\[2mm] &\int\limits_{\frac{r_c}{r_m}}^{\infty} x^2 A_0 \exp[a(1-x)]dx + \int\limits_{\frac{r_c}{r_m}}^{\infty} x^2 A_1(x-1)\ \exp[a(1-x)]dx + \\[2mm] &\int\limits_{\frac{r_c}{r_m}}^{\infty} x^2 A_2(x-1)^2 \exp[a(1-x)]dx + \int\limits_{\frac{r_c}{r_m}}^{\infty} x^2 A_3(x-1)^3 \exp[a(1-x)]dx + \\[2mm] &\int\limits_{\frac{r_c}{r_m}}^{\infty} x^2 A_4(x-1)^4 \exp[a(1-x)]dx + \int\limits_{\frac{r_c}{r_m}}^{\infty} x^2 A_5(x-1)^5 \exp[a(1-x)]dx = \\[2mm] &I_0 + I_1 + I_2 + I_3 + I_4 + I_5 \end{aligned} \right\}$$

$$(A1.4)$$

where:

$$I_0 = A_0 \int\limits_{\frac{r_c}{r_m}}^{\infty} x^2 \exp[a(1-x)]dx \qquad (A1.5)$$

$$I_1 = A_1 \int\limits_{\frac{r_c}{r_m}}^{\infty} (x^3 - x^2)\ \exp[a(1-x)]dx \qquad (A1.6)$$

$$I_2 = A_2 \int_{\frac{r_c}{r_m}}^{\infty} (x^4 - 2x^3 + x^2) \ \exp[a(1-x)]dx \qquad (A1.7)$$

$$I_3 = A_3 \int_{\frac{r_c}{r_m}}^{\infty} (x^5 - 3x^4 + 3x^3 - x^2) \ \exp[a(1-x)]dx \qquad (A1.8)$$

$$I_4 = A_4 \int_{\frac{r_c}{r_m}}^{\infty} (x^6 - 4x^5 + 6x^4 - 4x^3 + x^2) \ \exp[a(1-x)]dx \qquad (A1.9)$$

$$I_5 = A_5 \int_{\frac{r_c}{r_m}}^{\infty} (x^7 - 5x^6 + 10x^5 - 10x^4 + 5x^3 - x^2) \ \exp[a(1-x)]dx \qquad (A1.10)$$

Now consider the following integrals:

$$< 0 >= \int \exp[a(1-x)]dx = -\frac{1}{a}\exp[a(1-x)] + const. \qquad (A1.11)$$

$$< 1 >= \int x\exp[a(1-x)]dx = \frac{1}{a}\{-x\exp[a(1-x)] + < 0 >\} + const. \qquad (A1.12)$$

$$< 2 >= \int x^2 \exp[a(1-x)]dx = \frac{1}{a}\{-x^2\exp[a(1-x)] + 2 < 1 >\} + const. \qquad (A1.13)$$

$$< 3 >= \int x^3 \exp[a(1-x)]dx = \frac{1}{a}\{-x^3\exp[a(1-x)] + 3 < 2 >\} + const. \qquad (A1.14)$$

$$< 4 >= \int x^4 \exp[a(1-x)]dx = \frac{1}{a}\{-x^4\exp[a(1-x)] + 4 < 3 >\} + const. \qquad (A1.15)$$

$$< 5 >= \int x^5 \exp[a(1-x)]dx = \frac{1}{a}\left\{- x^5 \exp[a(1-x)]+5 < 4 >\right\}+ const. \qquad \text{(A1.16)}$$

$$< 6 >= \int x^6 \exp[a(1-x)]dx = \frac{1}{a}\left\{- x^6 \exp[a(1-x)]+6 < 5 >\right\}+ const. \qquad \text{(A1.17)}$$

$$< 7 >= \int x^7 \exp[a(1-x)]dx = \frac{1}{a}\left\{- x^7 \exp[a(1-x)]+7 < 6 >\right\}+ const. \qquad \text{(A1.18)}$$

Using these expressions and the following relations:

$$R = \frac{r_c}{r_m} \qquad ; \qquad Q = \frac{1}{a}\exp\left[a\left(1-\frac{r_c}{r_m}\right)\right], \qquad \text{(A1.19)}$$

we can solve the following integrals as:

$$< 0 >'= \int_{\frac{r_c}{r_m}}^{\infty} \exp[a(1-x)]dx = Q \qquad \text{(A1.20)}$$

$$< 1 >'= \int_{\frac{r_c}{r_m}}^{\infty} x\exp[a(1-x)]dx = -\frac{1}{a}\left\{-\frac{r_c}{r_m}\exp\left[a\left(1-\frac{r_c}{r_m}\right)\right]+ < 0 >'\right\}= Q\left(R-\frac{1}{a}\right) \quad \text{(A1.21)}$$

$$< 2 >' = \int_{\frac{r_c}{r_m}}^{\infty} x^2 \exp[a(1-x)]dx = -\frac{1}{a}\left\{-\left(\frac{r_c}{r_m}\right)^2 \exp\left[a\left(1-\frac{r_c}{r_m}\right)\right]+2<1>'\right\} =$$

(A1.22)

$$Q\left(R^2 - \frac{2}{a}R + \frac{2}{a^2}\right)$$

$$< 3 >' = \int_{\frac{r_c}{r_m}}^{\infty} x^3 \exp[a(1-x)]dx = -\frac{1}{a}\left\{-\left(\frac{r_c}{r_m}\right)^3 \exp\left[a\left(1-\frac{r_c}{r_m}\right)\right]+3<2>'\right\} =$$

(A1.23)

$$Q\left(R^3 - \frac{3}{a}R^2 + \frac{6}{a^2}R - \frac{6}{a^3}\right)$$

$$< 4 >' = \int_{\frac{r_c}{r_m}}^{\infty} x^4 \exp[a(1-x)]dx = -\frac{1}{a}\left\{-\left(\frac{r_c}{r_m}\right)^4 \exp\left[a\left(1-\frac{r_c}{r_m}\right)\right]+4<3>'\right\} =$$

(A1.24)

$$Q\left(R^4 - \frac{4}{a}R^3 + \frac{12}{a^2}R^2 - \frac{24}{a^3}R + \frac{24}{a^4}\right)$$

$$< 5 >' = \int_{\frac{r_c}{r_m}}^{\infty} x^5 \exp[a(1-x)]dx = -\frac{1}{a}\left\{-\left(\frac{r_c}{r_m}\right)^5 \exp\left[a\left(1-\frac{r_c}{r_m}\right)\right]+5<4>'\right\} =$$

(A1.25)

$$Q\left(R^5 - \frac{5}{a}R^4 + \frac{20}{a^2}R^3 - \frac{60}{a^3}R^2 + \frac{120}{a^4}R - \frac{120}{a^5}\right)$$

$$< 6 >' = \int_{\frac{r_c}{r_m}}^{\infty} x^6 \exp[a(1-x)]dx = -\frac{1}{a}\left\{-\left(\frac{r_c}{r_m}\right)^6 \exp\left[a\left(1-\frac{r_c}{r_m}\right)\right]+6<5>'\right\} =$$

(A1.26)

$$Q\left(R^6 - \frac{6}{a}R^5 + \frac{30}{a^2}R^4 - \frac{120}{a^3}R^3 + \frac{360}{a^4}R^2 - \frac{720}{a^5}R + \frac{720}{a^6}\right)$$

$$< 7 >' = \int_{\frac{r_c}{r_m}}^{\infty} x^7 \exp[a(1-x)] dx = -\frac{1}{a} \left\{ -\left(\frac{r_c}{r_m}\right)^7 \exp\left[a\left(1-\frac{r_c}{r_m}\right)\right] + 7 < 6 >' \right\} =$$

. (A1.27)

$$Q\left(R^7 - \frac{7}{a} R^6 + \frac{42}{a^2} R^5 - \frac{210}{a^3} R^4 + \frac{840}{a^4} R^3 + \frac{2520}{a^5} R^2 + \frac{5040}{a^6} R + \frac{5040}{a^7} \right)$$

Using these integrals, Eq. (A1.4) can be solved:

$$\begin{cases} I_0 = A_0 < 2 >' \\ I_1 = A_1(< 3 >' - < 2 >') \\ I_2 = A_2(< 4 >' - 2 < 3 >' + < 2 >') \\ I_3 = A_3(< 5 >' - 3 < 4 >' + 3 < 3 >' - < 2 >') \\ I_4 = A_4(< 6 >' - 4 < 5 >' + 6 < 4 >' - 4 < 3 >' + < 2 >') \\ I_5 = A_5(< 7 >' - 5 < 6 >' + 10 < 5 >' - 10 < 4 >' + 5 < 3 >' - < 2 >') \end{cases}$$

. (A1.28)

Consider now the rest of the terms in Eq. (A1.3):

$$\int_{\frac{r_c}{r_m}}^{\infty} \sum_{j=0}^{2} \frac{C_{2j+6}}{d + x^{2j+6}} x^2 dx = -\int_{\frac{r_c}{r_m}}^{\infty} \frac{C_6}{d + x^6} x^2 dx - \int_{\frac{r_c}{r_m}}^{\infty} \frac{C_8}{d + x^8} x^2 dx - \int_{\frac{r_c}{r_m}}^{\infty} \frac{C_{10}}{d + x^{10}} x^2 dx =$$

(A1.29)

$$-\{J_6 + J_8 + J_{10}\}$$

where:

$$J_6 = C_6 \int_{\frac{r_c}{r_m}}^{\infty} \frac{x^2}{d + x^6} dx = C_6 \left\{ \frac{1}{3\sqrt{d}} arctg\left(\frac{x^3}{\sqrt{d}}\right) \Big|_{\frac{r_c}{r_m}}^{\infty} \right\} = C_6 \left\{ \frac{1}{3\sqrt{d}} \frac{p}{2} - \frac{1}{3\sqrt{d}} arctg\left(\frac{\left(\frac{r_c}{r_m}\right)^3}{\sqrt{d}}\right) \right\} .$$

(A1.30)

for J_8 and J_{10} an approximation has to be used. Since $\boldsymbol{d} = 0.01$ and $x = \dfrac{r}{r_m} > 0.9$

(practically always), we can infer that $x^8 >> \boldsymbol{d}$ and $x^{10} >> \boldsymbol{d}$ so it is possible to write:

$$J_8 = C_8 \int_{\frac{r_c}{r_m}}^{\infty} \frac{x^2}{\boldsymbol{d} + x^8} dx \approx C_8 \int_{\frac{r_c}{r_m}}^{\infty} \frac{1}{x^6} dx = C_8 \left\{ -\frac{1}{5} \frac{1}{x^5} \Big|_{\frac{r_c}{r_m}}^{\infty} \right\} = C_8 \left\{ \frac{1}{5} \frac{1}{\left(\frac{r_c}{r_m}\right)^5} \right\} \qquad \text{(A1.31)}$$

$$J_{10} = C_{10} \int_{\frac{r_c}{r_m}}^{\infty} \frac{x^2}{\boldsymbol{d} + x^{10}} dx \approx C_{10} \int_{\frac{r_c}{r_m}}^{\infty} \frac{1}{x^8} dx = C_{10} \left\{ -\frac{1}{7} \frac{1}{x^7} \Big|_{\frac{r_c}{r_m}}^{\infty} \right\} = C_{10} \left\{ \frac{1}{7} \frac{1}{\left(\frac{r_c}{r_m}\right)^7} \right\} . \qquad \text{(A1.32)}$$

Using the integrals calculated, we can finally write:

$$E_{lrc}^{2b} = 2\boldsymbol{p} N \boldsymbol{r} \, r_m^3 \boldsymbol{e} \left[\sum_{i=0}^{5} I_i - \sum_{j=0}^{2} J_{2j+6} \right]$$

For the pressure we have the expression (see Eq. (2.101)):

$$P_{lrc}^{2b} = -\frac{2\boldsymbol{p}\boldsymbol{r}^2}{3} \int_{r_c}^{\infty} \frac{du^{2b}}{dr} r^3 dr = -\frac{2\boldsymbol{p}\boldsymbol{r}^2}{3} r_m^3 \int_{\frac{r_c}{r_m}}^{\infty} x^3 \left(\frac{du^{2b}(x)}{dx} \right) dx . \qquad \text{(A1.33)}$$

Considering the formula for integration by part:

$$\int_{a}^{b} f(x) g'(x) dx = f(x) g(x) \Big|_{a}^{b} - \int_{a}^{b} f'(x) g(x) dx \qquad \text{(A1.34)}$$

we can write:

$$I = \int\limits_{\frac{r_c}{r_m}}^{\infty} x^3 \left(\frac{du^{2b}(x)}{dx} \right) dx = x^3 u^{2b}(x) \Big|_{\frac{r_c}{r_m}}^{\infty} - 3 \int\limits_{\frac{r_c}{r_m}}^{\infty} x^2 u^{2b}(x) dx =$$

$$- \left(\frac{r_c}{r_m} \right)^3 e \left\{ \sum_{i=0}^{5} A_i \left(\frac{r_c}{r_m} - 1 \right)^i \exp\left[a\left(1 - \frac{r_c}{r_m}\right) \right] - \sum_{j=0}^{2} \frac{C_{2j+6}}{d + \left(\frac{r_c}{r_m} \right)^{2j+6}} \right\} \qquad (A1.35)$$

$$- 3e \left[\sum_{i=0}^{5} I_i - \sum_{j=0}^{2} J_{2j+6} \right]$$

thus,

$$P_{lrc}^{2b} = -\frac{2pr^2}{3} r_m^3 I \quad . \qquad (A1.36)$$

Appendix 2

Three-Body Potential Molecular Simulation Implementation

In this appendix we report an easy and correct way to implement the 3-body potential (namely, the Axillord-Teller potential [Axi43]) in a molecular dynamics and Monte Carlo computer simulation program.

In the first section we show how to verify Newton's third law of dynamics with the 3-body potential, since in this way we are able to find useful expressions. In the second section we point out the problem arising using the minimum image convention with the 3-body potential, suggesting also the correct method to avoid mistakes. In the third section we write the expressions for the forces and the pressure, and in the last section we implement these expressions in an algorithm optimized for vector computers and designed to be fast enough to make the simulations feasible.

A2.1 Newton's third law of dynamics for 3-body potential

Considering three atoms i, j and k the 3-body Axilrod-Teller potential is (see Chapter 2):

$$u_{ijk} = \frac{v\left(1 + 3\cos\boldsymbol{q}_i \cos\boldsymbol{q}_j \cos\boldsymbol{q}_k\right)}{\left(r_{ij} r_{ik} r_{jk}\right)^3} \tag{A2.1}$$

where v_{DDD} is a non-additive coefficient and where the angles and intermolecular separations

$$r_{ij}^2 = \left(x_i - x_j\right)^2 + \left(y_i - y_j\right)^2 + \left(z_i - z_j\right)^2 \qquad (A2.2)$$

refer to a triangular configuration of atoms (see Figure 2.1). Using the cosine law:

$$r_{ij}^2 = r_{ik}^2 + r_{jk}^2 - 2r_{ik}r_{jk}\cos\boldsymbol{a} \qquad \rightarrow \qquad \cos\boldsymbol{a} = \frac{-r_{ij}^2 + r_{ik}^2 + r_{jk}^2}{2r_{ik}r_{jk}} \qquad (A2.3)$$

the potential in eq (A2.1)can be written as:

$$u_{ijk} = v\left[\frac{1}{r_{ij}^3 r_{ik}^3 r_{jk}^3} + \frac{3\left(-r_{ij}^2 + r_{ik}^2 + r_{jk}^2\right)\left(r_{ij}^2 - r_{ik}^2 + r_{jk}^2\right)\left(r_{ij}^2 + r_{ik}^2 - r_{jk}^2\right)}{8r_{ij}^5 r_{ik}^5 r_{jk}^5}\right] \qquad . \qquad (A2.4)$$

Expressing the potential as a function of the relative coordinates:

$$u\left(x_i; x_j; x_k; y_i; ....\right) = u\left(x_i - x_j; x_i - x_k; x_j - x_k; y_i - y_j; ...\right) = u\left(x_{ij}; x_{ik}; x_{jk}; y_{ij}; ....\right) \quad (A2.5)$$

the derivatives in the coordinates are easily obtained by:

$$F_{i(jk)}^{3b;x} \equiv -\frac{\partial u_{ijk}}{\partial x_i} = -\left[\frac{\partial x_{ij}}{\partial x_i}\frac{\partial u_{ijk}}{\partial x_{ij}} + \frac{\partial x_{ik}}{\partial x_i}\frac{\partial u_{ijk}}{\partial x_{ik}}\right] = -\left[\frac{\partial u_{ijk}}{\partial x_{ij}} + \frac{\partial u_{ijk}}{\partial x_{ik}}\right] = F_{i(j)k}^{3b;x} + F_{i(k)j}^{3b;x}. \quad (A2.6)$$

Here $F_{i(jk)}^{3b;x}$ is the total 3-body force (due to atoms j and k) on atom i in the x direction,

$F_{i(j)k}^{3b;x}$ is the contribution from atom j only. There are similar expressions for the other

coordinates:

$$\left.\begin{array}{l} F_{j(ik)}^{3b;x} \equiv -\dfrac{\partial u_{ijk}}{\partial x_j} = -\left[\dfrac{\partial x_{ij}}{\partial x_j}\dfrac{\partial u_{ijk}}{\partial x_{ij}} + \dfrac{\partial x_{jk}}{\partial x_j}\dfrac{\partial u_{ijk}}{\partial x_{jk}}\right] = -\left[-\dfrac{\partial u_{ijk}}{\partial x_{ij}} + \dfrac{\partial u_{ijk}}{\partial x_{jk}}\right] = \\[4mm] F_{j(i)k}^{3b;x} + F_{j(k)i}^{3b;x} = -F_{i(j)k}^{3b;x} + F_{j(k)i}^{3b;x} \end{array}\right\} \qquad (A2.7)$$

$$\left.\begin{array}{l} F_{k(ij)}^{3b;x} \equiv -\dfrac{\partial u_{ijk}}{\partial x_k} = -\left[\dfrac{\partial x_{ik}}{\partial x_k} \dfrac{\partial u_{ijk}}{\partial x_{ik}} + \dfrac{\partial x_{jk}}{\partial x_k} \dfrac{\partial u_{ijk}}{\partial x_{jk}} \right] = -\left[-\dfrac{\partial u_{ijk}}{\partial x_{ik}} - \dfrac{\partial u_{ijk}}{\partial x_{jk}} \right] = \\[4mm] F_{k(i)j}^{3b;x} + F_{k(j)i}^{3b;x} = -F_{i(k)j}^{3b;x} - F_{j(k)i}^{3b;x} \end{array}\right\} \quad . \qquad \text{(A2.8)}$$

Using the previous relationships, it is possible to show that the total forces on the atoms

i and j are equal and opposite to the total force on the atom k.

$$F_{i(jk)}^{3b;x} + F_{j(ik)}^{3b;x} = F_{i(j)k}^{3b;x} + F_{i(k)j}^{3b;x} + F_{j(i)k}^{3b;x} + F_{j(k)i}^{3b;x} = F_{i(k)j}^{3b;x} + F_{j(k)i}^{3b;x} = -F_{k(ij)}^{3b;x} \quad . \qquad \text{(A2.9)}$$

We point out that to obtain the previous result we have only used the fact that the 3-

body potential is a function of the relative distances between the three atoms.

A2.2 Three-body potential and minimum image convention

Given a triplet of atoms, applying the minimum image convention requires some

care. In general the minimum image convention does not keep the 'shape' of the

triangle. Let us analyze the *ijk* triplet in the following picture:
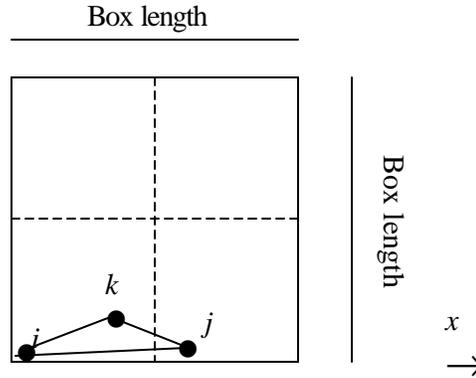
When we apply the minimum image convention on the length *ij*, we have to consider

the imagine of *j* (*j'*), because $(x_i - x_j)$ is longer than half the box length; so we consider

the side $\overline{ij'}$.
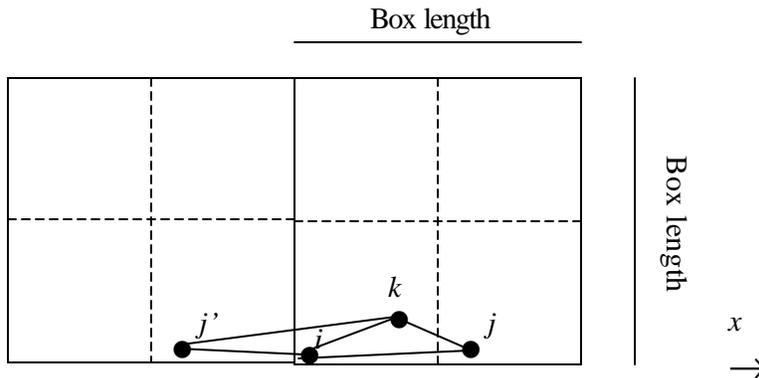
In the case of the side $\overline{ik}$, we do not have to consider the images because $(x_i - x_k)$ is not longer than half the box length. So the triangle now should be $ij'k$, but when we consider the atoms j and k, we have to calculate the side $\overline{jk}$ and not $\overline{kj'}$. So we have a "triangle" with the shape:
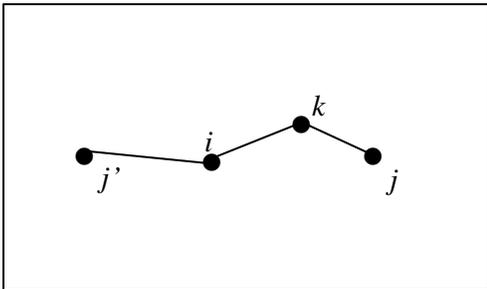
Using a cut-off for the 3-body potential for which a triangle is accepted if each side is less than a quarter of the box length, avoids these undesirable situations. Even if this condition is very strict, we have tested that for simulations at liquid densities with 500 argon atoms, the relative cut-off guarantees a good accuracy for the Axillord-Teller potential ([Mar99], see also Chapter 3). It is worthwhile to point out that the condition for the cut-off works also with Lees-Edwards sliding brick boundary conditions ([Eva90], see also Chapter 2).

In his work [Att92] Attard recognized this problem, but suggested a different solution. He implemented a different minimum image algorithm to be applied only for triplets of atoms and he adopted a cut-off for the three-body potential smaller than half the box length, as is the case for the two-body potential. Even if this mathematically solves the problem, we can not attribute to it a clear physical meaning. In the case depicted in the first figure, all the pair interactions between the three atoms are calculated, since all the three sides are less than half of the box length, according to the traditional minimum image convention. On the other hand, when Attard's algorithm is applied to calculate the three-body interactions, the same triplet of atoms is rejected, since $\overline{jk}$ is greater than half the box length. Furthermore, it is not clear if Attard's algorithm can be generalized for Lees-Edwards sliding brick boundary conditions.

Sometimes, a misleading condition for the three-body potential cut-off is adopted [Cor00]. The three-body force on atom i is considered different from zero if and only if both atoms j and k lie within the cut-off distance to atom i. No additional requirement is made on the distance between atoms j and k. This leads to non-symmetric situations. Let us consider the case where the distances between i and j and i and k are less than the cut-off, and the distance between j and k is greater than the cut-off. The three-body force on atom i is not zero. For atoms j and k the three-body force is zero. This clearly violates Newton's third law of dynamics, as expressed in Eq. (A2.9), since the total three-body force on the triplet of atoms is not zero.

A2.3 Forces and pressure for 3-body potential

In general, the $\boldsymbol{ab}$ ($\boldsymbol{a},\boldsymbol{b} = x,y,z$) component of the configurational pressure tensor is usually defined by [Ala87]:

$$P_{ab}V = \sum_i \mathbf{a}_i F_i^{\mathbf{b}} = -\sum_i \mathbf{a}_i \frac{\partial u_{tot}}{\partial \mathbf{b}_i} \qquad \text{(A2.10)}$$

Considering for simplicity the *xx* component, it is possible to write:

$$\sum_i x_i F_i^x = \sum_i \sum_{j>i} x_{ij} F_{ij}^x \qquad \text{(A2.11)}$$

where:

$$\left. \begin{array}{l} x_{ij} = x_i - x_j \\[2mm] F_{ij}^x = -\dfrac{\partial u_{ij}}{\partial x_{ij}} \end{array} \right\} \qquad \text{(A2.12)}$$

The left-hand-side of Eq. (A2.11) is not suitable to be used with the minimum image convention, since in general it changes the value of x_{ij}; we are forced to work with the second term of the relation (A2.11) [All87], i.e. with expressions which contain r_{ij} rather than r_i. In particular we also have to do this with the 3-body potential.

A similar relation holds for the 3-body case:

$$P_{xx}^{3b}V = \sum_i x_i F_i^{3b;x} = \sum_i \sum_{j \neq i} \sum_{k \neq j} x_i F_{i(jk)}^{3b;x} \qquad . \qquad \text{(A2.13)}$$

We can also write:

$$\sum_i x_i F_i^{3b;x} = \frac{1}{3} \sum_i \sum_{j \neq i} \sum_{k \neq j} \left(x_i F_{i(jk)}^{3b;x} + x_j F_{j(ik)}^{3b;x} + x_k F_{k(ij)}^{3b;x} \right) \qquad \text{(A2.14)}$$

since the indices i,j,k are equivalent.

Furthermore,

$$\sum_i x_i F_i^{3b;x} = \frac{1}{3} \sum_i \sum_{j \neq i} \sum_{k \neq j} \left\{ x_i \left[F_{i(j)k}^{3b;x} + F_{i(k)j}^{3b;x} \right] + \\ x_j \left[F_{j(i)k}^{3b;x} + F_{j(k)i}^{3b;x} \right] + x_k \left[F_{k(i)j}^{3b;x} + F_{k(j)i}^{3b;x} \right] \right\}$$
(A2.15)

Here we write $F_{i(jk)}^{3b;x} = F_{i(j)k}^{3b;x} + F_{i(k)j}^{3b;x}$, and similarly for the other triplet terms.

Substituting Eqs. (A2.7) and (A2.8) in Eq. (A2.15) gives:

$$\sum_i x_i F_i^{3b;x} = \frac{1}{3} \sum_i \sum_{j \neq i} \sum_{k \neq j} \left\{ x_i \left[F_{i(j)k}^{3b;x} + F_{i(k)j}^{3b;x} \right] + \\ x_j \left[- F_{i(j)k}^{3b;x} + F_{j(k)i}^{3b;x} \right] + x_k \left[- F_{i(k)j}^{3b;x} - F_{j(k)i}^{3b;x} \right] \right\}$$
(A2.16)

So:

$$\sum_i x_i F_i^{3b;x} = \frac{1}{3} \sum_i \sum_{j \neq i} \sum_{k \neq j} \left[(x_i - x_j) F_{i(j)k}^{3b;x} + (x_i - x_k) F_{i(k)j}^{3b;x} + (x_j - x_k) F_{j(k)i}^{3b;x} \right]$$ (A2.17)

or:

$$\sum_i x_i F_i^{3b;x} = \frac{1}{3} \sum_i \sum_{j \neq i} \sum_{k \neq j} \left(x_{ij} F_{i(j)k}^{3b;x} + x_{ik} F_{i(k)j}^{3b;x} + x_{jk} F_{j(k)i}^{3b;x} \right) = \\ \sum_i \sum_{j > i} \sum_{k > j} \left(x_{ij} F_{i(j)k}^{3b;x} + x_{ik} F_{i(k)j}^{3b;x} + x_{jk} F_{j(k)i}^{3b;x} \right)$$
(A2.18)

Since $F_{i(j)k}^{3b;x} = -\dfrac{\partial u_{ijk}}{\partial x_{ij}}$ (and similarly for all the other terms), we achieve the goal of

expressing the pressure as a function of pair distances. Now we need to find an

expression for $\dfrac{\partial u_{ijk}}{\partial x_{ij}}$. The potential is:

$$u_{ijk} = v\left[\frac{1}{r_{ij}^3 r_{ik}^3 r_{jk}^3} + \frac{3\left(-r_{ij}^2 + r_{ik}^2 + r_{jk}^2\right)\left(r_{ij}^2 - r_{ik}^2 + r_{jk}^2\right)\left(r_{ij}^2 + r_{ik}^2 - r_{jk}^2\right)}{8 r_{ij}^5 r_{ik}^5 r_{jk}^5}\right] =$$

$$\boldsymbol{n}\left[\frac{1}{r_{ij}^3 r_{ik}^3 r_{jk}^3} + \right.$$

$$\left. 3\frac{-r_{ij}^6 - r_{ik}^6 - r_{jk}^6 + r_{ij}^4 r_{ik}^2 + r_{ij}^4 r_{jk}^2 + r_{ij}^2 r_{ik}^4 + r_{ij}^2 r_{jk}^4 + r_{ik}^4 r_{jk}^2 + r_{ik}^2 r_{jk}^4 - 2 r_{ij}^2 r_{ik}^2 r_{jk}^2}{8 r_{ij}^5 r_{ik}^5 r_{jk}^5}\right]$$

. (A2.19)

So:

$$\frac{\partial u_{ijk}}{\partial x_{ij}} = \frac{\partial r_{ij}}{\partial x_{ij}}\frac{\partial u_{ijk}}{\partial r_{ij}} = \frac{x_{ij}}{r_{ij}}\frac{\partial u_{ijk}}{\partial r_{ij}} = \frac{x_{ij}}{r_{ij}} v\left[\frac{-3}{r_{ij}^4 r_{ik}^3 r_{jk}^3} - \frac{3}{8 r_{ik}^5 r_{jk}^5} + 3\frac{5 r_{ik}}{8 r_{ij}^6 r_{jk}^5} + \right.$$

$$3\frac{5 r_{jk}}{8 r_{ij}^6 r_{ik}^5} - \frac{3}{8 r_{ij}^2 r_{ik}^3 r_{jk}^5} - \frac{3}{8 r_{ij}^2 r_{ik}^5 r_{jk}^3}$$

$$\left. -3\frac{3}{8 r_{ij}^4 r_{ik} r_{jk}^5} - 3\frac{3}{8 r_{ij}^4 r_{ik}^5 r_{jk}} - 3\frac{5}{8 r_{ij}^6 r_{ik} r_{jk}^3} - 3\frac{5}{8 r_{ij}^6 r_{ik}^3 r_{jk}} + 3\frac{6}{8 r_{ij}^4 r_{ik}^3 r_{jk}^3}\right]$$

. (A2.20)

Similar expressions exist for all other derivatives of the triplet potential. This expression is 'easy' to implement in a program, as we report in the following section.

A2.4 Algorithm

In what follows we report an algorithm to implement the 3-body potential for a system of n atoms. We optimize the algorithm in order to take advantage of the vectorisation, hence this algorithm is not suitable for a parallel computer.

As a first step we have to calculate the distances between all the pair of atoms, and apply the minimum image convention (note that this loop in not time consuming in comparison with the 3-body algorithm):

loop *i* ← *1,N-1*
  loop *j* ← *i+1,N*

  // *coordAtomX(i)*, *coordAtomY(i)* and *coordAtomZ(i)* are the coordinates of atom *i*.
  // *distanceAtomsX*, *distanceAtomsY* and *distanceAtomsZ* are the distances between two
  // atoms in the *x*, *y*, *z* directions respectively.

  distanceAtomsX ← *coordAtomX(i) - coordAtomX(j)*
  distanceAtomsY ← *coordAtomY(i) - coordAtomY(j)*
  distanceAtomsZ ← *coordAtomZ(i) - coordAtomZ(j)*

  // Minimum image convention [All87]. *boxLength* is the box length. The
  // efficiency of different algorithms for the implementation of the minimum image
  // convention is studied in the work of Hloucha and Deiters [Hlo97].

  distanceAtomsX ← *distanceAtomsX - boxLength * NINT(distanceAtomsX / boxLength)*
  distanceAtomsY ← *distanceAtomsY - boxLength * NINT(distanceAtomsY / boxLength)*
  distanceAtomsZ ← *distanceAtomsZ - boxLength * NINT(distanceAtomsZ / boxLength)*

  // *distanceAtoms1(i,j), distanceAtoms2(i,j),…distanceAtoms6(i,j)* are arrays where the
  // distances between atoms (and their respective powers) are stored. These arrays
  // should be symmetrised, (*d(i,j)=d(j,i)*), but in what follows it is not necessary.

  distanceAtoms2(i,j) ← *distanceAtomsX**2 + distanceAtomsY**2 +*
    *distanceAtomsZ**2*
  distanceAtoms1(i,j) ← *SQRT(distanceAtoms2(i,j))*
  distanceAtoms3(i,j) ← *distanceAtoms2(i,j)*distanceAtoms1(i,j)*
  distanceAtoms4(i,j) ← *distanceAtoms2(i,j)*distanceAtoms2(i,j)*
  distanceAtoms5(i,j) ← *distanceAtoms2(i,j)*distanceAtoms3(i,j)*
  distanceAtoms6(i,j) ← *distanceAtoms2(i,j)*distanceAtoms4(i,j)*

  // *x(i,j),y(i,j)* and *z(i,j)* are arrays to store the relative distances in the *x*, *y*, *z* directions.

  x(i,j) ← *distanceAtomsX*
  y(i,j) ← *distanceAtomsY*
  z(i,j) ← *distanceAtomsZ*

  end *j* **loop**
end *i* **loop**

As usual, a double loop can be used at this stage to calculate the 2-body potential and forces:

loop *i ← 1,N-1*
 loop *j ← i+1,N*

  // Calculation of two-body potential and forces

  end *j* ***loop***
end *i* ***loop***

This loop is not time consuming in comparison with the 3-body algorithm; note that we do not use a neighbor list, since it could be complicated to implement with a 3-body potential and because it would probably compromise the vectorisation.

Before the algorithm for the 3-body terms is implemented, some variables have to be initialized:

// *total3BodyEnergy* is the total 3-body energy. *total3BodyForceX(i),*
// *total3BodyForceY(i), total3BodyForceZ(I)* are the total forces on the atom *i* in the *x,*
// *y, z* directions. *pressureTensor3body(1),….pressureTensor3body(6)* are the *xx, xy, xz,*
// *yy, yz, zz* elements of the 3-body pressure tensor. The hydrostatic pressure is 1/3 of the
// pressure tensor's trace.

total3BodyEnergy ←0.0
loop *i←1,N*

total3BodyForceX(i) ←0.0
total3BodyForceY(i) ←0.0
total3BodyForceZ(i) ←0.0

end *i* ***loop***

loop *i←1,6*

pressureTensor3body(i) ←0.0

end *i* ***loop***

Now we have to apply the cut-off condition to know which triplets of atoms

(triangles) can be counted. To do that we use the usual triple-loop:

> // *d1a(lc), d2a(lc),...d6a(lc)* are arrays to store the first side (and powers) of the
> // *lc*-th accepted triangle. *d1b(lc), d2b(lc),...d6b(lc)* are arrays to store the second
> // side (and powers) of the *lc*-th accepted triangle. *d1c(lc), d2c(lc),...d6c(lc)* are
> // arrays to store the third side (and powers) of the *lc*-th accepted triangle. *dXa(lc),*
> // *dYa(lc), dZa(lc)* are arrays to store the relatives coordinates of the first side of
> // the *lc*-th accepted triangle.

lc←0.0
loop *i←1,N-2*
  loop *j←i+1,N-1*
    loop *k←j+1,N*

  if *(distanceAtoms1(i,j) < boxLength/4 .and.*
     distanceAtoms1(i,k) < boxLength/4 .and.
     distanceAtoms1(j,k) < boxLength/4)

     // This is the cut-off condition: a triangle is accepted if each of its sides is less than
     // a quarter of the box length.

     lc ¬ lc+1
     d1a(lc) ←distanceAtoms1(i,j)
     d2a(lc) ←distanceAtoms2(i,j)
     d3a(lc) ←distanceAtoms3(i,j)
     d4a(lc) ←distanceAtoms4(i,j)
     d5a(lc) ←distanceAtoms5(i,j)
     d6a(lc) ←distanceAtoms6(i,j)

     dXa(lc) ←x(i,j)
     dYa(lc) ←y(i,j)
     dZa(lc) ←z(i,j)

     d1b(lc) ←distanceAtoms1(i,k)
     d2b(lc) ←distanceAtoms2(i,k)
     d3b(lc) ←distanceAtoms3(i,k)
     d4b(lc) ←distanceAtoms4(i,k)
     d5b(lc) ←distanceAtoms5(i,k)
     d6b(lc) ←distanceAtoms6(i,k)

     dXb(lc) ←x(i,k)
     dYb(lc) ←y(i,k)
     dZb(lc) ←z(i,k)

d1c(lc) ←*distanceAtoms1(j,k)*
d2c(lc) ←*distancetoms2(j,k)*
d3c(lc) ←*distanceAtoms3(j,k)*
d4c(lc) ←*distanceAtoms4(j,k)*
d5c(lc) ←*distanceAtoms5(j,k)*
d6c(lc) ←*distanceAtoms6(j,k)*

dXc(lc) ←*x(j,k)*
dYc(lc) ←*y(j,k)*
dZc(lc) ←*z(j,k)*

// *l1(lc), l2(lc), l3(lc)* are integer arrays to store the indices of the 3 atoms in the
// *lc*-th triangle; these arrays will be used to calculate the forces.

l1(lc) ←*i*
l2(lc) ←*j*
l3(lc) ←*k*

   end if

   end k loop
  end j loop
end i loop

The next loop will be a 'long' loop over the number of all accepted triangles to calculate energy, forces and pressure. This loop speeds up the program, since it can be vectorised more intensely than a normal triple loop.

loop l¬ 1,lc

// *dVdRa, dVdRb, dVdRc* are $\dfrac{\boldsymbol{n}}{r_{ij}}\dfrac{\partial u}{\partial r_{ij}}$, $\dfrac{\boldsymbol{n}}{r_{ik}}\dfrac{\partial u}{\partial r_{ik}}$, $\dfrac{\boldsymbol{n}}{r_{jk}}\dfrac{\partial u}{\partial r_{jk}}$ respectively (see section A2.3).
// *nonAdditiveCoef* is the non-additive coefficient *n*.

dVdRa ← (3.*nonAdditiveCoef/(8.*d1a(l)))*(
       -8./(d4a(l)*d3b(l)*d3c(l))-1./(d5b(l)*d5c(l))
       +5.*d1b(l)/(d6a(l)*d5c(l))+5.*d1c(l)/(d6a(l)*d5b(l))
       -1./(d2a(l)*d3b(l)*d5c(l))-1./(d2a(l)*d5b(l)*d3c(l))
       -3./(d4a(l)*d1b(l)*d5c(l))-3./(d4a(l)*d5b(l)*d1c(l))
       -5./(d6a(l)*d1b(l)*d3c(l))-5./(d6a(l)*d3b(l)*d1c(l))
       +6./(d4a(l)*d3b(l)*d3c(l)))

dVdRb ← (3.*nonAdditiveCoef/(8.*d1b(l)))*(
       -8./(d4b(l)*d3a(l)*d3c(l))-1./(d5a(l)*d5c(l))
       +5.*d1a(l)/(d6b(l)*d5c(l))+5.*d1c(l)/(d6b(l)*d5a(l))
       -1./(d2b(l)*d3a(l)*d5c(l))-1./(d2b(l)*d5a(l)*d3c(l))
       -3./(d4b(l)*d1a(l)*d5c(l))-3./(d4b(l)*d5a(l)*d1c(l))
       -5./(d6b(l)*d1a(l)*d3c(l))-5./(d6b(l)*d3a(l)*d1c(l))
       +6./(d4b(l)*d3a(l)*d3c(l)))

dVdRc ← (3.*nonAdditiveCoef/(8.*d1c(l)))*(
       -8./(d4c(l)*d3b(l)*d3a(l))-1./(d5b(l)*d5a(l))
       +5.*d1b(l)/(d6c(l)*d5a(l))+5.*d1a(l)/(d6c(l)*d5b(l))
       -1./(d2c(l)*d3b(l)*d5a(l))-1./(d2c(l)*d5b(l)*d3a(l))
       -3./(d4c(l)*d1b(l)*d5a(l))-3./(d4c(l)*d5b(l)*d1a(l))
       -5./(d6c(l)*d1b(l)*d3a(l))-5./(d6c(l)*d3b(l)*d1a(l))
       +6./(d4c(l)*d3b(l)*d3a(l)))

// This is the calculation of the forces:

// *total3BodyForceX(l1(l))* is the force on the atom *i* in the *X* direction.
// *total3BodyForceX(l2(l))* is the force on the atom *j* in the *X* direction.
// *total3BodyForceX(l3(l))* is the force on the atom *k* in the *X* direction.

total3BodyForceX(l1(l)) ←total3BodyForceX(l1(l))-dXa(l)*dVdRa -dXb(l)*dVdRb
total3BodyForceY(l1(l)) ←total3BodyForceY(l1(l))-dYa(l)*dVdRa -dYb(l)*dVdRb
total3BodyForceZ(l1(l)) ←total3BodyForceZ(l1(l))-dZa(l)*dVdRa -dZb(l)*dVdRb

total3BodyForceX(l2(l)) ←total3BodyForceX(l2(l))-dXa(l)*(-dVdRa)-dXc(l)*dVdRc
total3BodyForceY(l2(l)) ←total3BodyForceY(l2(l))-dYa(l)*(-dVdRa)-dYc(l)*dVdRc
total3BodyForceZ(l2(l)) ←total3BodyForceZ(l2(l))-dZa(l)*(-dVdRa)-dZc(l)*dVdRc

total3BodyForceX(l3(l)) ←total3BodyForceX(l3(l))-dXb(l)*(-dVdRb)-dXc(l)*(-dVdRc)
total3BodyForceY(l3(l)) ←total3BodyForceY(l3(l))-dYb(l)*(-dVdRb)-dYc(l)*(-dVdRc)
total3BodyForceZ(l3(l)) ←total3BodyForceZ(l3(l))-dZb(l)*(-dVdRb)-dZc(l)*(-dVdRc)

// Note, it is accumulating all the contributions of the same atom from all triangles
// where the atom is present).

// Calculation of the elements of the 3-body pressure tensor.

pressureTensor3body(1) ←pressureTensor3body (1)
     -dXa(l)*dXa(l)*dVdRa -dXb(l)*dXb(l)*dVdRb -dXc(l)*dXc(l)*dVdRc
pressureTensor3body(2) ←pressureTensor3body(2)
     -dXa(l)*dYa(l)*dVdRa -dXb(l)*dYb(l)*dVdRb -dXc(l)*dYc(l)*dVdRc
pressureTensor3body(3) ←pressureTensor3body(3)
     -dXa(l)*dZa(l)*dVdRa -dXb(l)*dZb(l)*dVdRb -dXc(l)*dZc(l)*dVdRc
pressureTensor3body(4) ←pressureTensor3body(4)
     -dYa(l)*dYa(l)*dVdRa -dYb(l)*dYb(l)*dVdRb -dYc(l)*dYc(l)*dVdRc
pressureTensor3body(5) ←pressureTensor3body(5)
     -dYa(l)*dZa(l)*dVdRa -dYb(l)*dZb(l)*dVdRb -dYc(l)*dZc(l)*dVdRc

pressureTensor3body(6) ←pressureTensor3body(6)
  -dZa(l)*dZa(l)*dVdRa -dZb(l)*dZb(l)*dVdRb -dZc(l)*dZc(l)*dVdRc

// Calculation of the 3-body energy.

total3BodyEnergy ←total3BodyEnergy+nonAdditiveCoef*(1.0/(d3c(l)*d3b(l)*d3a(l))
  +(3.0*(d2c(l)+d2b(l)-d2a(l))*(d2c(l)-d2b(l)+d2a(l))
  *(-d2c(l)+d2b(l)+d2a(l))/(8.*d5c(l)*d5b(l)*d5a(l))))

end l loop

To check the validity of the previous calculations it is worthwhile to verify the relationship:

$$\frac{3u_{tot}^{3b}}{V} = \frac{1}{3}\left(P_{xx}^{3b} + P_{yy}^{3b} + P_{zz}^{3b} \right)$$
(A2.21)

which holds since the Axilrod-Teller potential is a homogenous function of degree -9 in the variables r_{ij}, r_{ik} and r_{jk} [Bar71]. We did this test to check our program, and Eq. (A2.21) turned out to be verified.

Using a NEC SX-4 supercomputer we found that this algorithm used for molecular dynamics simulations with 500 particles makes the program 10 times faster than a program using normal triple-loops.

References

[Agr95]   Agrawal R. and Kofke D. A. (1995), *Thermodynamic and structural properties of model systems at solid-fluid coexistence: II. Melting and sublimation of the Lennard-Jones system*, Mol. Phys. **85**, 43-59.

[All87]   Allen M. P. and Tildesley D. J. (1987), *Computer simulation of liquids*; Clarendon: Oxford.

[All93]   Allen M. P. and Tildesley D. J. (1993), *Computer simulation in chemical physics*, NATO ASI Ser. C **397**; Kluwer: Dordrecht.

[Ant97]   Anta J. A., Lomba E. and Lombardero M. (1997), *Influence of three-body forces on the gas-liquid coexisting of simple fluids: the phase equilibrium of argon*, Phys. Rev. E **55**, 2707-2712.

[Ash73]   Ashurst W. T. and Hoover W. G. (1973), *Argon shear viscosity via a Lennard-Jones Potential with equilibrium and nonequilibrium molecular dynamics*, Phys. Rev. Lett. **31**, 206-208.

[Ash75]   Ashurst W. T. and Hoover W. G. (1975), *Dense-fluid shear viscosity via nonequilibrium molecular dynamics*, Phys. Rev. A **11**, 658-678.

[Att92]   Attard P. (1992), *Simulation results for a fluid with the Axilrod-Teller triple dipole potential*, Phys. Rev. A **45**, 5649-5653.

[Axi43]   Axilrod B. M. and Teller E., J. (1943), *Interaction of the van der Waals type between three atoms*, Chem. Phys. **11**, 299-300.

[Axi51]   Axilrod B. M. (1951), *Triple-dipole interaction. I. Theory*, J. Chem. Phys. **19**, 719-724.

[Azi86]   Aziz R. A. and Slaman M. J. (1986), *The argon and krypton interatomic potentials revisited*, Mol. Phys. **58**, 679-697.

[Azi89]   Aziz R. A., Buck U., Jonsson H., Ruiz-Suarez J. C., Schmidt B., Scoles G., Slaman J. J. and Xu J. (1989), *Two- and three-body forces in the interaction of He atoms with Xe overlayers adsorbed on (0001) graphite*, J. Chem. Phys. **91**, 6477-6493.

[Azi93]   Aziz R. A. (1993), *A highly accurate interatomic potential for argon*, J. Chem. Phys. **99**, 4518-4524

[Azi95]   Aziz R. A., Janzen A. R. and Moldover M. R. (1995), *Ab initio calculations for helium: A standard for transport property measurements*, Phys. Rev. Lett. **74**, 1586-1589.

[Bad58]   Bade W. L. (1958), *Drude-model calculation of dispersion forces. III. The forth-order contribution*, J. Chem. Phys. **28**, 282-284.

[Bar68]   Barker J. A. and Pompe A. (1968), *Atomic interactions in argon*, Aust. J. Chem. **21**, 1683-1694.

[Bar71a]   Barker J. A., Fisher R. A. and Watts R. O., *Liquid argon: Monte Carlo and molecular dynamics calculations*, (1971), Mol. Phys. **21**, 657-673.

[Bar71b]   Barker J. A., Bobetic M. V. and Pompe A. (1971), *An experimental test of the Boltzamm equation: argon*, Mol. Phys. **20**, 347-355.

[Bar72a]   Barker J. A., Johnson C. H. J. and Spurling T. H. (1972), *On the cancellation of certain three- and four-body interactions in inert gases*, Aust. J. Chem. **25**, 1811-1812.

[Bar72b]   Barker J. A., Johnson C. H. J. and Spurling T. H. (1972), *Third virial coefficient for krypton*, Aust. J. Chem. **25**, 1813-1814.

[Bar74]   Barker J. A., Watts R. O., Lee J. K., Schafer T. P. and Lee Y. T. (1974), *interatomic potential for krypton and xenon*, J. Phys. Chem. **61**, 3081-3089.

[Bar76]   Barker J. A. (1976), *Interatomic potentials for inert gases from experimental data*, p. 212-264, in *Rare gas solids*, vol. 1, Klein M. L. and Venables J. A., (Eds); Academic: London.

[Bar95]   Baranyai A. and Cummings P. T. (1995), *On the molecular dynamics algorithm for Gibbs ensemble simulation*, Mol. Simul. **17**, 21-25.

[Bel70]   Bell R. J. (1970), *Multipolar expansion for the non-additive third-order interaction energy of three atoms*, J. Phys. B, **3**, 751-762.

[Bel76]   Bell R. J. and Zucker I. J. (1976), *Long-range forces*, p. 122-175, in *Rare gas solids*, vol.1, Klein M. L. and Venables J. A., (Eds); Academic: London.

[Bhu96]   Bhupathiraju R., Cummings P. T. and Cochran H. D. (1996), *An efficient parallel algorithm for non-equilibrium molecular dynamics simulations of very large systems in planar Couette flow*, Mol. Phys. **88**, 1665-1670.

[Bor54]   Born M. and Huang K. (1954), *Dynamical theory of crystal lattice*, Clarendon: Oxford.

[Bob70]   Bobetic V. and Barker J. A. (1970), *Lattice dynamics with three-body forces: argon*, Phys. Rev. B. **2**, 4169-4175.

[Bra83]   Bransden B. H. and Joachain C. J. (1983), *Physics of atoms and molecules*; Addison Wesley Longman: England

[Bru97]   Bruce A. D. (1997), *Finite-size critical behavior in the Gibbs ensemble*, Phys. Rev. E **55**, 2315-2320.

[Buk01]   Bukowsky R. and Szalewicz K. (2001), *Monte Carlo simulations for gaseous and liquid argon with complete ab initio nonadditive potential*, J. Chem. Phys. submitted.

[Cha88]   Chalasinsky G., Szczesniak M.M. (1988), *On the connection between the supermolecular Møller-Plesset treatment of the interaction energy and the perturbation theory of intermolecular forces*, Mol. Phys. **63**, 205-224.

[Cha90]   Chalasinsky G. Szczesniak M. M. and Cybulsky S. M. (1990), *Calculations of nonadditive effects by means of supermolecular Møller-Plesser perturbation theory approach: Ar_3 and Ar_4*, J. Chem. Phys. **92**, 2481-2487.

[Cic75]   Ciccotti G., Jacucci G. (1975), *Direct computation of dynamics response by molecular dynamics: the mobility of a charged Lennard-Jones particle*, Phys. Rev. Lett. **35**, 789-792.

[Cic76]   Ciccotti G., Jacucci G. and McDonald I. R. (1976), *Transport properties of molten alkali halides*, Phys. Rev. A **13**, 426-436.

[Cic79]   Ciccotti G., Jacucci G. and McDonald I. R. (1979), *"Thought-experiments" by molecular dynamics*, J. Stat. Phys. **21**, 1-22.

[Cop68]   Copeland D. A. and Kestener N. R. (1968), *Accurate "Effective" intermolecular pair potentials in gaseous argon*, J. Chem. Phys. **49**, 5214-5222.

[Cor00]   Cornwell C. F. and Wille L. T. (2000), *Parallel molecular dynamics simulations for short-ranged many-body potentials*, Computer Phys. Commun. **128**, 477-491.

[Cro65]   Cross M. M. (1965), *Rheology of non-Newtonian fluids: a new flow equation for pseudoplastic systems*, J. Colloid. Sci. **20**, 417-437.

[Dai92]   Daivis P. J. and Evans D. J. (1992), *Computer simulation study of the comparative rheology of branched and linear alkanes*, J. Chem. Phys. **97**, 616-627.

[Dei99]   Deiters U. K., Hlooucha M. and Leonhard K. (1999), *Chemical Thermodynamics*, 187-195, in *Chemistry for the 21st century*, Letcher T. M. Ed.; Blackwell Science: Oxford.

[Dob57]   Dobbs E. R. and Jones G. O. (1957), *Theory and properties of solid argon*, Rep. Progr. Phys. **20**, 516-564.

[Doi86]   Doi M. Edwards S. F. (1986), *The theory of polymer dynamics*; Clarendon: Oxford.

[Dor70]   Dorfman J. R. and Cohen E. G. D. (1970), *Velocity correlation functions in two and three dimensions*, Phys. Rev. Lett. **25**, 1257-1260.

[Dor71]   Doran M. B. and Zucker I. J. (1971), *Higher order multipole three-body van der Waals interactions and stability of rare gas solids*, J. Phys. C **4**, 307-312.

[Dor72]   Dorfman J. R. and Cohen E. G. D. (1972), *Velocity-correlation functions in two and three dimentions: low density*, Phys. Rev. A. **6**, 776-790.

[Dru96]   Drugowich de Felicio J. R. and Libero V. L. (1996), *Updating Monte Carlo algorithms*, Am. J. Phys. **64**, 1281-1285.

[Ege88]   Egelstaff P. A. (1988), *Experimental tests for many-body forces in noble gas fluids*, Can. J. Chem. **66**, 598-608.

[Ege94]   Egelstaff P. A. (1994), *An introduction to the liquid state*; Clarendon: Oxford.

[Elr94]   Elrod M. J. and Saykally R. J. (1994), *Many-body effects in intermolecular forces*, Chem. Rev. **94**, 1975-1997.

[Erm98]   Ermakova E., Solca J., Steinebrunner G. and Huber H. (1998), *Ab initio calculation of a three-body potential to be applied in simulations of fluid neon*, Chem.–Eur. J. **4**, 377-382.

[Erp84]   Erpenbeck J. J. (1984), *Shear viscosity of the hard-sphere fluid via nonequilibrium molecular dynamics*, Phys. Rev. Lett. **52**, 1333-1335.

[Ess95]   Esselink K., Loyens L. D. J. C. and Smit B. (1995), *Parallel Monte Carlo simulations*, Phys. Rev. E **51**, 1560-1568.

[Eva80]   Evans D.J. (1980), *Nonlinear viscous flow in two-dimensional systems*, Phys. Rev. A **22**, 290-294.

[Eva81]   Evans D.J. (1981), *Rheological properties of simple fluids by computer simulation*, Phys. Rev. A **23**, 1988-1997.

[Eva84a] Evans D. J. and Morris G. P. (1984), *Equilibrium time correlation functions under Gaussian isothermal dynamics*, Chem. Phys. **87**, 451-454.

[Eva84b] Evans D. J. and Morris G. P. (1984), *Non-Newtonian molecular dynamics*, Computer Phys. Reports **1**, 297-343.

[Eva84c] Evans D. J. and Morris G. P. (1984), *Nonlinear-response theory for steady planar Couette flow*, Phys. Rev. A **30**, 1528-1530.

[Eva86]   Evans D. J. and Morriss G. P. (1986), *Shear thickening and turbulence in simple fluids*, Phys. Rev. Lett. **56**, 2172-2175.

[Eva89]   Evans D. J., Morriss G. P. and Hood L. M. (1989), *On the number dependence of viscosity in three dimensional fluids*, Mol. Phys. **68**, 637-646.

[Eva90]   Evans D. J. and Morris G. P. (1990), *Statistical mechanics of nonequilibrium liquids*; Academic: London.

[Eva92]   Evans D. J., Cui S. T., Hanley H. J. M. and Straty G. C. (1992), *Conditions for the existence of a reentrant solid phase in a sheared atomic fluid*, Phys. Rev. A **46**, 6731-6735.

[Fer88]   Ferrenberg A. M. and Swendsen (1988), *New Monte Carlo technique for studying phase transitions*, Phys. Rev. Lett. **61**, 2635-2638.

[Fer89]   Ferrenberg A. M. and Swendsen (1989), *Optimized Monte Carlo data analysis*, Phys. Rev. Lett. **63**, 1195-1198.

[Fer91a]   Ferrario M., Ciccotti G., and Holian B. L. and J. P. Ryckaert J. P. (1991), *Shear-rate viscosity of the Lennard-Jones liquid at the triple point*, Phys. Rev. A **44**, 6936-6939.

[Fer91b]   Ferguson J. and Kemblowsky Z. (1991), *Applied fluid rheology*, Elsevier Science: New York.

[For98]   Formisano F., Barocchi F. and Magli R. (1998), *Long range interactions in xenon*, Phys. Rev. E **58**, 2648-2651.

[Fre96]   Frenkel D. and Smit B. (1996), *Understanding molecular simulation*; Academic: London.

[Gal93]   Galli G. and Pasquarello A. (1993), *First-principle molecular dynamics*, p. 261-313, in *Computer simulation in chemical physics*, Allen M. P. and Tildesley D. J. (Eds), NATO ASI Ser. C **397**; Kluwer: Dordrecht.

[Gea71]   Gear C. W. (1971), *Numerical initial value problems in ordinary differential equations*; Prentice Hall: London.

[GeJ01]   Ge J., Marcelli G. Todd B. D. and Sadus R. J. (2001), *Energy and pressure of shearing fluids at different state points*, Phys. Rev. Lett., submitted.

[Gos73]   Gosling E. M., McDonald I. R. and Singer K. (1973), *On the calculation by molecular dynamics of the shear viscosity of simple fluid*, Mol. Phys. **26**, 1475-1484.

[Gre52]   Green H. S. (1952), *The molecular theory of fluids*; North-Holland-Interscience.

[Gub89]   Gubbins K. E. (1989), *The role of the computer simulation in studying phase equilibria*, Mol. Simul. **2**, 223-252.

[Gub96]   Gubbins K. E. and Quirke N. (1996), *Molecular simulation and industrial applications. Methods, examples and prospects*; Gordon and Breach Science: Amsterdam.

[Gui89a]   Guillot B., Mountain R. D. and Birnbaum G. (1989), *Triple dipoles in the absorption spectra of dense rare gas mixtures. I. Short range interactions*, J. Chem. Phys. **90**, 650-6662.

[Gui89b]   Guillot B. (1989), *Triple dipoles in the absorption spectra of dense rare gas mixtures. II. Long range interactions*, J. Chem. Phys. **91**, 3456-3462.

[Han80]   Hanley H. J. and Evans D. J. (1980), *Equilibrium and non-equilibrium radial distribution functions in mixtures*, Mol. Phys. **39**, 1039-1042.

[Hey98]   Heyes D. M. (1998), *The liquid state. Applications of molecular simulations*; Wiley: Chichester.

[Hlo97]   Hloucha M. and Deiters U. K. (1997), *Fast coding of the minimum image convention*, Mol. Simul. **20**, 239-244.

[Hoh93]   Hoheisel C. (1993), *Theoretical treatment of liquids and liquid mixtures*; Elsevier: Amsterdam.

[Hoo80]   Hoover W. G., Evans D. J., Hickman R. B., Ladd A. J. C., Ashurst W. T. and Moran B. (1980), *Lennard-Jones triple-point bulk and shear viscosity. Green-Kubo theory, Hamiltonian mechanics, and nonequilibrium molecular dynamics*, Phys. Rev. A **22**, 1690-1697.

[Hoo85]   Hoover W. G. (1985), *Canonical dynamics: equilibrium phase-space distributions*, Phys. Rev. A **31**, 1695-1697.

[Hua63]   Huang K. (1963), *Statistical mechanics*; Wiley: New York.

[Irv50]   Irving J. H. and Kirkwood J. G. (1950), *The statistical mechanical theory of transport processes. IV. The equations of hydrodynamics*, J. Chem. Phys. **18**, 817-829.

[Jan62]   Jansen L. (1962), *Systematic analysis of many-body interactions in molecularc solids*, Phys. Rev. **125**, 1798-1804.

[Kaw73]   Kawasaki K. and Gunton J. D. (1973), *Theory of nonlinear transport processes: nonlinear shear viscosity and normal stress effects*, Phys. Rev. A **8**, 2048-2064

[Khi49]   Khinchin A. I. (1949), *Statistical mechanics*; Dover: New York.

[Kir98]   Kirchner B., Ermakova E., Solca J. and Huber H. (1998), *Chemical accuracy obtained in an ab initio molecular dynamics simulation of a fluid by inclusion of a three-body potential*, Chem.-Eur. J. **4**, 383-388.

[Kof93a]   Kofke D. A. (1993), *Gibbs-Duhem integration: a new method for direct evaluation of phase coexistence by molecular simulation*, Mol. Phys. **78**. 1331-13336.

[Kof93b]   Kofke D. A. (1993), *Direct evaluation of phase coexistence by molecular simulation via integration along the saturation line*, J. Chem. Phys. **98**, 4149-4162.

[Kof97]   Kofke D. A. and Cummings P. T. (1997), *Quantitative comparison and optimization of method for evaluating the chemical potential by molecular simulation*, Mol. Phys. **92**, 973-996.

[Kub57]   Kubo R. (1957), *Statistical-mechanical theory of irreversible processes. I. General theory and simple applications to magnetic and conduction problems*, J. Phys. Soc. Jpn. **12**, 570-596.

[Lee72]   Lees A. W. and Edwards S. F. (1972), *The computer study of transport processes under extreme conditions*, J. Phys. C **5**, 1921-1929.

[Lee93]   Lee S. H. and Cummings P. T. (1993), *Shear viscosity of model mixtures by nonequilibrium molecular dynamics. 1. Argon-krypton mixtures*, J. Chem. Phys. **99**, 3919-3925.

[Lee94]   Lee S. H. and Cummings P. T. (1994), *Effect of three-body forces on the shear viscosity of liquid argon*, J. Chem. Phys. **101**, 6206-6209.

[Leo00]   Leonhard K. and Deiters U. K. (2000), *Monte Carlo simulations of neon and argon using ab initio potentials*, Mol. Phys. **98**, 1603-1616.

[Leo75]   Leonard P. J. and Barker J. A. (1975), *Dipole oscillator strengths and related quantities for inert gases*, p. 117-136, in H. Eyring, and D. Henderson (Eds), *Theoretical Chemistry: Advances and Perspectives*, Vol. 1; Academic: London.

[LeS83]   LeSar R. (1983), *Ground- and excited-state properties of solid argon under pressure*, Phis. Rev. B **28**, 6812-6820.

[Lie92]   Liem S. Y., Brown D. and Clarke J. H. R. (1992), *Investigations of the homogeneous-shear nonequilibrium-molecular-dynamics method*, Phys. Rev. A **45**, 3706-3713.

[Lis96a]   Lisal M. and Vacek V. (1996), *Direct evaluation of vapour-liquid equilibria by molecular dynamics using Gibbs-Duhem integration*, Mol. Simul. **17**, 27-39.

[Lis96b]   Lisal M. and Vacek V. (1996), *Direct evaluation of vapour-liquid equilibria of mixtures by molecular dynamics using Gibbs-Duhem integration*, Mol. Simul. **19**, 75-99.

[Lot92]   Lotfi A., Vrabec J. and Fischer J. (1992), *Vapour liquid equilibria of the Lennard-Jones fluid from NPT plus test particle method*, Mol. Phys. **76**, 1319-1333.

[Lot97a]   Lotrich V. F. and Szalewicz K. (1997), *Three-body contribution to binding energy of solid argon and analysis of crystal structure*, Phys. Rev. Lett. **79**, 1301-1304.

[Lot97b]   Lotrich V. F. and Szalewicz K. (1997), *Symmetry-adapted perturbation theory of three-body nonadditivity in Ar trimer*, J. Chem. Phys. **106**, 9688-9702.

[Loy95]   Loyens L. D. J. C., Smit B. and Esselink K. (1995), *Parallel Gibbs-Ensemble simulations*, Mol. Phys. **86**, 171-183.

[Mai81]   Maitland G. C., Rigby M., Smith E. B. and Wakeham W. A. (1981), *Intermolecular forces, their origin and determination*; Clarendon: Oxford.

[Mar00]   Marcelli G. and Sadus R. J. (2000), *A link between the two-body and three-body interaction energies of fluids from molecular simulation*, J. Chem. Phys. **112**, 6382-6385.

[Mar01a]   Marcelli G. and Sadus R. J. (2001), *Three-body interactions and the phase equilibria of mixtures*, High Temp. -High Pressures **33**, 111-118.

[Mar01b]   Marcelli G., Todd B. D. and Sadus R. J. (2001), *Analytic dependence of the pressure and energy of an atomic fluid under shear*, Phys. Rev. E **63**, in press.

[Mar01c]   Marcelli G., Todd B. D. and Sadus R. J. (2001), *The strain rate dependence of shear viscosity, pressure and energy from two-body and three-body interactions*, Fluid Phase Equilib., in press.

[Mar01d]   Marcelli G., Todd B. D. and Sadus R. J. (2001), *On the relationship between two-body and three-body interactions from non-equilibrium molecular dynamics simulation*, J. Chem. Phys., submitted.

[Mar99]   Marcelli G. and Sadus R. J. (1999), *Molecular simulation of the phase behavior of noble gases using accurate two-body and three-body intermolecular potentials*, J. Chem. Phys. **111**, 1533-1540.

[Mat00]   Matin M. L., Daivis P. J. and Todd B. D. (2000), *Comparison of planar shear flow and planar elongational flow for systems of small molecules*, J. Chem. Phys. **113**, 9122-9131.

[McL88]   McLean A. D., Liu B. and Barker J. A. (1988), *Ab initio calculation of argon-argon potential*, J. Chem. Phys. **89**, 6339-6347.

[Mel93]   Melchionna S., Ciccotti G. and Holian B. L. (1993), *Hoover NPT dynamics for systems varying in shape and size*, Mol. Phys. **78**, 533-544.

[Mel94]   Melchionna S., Ciccotti G. and Holian B. L. (1994), *Comment on "Constant pressure molecular dynamics algorithms"*, J. Chem. Phys. **101**, 346-347.

[Met53]   Metropolis N., Rosenbluth A. W., Teller A. N. and Teller E. (1953), *Equation of state calculations by fast computing machines*, J. Chem. Phys. **21**, 1087-1092.

[Miy94]   Miyano Y. (1994), *An effective triplet potential for argon*, Fluid Phase Equil. **95**, 31-41.

[Möl90]   Möller D. and Fischer J. (1990), *Vapour liquid equilibrium of a pure fluid from test particle method with NPT molecular dynamics simulations*, Mol. Phys. **69**, 463-473.

[Mou94]   Mountain R. D. and Thirumalai D. (1994), *Quantitative measure of efficiency of Monte Carlo Simulations*, Physica A **210**, 453-460.

[Mur71]   Murphy R. D. and Barker J. A. (1971), *Three-body interactions in liquid and solid helium*, Phys. Rev. A **3**, 1037-1040.

[Mur76]   Murrell J. N. (1976), *Short and intermediate range forces*, p. 176-211, in *Rare gas solids*, vol.1, Klein M. L. and Venables J. A., (Eds); Accademic: London.

[Nie76]   Niebel K. F. and Venables J. A. (1976), *The crystal structure problem*, p. 558-589, in *Rare gas solids*, vol.1, Klein M. L. and Venables J. A., (Eds); Accademic: London.

[Pal94]   Palmer B. and Lo C. (1994), *Molecular dynamics implementation of the Gibbs ensemble calculation*, J. Chem. Phys. **101**, 10899-10907.

[Pan00]   Panagiotopoulos A. Z. (2000), *Monte Carlo methods for phase equilibria of fluids*, J. Phys.: Condens. Matter **12**, R25-R52

[Pan87]   Panagiotopoulus A. Z. (1987), *Direct determination of phase coexistence properties of fluids by Monte Carlo simulation in a new ensemble*, Mol. Phys. **61**, 813-826.

[Pan88]   Panagiotopoulus A. Z., Quirke N., Stapleton M. and Tildesley D. J. (1988), *Phase equilibria by simulation in the Gibbs ensemble. Alternative derivation, generalization and application to mixture and membrane equilibria*, Mol. Phys. **63**, 527-545.

[Pan94a]   Panagiotopoulos A. Z. (1994), *Molecular simulation of phase equilibria*, p. 411-437 in *Supercritical Fluids - Fundamentals for Application*, E. Kiran. and J. M. H. Levelt Sengers (Eds), NATO ASI Series E **273**; Kluwer: Dordrecht.

[Pan94b]   Panagiotopoulos A. Z. (1994), *Molecular simulation of phase coexistence: finite-size effects and determination of critical parameters for two- and three-dimensional Lennard-Jones fluids*, Int. J. Thermophys. **15**, 1057-1072.

[Pan95] Panagiotopoulos A. Z. (1995), *Gibbs ensemble techniques*, 463-501, in M. Baus, L.R. Rull and J.P. Ryckaert, *Observation, prediction and simulation of phase transitions in complex fluids*, NATO ASI Series C, **460**; Kluwer Academic: Dordrecht.

[Pan98] Panagiotopoulos A. Z., Wong V. and Floriano M. A. (1998), *Phase equilibria of lattice polymers from histogram reweighting Monte Carlo simulations*, Macromolecules **31**, 912-918.

[Pla97] Plackov D. and Sadus R. J. (1997), *Molecular simulation of intermolecular attraction and repulsion in coexisting liquid and vapour phases*, Fluid Phase Equilibria **134**, 77-85.

[Pot98] Potoff J. J. and Panagiotopoulos A. Z. (1998), *Critical point and phase behaviour of the pure fluid and a Lennard-Jones mixture*, J. Chem. Phys. **109**, 10914-10920.

[Pot99] Potoff J. J, Errington J. R. and Panagiotopoulos A. Z. (1999), *Molecular Simulation of Phase Equilibria for Mixtures of Polar and Non-Polar Components*, Mol. Phys. **97**, 1073-83.

[Pry66] Pryde J. A. (1966), *The liquid state*; Hutchinson: London.

[Que82] Quentrec B. (1982), *Dependence de la viscosite' en fonction du taux de cisaillement dans un fluide Lennard-Jones* , Mol. Phys. **46**, 707-714.

[Qui01] Quirke N. (2001), *Molecular modelling and simulation: tools for the modern era* , Mol. Simul. **26**, 1-31.

[Rec93] Recht J. R. and Panagiotopoulus A. Z. (1993), *Finite effects and approach to criticality in Gibbs ensemble simulations*, Mol. Phys. **80**, 843-852.

[Rit90] Rittger E. (1990), *An empirical three-body potential for xenon* , Mol. Phys. **71**, 79-96.

[Row82] Rowlinson J. S. and Widom B. (1982), *Molecular theory of capillarity* ; Calarendon: Oxford.

[Ryc88] Ryckaert J. P., Bellemans A., Ciccotti G. and Paolini G.V. (1988), *Shear-rate dependence of the viscosity of simple fluids by nonequilibrium molecular dynamics* , Phys. Rev. Lett. **60**, 128-131.

[Sad95] Sadus R. J. (1995), *Equations of state for hard-sphere chains*, J. Phys. Chem. **99**, 12363-12366.

[Sad96a] Sadus R. J. (1996), *Molecular simulation of the vapour-liquid equilibria of pure fluids and binary mixtures containing dipolar components: the effect of Keesom interactions*, Mol. Phys. **87**, 979-990.

[Sad96b]   Sadus R. J. and Prausnitz J. M. (1996), *Three-body interactions in fluids from molecular simulation: vapor-liquid coexistence of argon*, J. Chem. Phys. **104**, 4784-4787.

[Sad98a]   Sadus R. J. (1998), *Exact calculation of the effect of three-body Axilrod-Teller interactions on vapour-liquid phase coexistence*, Fluid Phase Equilibria **144,** 351-360.

[Sad98b]   Sadus R. J. (1998), *The effect of three-body interactions on the liquid-liquid phase coexistence of binary fluid mixtures*, Fluid Phase Equilibria **150-151**, 63-72.

[Sad98c]   Sadus R. J. (1998), *Effect of three-body interactions between dissimilar molecules on the phase behaviour of binary mixtures: the transition from vapor-liquid equilibria to type III behaviour*, Ind. Eng. Chem. Res. **37**, 2977-2982.

[Sad99]   Sadus R. J. (1999), *Molecular simulation of fluids: Theory, algorithms and object-orientation*; Elsevier: Amsterdam.

[San94]   Sandler S. I. (1994), *Equations of state for phase equilibrium computations*, p. 147-175 in *Supercritical Fluids - Fundamentals for Application*, E. Kiran. and J. M. H. Levelt Sengers (Eds), NATO ASI Series E **273**; Kluwer: Dordrecht.

[Sar98]   Sarman S. S., Evans D. J. and Cummings P. T. (1998), *Recent developments in non-Newtonian molecular dynamics*, Phys. Rep. **305**, 1-92.

[Sch75]   Schouten J. A., Deerenberg A. Trappeniers N. J. (1975), *Vapour-liquid and gas-gas equilibria in simple systems*, Physica A **81**, 151-160.

[Sea75]   Sear F. W. and Salinger G. L. (1975), *Thermodynamics, kinetic theory and statistical thermodynamics*; Addison-Wesley: Massachusetts.

[She66]   Sherwood A. E., de Rocco A. G. and Mason E. A. (1966), Nonadditivity of *intermolecular potential forces: effects on the third virial coefficient*, J. Chem. Phys. **44**, 2984-2994.

[Sie93]   Siepmann J. I., Karaborni S. and Smit B. (1993), *Simulating the critical behaviour of complex fluids*, Nature **365**, 330-332.

[Smi89a]   Smit B., De Smedt P. and Frenkel D. (1989), *Computer simulations in the Gibbs ensemble*, Mol. Phys. **68**, 931-950.

[Smi89b]   Smit B. and Frenkel D. (1989), *Calculation of the chemical potential in the Gibbs ensemble*, Mol. Phys. **68**, 951-958.

[Smi92]   Smit B., Hauschild T. and Prausnitz J. M. (1992), *Effect of a density-dependent potential on phase behavior of fluid*, Mol. Phys. **77**, 1021-1031.

[Smi95]   Smit B., Karaborni S. and Siepmann J. I. (1995), *Computer simulations of vapor–liquid phase equilibria of n-alkanes*, J. Chem. Phys. **102**, 2126-2140.

[Ste94]   Stenschke H. (1994), *Effective Axilrod-Teller interaction in van der Waals gases and liquids*, J. Chem Phys. **100**, 4704-4705.

[Str00]   Strnad M. and Nezbeda I. (2000), *Parallelized sampling of the Gibbs ensemble*, Mol. Phys. **98**, 1887-1894.

[Szc92]   Szczesniak M.M. and Chalasinsky G. (1992), *Ab initio calculations of nonadditive effects*, J. Mol. Struct. (*Theochem*) **261**, 37-54.

[Tan70]   Tanaka Y. and Yoshino K. (1970), *Absorption spectrum of the argon molecule in the vacuum-uv region*, J. Chem. Phys. **53**, 2012-2030.

[Ten82]   Tenenbaum A., Ciccotti G. and Gallico Renato (1982), *Stationary nonequilibrium states by molecular dynamics. Fourier's law*, Phys. Rev. A **25**, 2778-2787.

[Tod95]   Todd B. D., Evans D. J. and Daivis P. J. (1995), *Pressure tensor for inhomogeneous fluids*, Phys. Rev. E **52**, 1627-1638.

[Tod97]   Todd B. D. (1997), *Application of transient-time correlation functions to nonequilibrium molecular-dynamics simulations of elongational flow*, Phys. Rev. E **56**, 6723-6728.

[Tod99]   Todd B. D. and Daivis P. J. (1999), *A new algorithm for unrestricted duration nonequilibrium molecular dynamics simulations of planar elongational flow*, Comp. Phys. Comm. **117**, 191-199.

[Tra98]   Travis K. P., Searles D. J. and Evans D. J. (1998), *Strain-rate dependent properties of a simple fluid*, Mol. Phys. **95**, 195-202.

[Tro84]   Trozzi C. and Ciccotti G. (1984), *Stationary nonequilibrium states by molecular dynamics. II. Newton's law*, Phys. Rev. A **29**, 916-925.

[van98]   van der Hoef M. A. and Madden. P. A. (1998), *Novel simulation model for many-body multipole dispersion interactions*, Mol. Phys. **94**, 417-433.

[van99]   van der Hoef M. A. and Madden. P. A. (1999), *Three-body dispersion contributions to the thermodynamic properties and effective pair interactions in liquid argon*, J. Chem. Phys. **111**, 1520-1526.

[Var75]   Vargaftik N. B. (1975), *Handbook of physical properties of liquids and gases*; Hemisphere: Washington.

[Ver67]   Verlet L. (1967), *Computer 'experiments' on classical fluids. I. Thermodynamical properties of Lennard-Jonnes molecules*, Phys. Rev. **159**, 98-103.

[Wee71]   Weeks J. D., Chandler D. and Andersen H. C.(1971), *Role of repulsive forces in determining the equilibrium structure of simple liquids*, J. Chem. Phys. **54**, 5237-5247.

[Wic73]   Wichtherle I., Linek J. and Hala Eduard (1973), *Vapour-liquid equilibrium data bibliography*, Elsevier: Amsterdam.

[Wid63]   Widom B. (1963), *Some Topics in the Theory of Fluids*, J. Chem. Phys. **39**, 2808-2812.

[Wil95]   Wilding N. B. (1995), *Critical-point and coexisting-curve properties of the Lennard-Jones fluid: a finite-size scaling study*, Phys. Rev. E 52, 602-611.

[Yan96]   Yan Q., Liu H. and Hu Y. (1996), *Simulation of phase equilibria for lattice polymers*, Macromolecules **29**, 4066-4071.